

Nonequilibrium dynamics and self-organization in field-driven dipolar colloidal particles

vorgelegt von
Diplom-Physiker

Sebastian Jäger

aus Bottrop

Von der Fakultät II - Mathematik und Naturwissenschaften
der Technischen Universität Berlin
zur Erlangung des akademischen Grades
Doktor der Naturwissenschaften
Dr. rer. nat.

genehmigte Dissertation

Promotionsausschuss:

Vorsitzender: Prof. Dr. Martin Schön
Gutachterin: Prof. Dr. Sabine H. L. Klapp
Gutachter: Prof. Dr. Roland R. Netz

Tag der wissenschaftlichen Aussprache: 20.02.2013

Berlin 2013
D 83

Abstract

In this thesis, we investigate the dynamics and pattern formation behavior of systems of spherical colloidal particles with permanent dipole moments in external time-dependent fields on the basis of computer simulations and theoretical considerations. The computer simulation techniques that we use are molecular dynamics simulations, Langevin dynamics simulations, Wang-Landau Monte Carlo simulations, and Brownian dynamics simulations that include hydrodynamic interactions.

First, we focus on rotating fields in a three-dimensional geometry. Performing simulations at a fixed packing fraction and dipolar coupling parameter, we construct a full nonequilibrium phase diagram as function of the driving frequency and field strength. This diagram contains both synchronized states, where the individual particles follow the field with (on average) constant phase difference, and asynchronous states. The synchronization is accompanied by layer formation, which breaks down at too large driving frequencies. During the transition from layered to unlayered states, complex changes in the single-particle rotational dynamics from synchronous to asynchronous behavior appear. We investigate this dynamic behavior in detail and show that the limit frequencies can be well described as a bifurcation in the nonlinear equation of motion of a single particle rotating in a viscous medium. We also present a density functional theory, which describes the emergence of layers in perfectly synchronized states as an equilibrium phase transition. Finally, we investigate the influence of hydrodynamic interactions on these three-dimensional systems.

In a next step, we consider monolayers of dipolar particles that are driven by rotating external in-plane fields. In these system, two-dimensional cluster formation can occur. We investigate at which field strengths and frequencies these clusters form and explore the influence of hydrodynamic interactions in depth. In particular, we focus on their interplay with the permanent dipolar interactions of the particles. We also examine the phase behavior of the equilibrium system resulting from a time-average of the colloidal interactions in the rotating field. In this way we demonstrate that the clustering in the driven system arises from a first-order phase transition between a vapor and a condensed phase.

Lastly, we report results on the rotational ratchet effect in systems of three-dimensional dipolar particles. The ratchet effect consists of directed rotations of particles in an oscillating magnetic field, which lacks a net rotating component. We investigate the influence of both the random and deterministic contributions to the equations of motion on the ratchet effect. As a main result, we show that dipolar interactions can have an enhancing as well as a dampening effect on the ratchet behavior depending on the dipolar coupling strength of the system under consideration. The enhancement is shown to be caused by an increase in the effective field on a particle generated by neighboring magnetic particles, while the dampening is due to restricted rotational motion in the effective field. Moreover, we find a non-trivial influence of the short-range, repulsive interaction between the particles.

Zusammenfassung

In dieser Arbeit untersuchen wir die Dynamik und das Strukturbildungsverhalten in Systemen aus dipolaren kolloidalen Teilchen mit permanenten Dipolmomenten in externen zeitabhängigen Feldern mittels Computersimulationen und theoretischen Überlegungen. Die verwendeten Computersimulationstechniken sind Molekulardynamik, Langevindynamik und Brownsche Dynamik mit hydrodynamischen Wechselwirkungen.

Zuerst untersuchen wir den Einfluss rotierender Felder auf dipolare kolloidale Systeme in dreidimensionalen Geometrien. Wir konstruieren ein Nichtgleichgewichtsdiagramm, in dem sich sowohl synchronisierte Zustände, in denen die Teilchen dem Feld folgen, als auch nichtsynchronisierte Zustände finden. Die Synchronisation ist von Schichtenbildung begleitet, die bei zu hohen Feldfrequenzen zusammenbricht. Der Zusammenbruch geht mit einem Übergang des Systems in einen asynchronen Zustand einher. Wir untersuchen das damit verbundene dynamische Verhalten und zeigen, dass die Grenzfrequenz durch eine Bifurkation der nichtlinearen Bewegungsgleichung eines isolierten Teilchens, das in einem viskosen Medium rotiert, beschrieben werden kann. Weiterhin konstruieren wir eine Dichtefunktionaltheorie, die das Auftreten der Schichtenbildung in perfekt synchronisierten Systemen beschreibt. Zuletzt untersuchen wir den Einfluss hydrodynamischer Wechselwirkungen auf das System.

Im nächsten Schritt diskutieren wir quasi-zweidimensionale Systeme aus dipolaren Teilchen, die von einem rotierenden Feld getrieben werden. In solchen Systemen können sich zweidimensionale Cluster bilden. Wir studieren das Auftreten der Cluster in Abhängigkeit von den Feldparametern und analysieren den Einfluss hydrodynamischer Wechselwirkungen auf das Verhalten des Systems. Insbesondere das Wechselspiel zwischen den dipolaren und hydrodynamischen Wechselwirkungen untersuchen wir im Detail. Außerdem untersuchen wir das Phasenverhalten des Gleichgewichtssystems, das aus der Mittelung der dipolaren Wechselwirkung im rotierenden Feld hervorgeht. Zusammen mit einer Analyse des Clusterwachstums können wir so zeigen, dass Clusterbildung in einem Phasenübergang zwischen einer gasförmigen und einer kondensierten Phase begründet ist.

Zuletzt untersuchen wir den rotatorischen Ratscheneffekt in dreidimensionalen Systemen aus dipolaren Teilchen. In diesem Effekt kann gerichtete rotatorische Bewegung aus oszillierenden Feldern, die keine Nettorotationskomponente besitzen, gewonnen werden. Wir analysieren den Einfluss sowohl der zufälligen als auch der deterministischen Beiträge in den Bewegungsgleichungen auf den Ratscheneffekt. Als Hauptresultat zeigen wir, dass dipolare Wechselwirkungen einen verstärkenden als auch einen unterdrückenden Effekt auf den Ratscheneffekt haben können. Die Verstärkung des Effekts kann durch einen Anstieg des lokalen Feldes in der Umgebung der dipolaren Teilchen begründet werden. Dieser Anstieg tritt auf, da die Teilchenwechselwirkung das effektiv wirkende Feld verstärkt. Die Unterdrückung ist durch die Einschränkung der rotatorischen Freiheit aufgrund der Dipolwechselwirkungen zu erklären. Außerdem finden wir einen nichttrivialen Einfluss der kurzreichweitigen und abstoßenden Wechselwirkung auf den Ratscheneffekt.

Contents

1. Introduction	9
2. Publications	15
3. Static interactions	17
3.1. The Lennard-Jones interaction	17
3.2. The soft sphere interaction	17
3.3. The soft wall interaction	18
3.4. Shifted interactions	18
3.5. The hard sphere interaction	18
3.6. The dipole-dipole interaction	19
3.7. The dipolar soft sphere interaction	19
4. Simulation methods and equations of motion	21
4.1. Molecular dynamics	21
4.1.1. The leapfrog scheme	21
4.1.2. The Gaussian isokinetic thermostat	22
4.2. Langevin dynamics	24
4.3. Brownian dynamics	24
4.4. Hydrodynamic interactions	26
4.4.1. Hydrodynamic interactions on the diffusion tensor level	27
4.4.2. Brownian dynamics with hydrodynamic interactions	30
4.5. Periodic boundary conditions	32
4.6. Reduced units	32
5. Long-range interactions in simulations	33
5.1. The Ewald sum in three-dimensional ionic bulk systems	33
5.2. The Ewald sum in three-dimensional dipolar bulk systems	36
5.3. The Ewald sum in quasi-two-dimensional dipolar systems	38
5.4. Parallelization	39
6. Phase transitions and density distributions	41
6.1. The vapor-liquid phase transitions	41
6.2. Density functional theory	42
6.2.1. The extremum condition	42
6.2.2. Perturbation expansion of the canonical potential	42
6.2.3. The direct correlation function	43
7. Pattern formation of dipolar colloids in rotating fields: layering and synchronization in three dimensions	47

7.1. Model and simulation methods	48
7.2. Zero field system	48
7.3. The layering effect	48
7.4. Magnetization dynamics	52
7.5. Microscopic rotational dynamics in the layered state	53
7.6. Effective single-particle theory	56
7.7. A density functional approach to layering in a perfectly synchronized system	58
7.8. Influence of hydrodynamic interactions	62
7.9. The role of the simulation method	65
7.10. Conclusions	67
8. Nonequilibrium condensation and coarsening of field-driven dipolar colloids in two dimensions	71
8.1. Model and simulation methods	72
8.2. Synchronization and cluster formation	72
8.3. Relation to condensation	75
8.4. Dynamic coarsening	76
8.5. Influence of hydrodynamic interactions	77
8.5.1. Dynamics on the particle level	78
8.5.2. Cluster dynamics	81
8.5.3. Internal structure of the cluster	84
8.6. Conclusions	86
9. Rotational ratchets with dipolar interactions	89
9.1. Background	90
9.2. Model and simulation methods	90
9.3. The thermal ratchet effect in a non-interacting system	91
9.4. Influence of the particle interactions	93
9.5. Relation to self-assembly	99
9.6. Conclusions	101
10. Summary	103
11. Outlook	105
Appendices	109
A. Pattern formation of dipolar colloids driven by out-of-plane fields in two dimensions	111
A.1. Model and simulation methods	111
A.2. One-dimensional layer formation	111
A.3. Density functional approach to one-dimensional layering in a synchronized system	112
A.4. Conclusion	114
B. Crossover from Normal to Anomalous Diffusion in Systems of Field-Aligned Dipolar Particles	115
B.1. Model and simulation methods	115
B.2. Dynamic behavior of the particles	115

C. Two-dimensional colloidal networks induced by a uni-axial external field	117
C.1. Model and simulation methods	117
C.2. Translational dynamics of the particles	118
D. Ewald expressions for the forces and torques in dipolar systems	120
D.1. In 3d systems	120
D.2. In 2d systems	120
E. Ewald summation of the diffusion tensor	123
F. Reduced units in the ratchet effect	126
G. Abbreviations	127
Bibliography	128

1. Introduction

Colloidal suspensions are suspensions of solid particles that are dispersed in a liquid medium. The dispersed particles are called colloids and are of macroscopic size compared to the particles that the liquid is composed of. Colloidal suspensions are ubiquitous in every day life. Examples include milk, blood, inks, and lubricants.

A particular example of a colloidal suspension is a ferrofluid. Ferrofluids are suspensions of particles with diameters of about 10 nm that contain a single permanent ferromagnetic domain [cf. Fig. 1.1] [1]. The solvent, i.e., the carrier liquid, is often chosen to be water or oil [1,2]. Its constituent particles are much smaller in diameter than the colloidal particles. For instance, the diameter of a water molecule is about 0.28 nm [3].

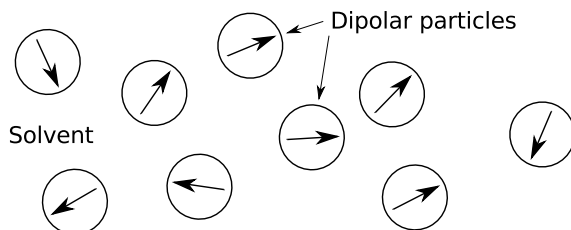


Figure 1.1.: Sketch of the colloidal particles in a ferrofluid. The arrows indicate the orientation of the dipole moments.

Ferrofluids are in widespread use in several applications. They can be found as rotary shaft seals [4] in, e.g., hard discs, as heat dissipation devices in loudspeakers [5], as magnetic carriers for drugs [6], in cancer treatment [7], and in medical imaging [8].

The thermal energy of the colloids of a ferrofluid is on the order of $k_B T$ [1], which is typically too small to keep the particles from sticking together due to van der Waals interactions. To prevent this, these colloids are usually coated with a surfactant, which inhibits a van der Waals induced coagulation [1]. The colloids can also aggregate due to the dipolar interactions. However, whether this happens depends on the dipole strengths of the particles.

A lot of different pattern formation phenomena can be observed in colloidal systems, such as lane formation [9,10], shear banding [11], and the wide range of patterns observed in particles immersed in liquid crystals [12]. In this regard, ferrofluids constitute a particularly interesting subclass of colloidal systems, since they can form exceptional structures. The anisotropy of the dipolar pair interactions of the colloids favors a head-to-tail alignment [Fig. 1.2(a)], which facilitates the formation of spatially disordered chains of particles. The latter was first predicted by de Gennes and Pincus [13] and subsequently shown to be true in computer simulations [14]. Direct experimental evidence of this fact, however, has only recently been put forward [15]. Fig. 1.2(b) shows a Cryogenic Transmission Electron Microscopy (Cryo-TEM) picture of a ferrofluid exhibiting chain-like structures. The suspension was quenched to a low temperature, vitrifying the solvent, after which TEM images were taken.

Indirect insight into the structure of ferrofluids is often obtained by two other methods. These

techniques are small angle neutron scattering (SANS) [16] and small angle X-ray scattering (SAXS) [17], which are well suited to investigate spatially disordered systems. The size scales that are accessible with these methods include the ones that are of interest in ferrofluidic systems. The key quantity that can be obtained by SANS and SAXS is the structure factor of the system. It is directly related to the pair correlation function, which provides information about average spatial correlations between the colloids of the suspension. An additional feature of SANS over SAXS is its ability to examine the magnetic properties of a sample. Neutrons not only scatter due to the interactions with the nuclei but also due to the interactions with the magnetic moments of the electrons.

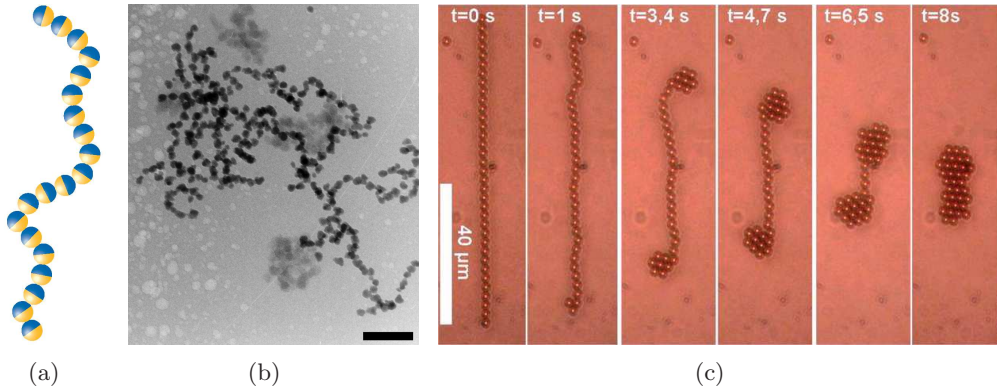


Figure 1.2.: (a) Sketch of the head-to-tail alignment in a chain of permanently dipolar particles. The image was taken from Ref. [18]. (b) Experimental picture from Ref. [15] of chain formation in a ferrofluid in zero field. (c) Process of coiling up of a chain of magnetic particles in a rotating external field. The snapshots of the system were taken at different times after the beginning of the coiling up process. The picture was taken from Ref. [19].

The anisotropy of the dipole-dipole interaction and the resulting preference of the particles to arrange themselves into a head-to-tail alignment has very interesting consequences when the additional influence of an external field is introduced. For instance, in a static and homogeneous field, dipolar particles tend to align into the direction of the field but still arrange themselves into chain-like clusters. As a consequence, the chains are aligned with the external field. This can be seen in Fig. 1.3: Fig. 1.3(a) shows the effect of directed chain formation in a homogeneous field from a simulation point of view, while Fig. 1.3(b) provides an experimental perspective. The latter picture was taken for a system of induced dipoles, where the dipole moments are automatically aligned with the field.

The property of being easily manipulated by external fields makes magnetic particles in general (i.e., particles with induced or permanent magnetic dipole moments) a very interesting subset of colloidal systems. In material science, this is used to control self-assembly and self-organization processes, which are an important prerequisite for synthesizing functional materials [22,23]. The general idea is to use external fields to tune pair interactions and thereby control the morphology of the self-assembled and self-organized structures [24,25], two recent examples being the formation of self-healing membranes of superparamagnetic particles in tilted rotating fields [26] and the coiling up of magnetic chains [see Fig. 1.2(c)] [19].

The interplay of the particle-field interactions and the anisotropic magnetic interactions be-

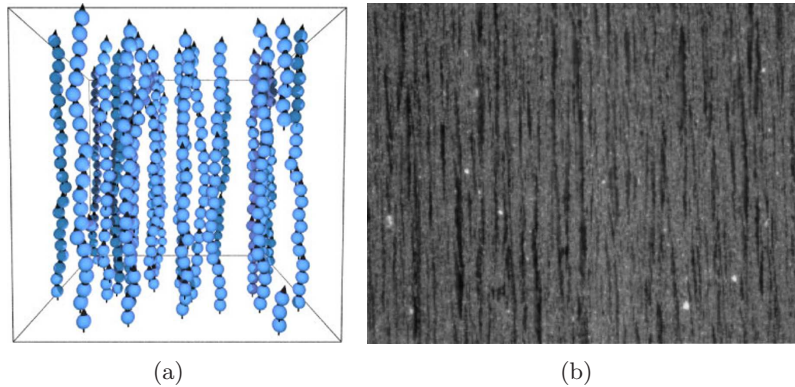


Figure 1.3.: (a) Chain formation of dipolar particles in the direction of the external field. Picture taken from the simulation study [20]. (b) Experimental picture of chain formation in a static and homogeneous field. The used particles are of paramagnetic nature. The image can be found in Ref. [21].

tween the particles can give rise to a wide variety of self-assembled and self-organized patterns. Some examples of the resulting structures found in systems involving dipolar interactions are shown in Figs. 1.3, 1.4, and 1.5. Figs. 1.3 and 1.5(a) depict the formation of field-aligned chains [20, 21, 30–33] and bundles of chains [28], respectively, at low densities in homogeneous fields. At high densities, the formation of bulk crystals can be observed instead [34, 35]. The effects of rotating fields are shown in Fig. 1.4. In a three-dimensional bulk geometry, the dipolar particles can arrange themselves into layers in the plane of the field [Figs. 1.4(a) and 1.4(b)] [21, 22, 33, 36–40]. In quasi-two-dimensions, on the other hand, the formation of clusters that extend into both the spatial dimensions can take place [Fig. 1.4(c)]. The honeycomb-like structures shown in Fig. 1.5(b) are the result of particularly tilted rotating (triaxial) fields [23, 24, 41] and the two-dimensional networks in Fig. 1.5(c) can emerge in oscillating fields [29, 42].

Many pattern formation phenomena are closely intertwined with the field-induced dynamics of the particles. This is, for instance, true for layer formation in rotating fields and pattern formation in triaxial fields. These effects are given rise to by the influence of the external field on the rotational dynamic behavior of the particles. The change in the dynamics affects the effective interparticle interactions, which then facilitate the formation of these structures.

The field-induced dynamic behavior of particles is important in many contexts. For instance, the behavior and functionality of actuators [43], microfluidic switches [44], and particles in optical traps [45] is governed by the particle dynamics. Of particular interest has recently been the field-induced single-particle dynamics of the magnetic colloids of ferrofluids that are exposed to oscillating fields. Surprisingly, the colloidal particles can acquire a torque and perform a net rotation despite the fields lacking a net rotating component [46, 47].

In nonequilibrium many-particle systems [48] and, specifically, in colloidal self-organization processes [49], the influence of hydrodynamic interactions can be of crucial importance. In particular, the dynamics of the colloids can considerably deviate from the ones observed in a system in which these interactions are not accounted for. While historically often ignored, a lot of studies now focus on or take hydrodynamic interactions into account. These interactions are, for instance, considered in colloidal lane formation [50], in systems of sheared ferrofluids [51], and in ratchets [52, 53]. Some effects, such as the hydrodynamic synchronization of particles [54]

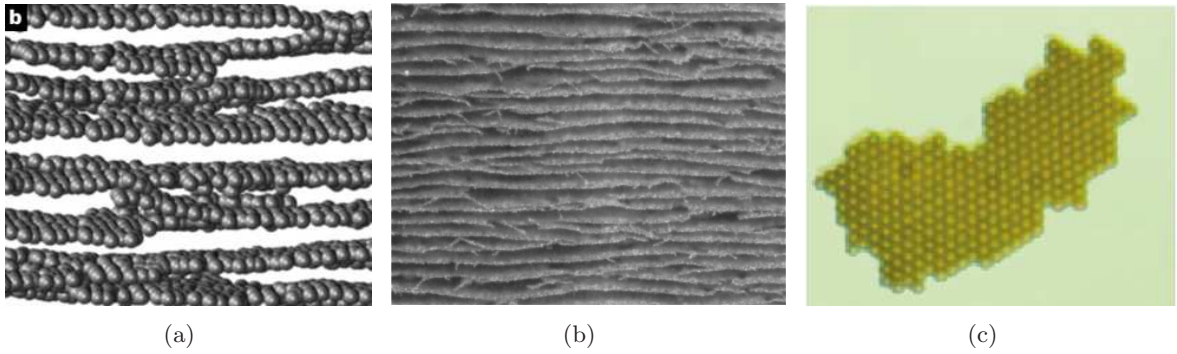


Figure 1.4.: (a) Simulation and (b) experimental pictures of layer formation of paramagnetic particles in a rotating field. The plane of the field coincides with the plane of the layers. The images are taken from [22] and [21], respectively. (c) Experimental picture of cluster formation of dipolar particles in (essentially) two dimensions. The plane of the external field is aligned with the two-dimensional geometry [27].

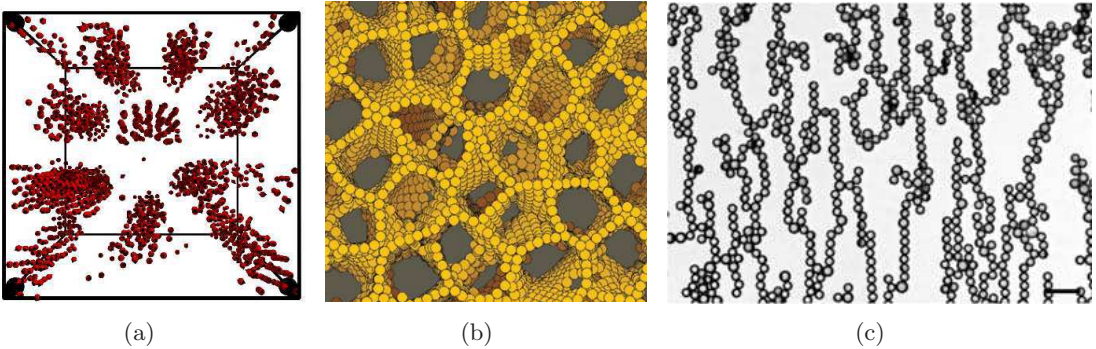


Figure 1.5.: (a) Snapshot from Ref. [28] of bundles of chains of dipolar particles in a static and homogeneous external field. The chains are aligned with the direction of the field. (b) Formation of honeycomb-like structures in systems of induced dipoles in a rotating triaxial field as shown in [23,24]. (c) Network formation in systems of induced dipoles and double-dipoles. Image taken from Ref. [29].

and the coiling up of magnetic chains [see Fig. 1.2(c)] [19] are given rise to by hydrodynamic interactions in the first place.

Historically, magnetic colloidal systems have been investigated with a variety of different methods. In particular computer simulations have played a key role in uncovering the phenomena that can occur in these systems. However, a central problem of computer simulations of dipolar systems is the fact that the dipolar interactions are of long-range. This means that the long-range tail of these interactions cannot simply be neglected, since such a truncation might cause significant physical changes in the dipolar systems [55]. Different techniques were proposed to deal with these long-range interactions. One proposal is the reaction field method [55,56], in which the interactions are truncated after a certain distance. The influence of the remaining particles is then taken into account by considering them as a dielectric medium. Another technique is the fast multipole method [57], where the interactions stemming from neighboring particles are treated as a single interaction source. However, the technique that has been used the most and

is now well established is the Ewald-summation method [58]. It allows for a numerically efficient and also correct evaluation of the dipolar interactions.

Monte Carlo computer simulations [58] have been very important in understanding the static properties of colloidal systems. For instance, the vapor-liquid phase transition in dipolar systems has been thoroughly studied with these simulations [59–62]. Of particular interest have been systems of dipolar particles that lack an attractive, isotropic, short-range attraction, since a full understanding of this transition (or lack thereof) has still not been put forward even in the simplest case of a dipolar hard sphere fluid [60–62].

Molecular dynamics, Langevin dynamics, and Brownian dynamics computer simulations, on the other hand, are very useful if dynamic phenomena are to be studied. In contrast to Monte Carlo simulations, they provide insight into the time evolution of systems. This has, e.g., been used in the investigations of the dynamics of gelation [63], network formation [42], chain formation [20], and magnetic relaxation times [64]. Moreover, these simulation techniques are very well suited to study systems that are driven out of equilibrium. Examples include the investigation of layer formation in rotating fields by Murashov and Patey [37], lane formation in oscillating fields [9], and the coiling up of magnetic chains [19].

The goal of this thesis is to contribute to the understanding of both the dynamic and the pattern formation behavior of permanently dipolar colloidal particles in external time-dependent fields. To achieve this goal, we will make extensive use of the aforementioned computer simulation techniques. Magnetic colloidal particles are very versatile systems due to the strong anisotropy of their interaction and the ease with which they can be influenced by external fields. These properties alone make them exceptionally interesting. However, furthering the understanding of the dynamics, the structure formation that can take place, and the interplay between these, may additionally lead to novel applications for dipolar systems.

The first parts of this thesis constitute an introduction to the methods that will be used in its later parts. The first phenomenon that we will investigate is the formation of layers that can be observed in three-dimensional systems exposed to rotating fields. We will study the structure of the layers, the dynamics associated with this phenomenon, the influence of hydrodynamic interactions, the circumstances under which layers can form, and, most importantly, why the formation of layers occurs in the first place. The methods that we will use in this investigation are of both simulation as well as of purely theoretical character. The computer simulation techniques that we will use are Langevin dynamics, molecular dynamics, and Brownian dynamics with hydrodynamic interactions. On the theoretical side, we will make use of density functional theory and an effective single particle theory. In a next step, we will closely examine the clustering behavior of rotationally driven dipolar colloids in quasi-two-dimensional geometries by Langevin dynamics simulations, Brownian dynamics simulations with hydrodynamic interactions, and Monte Carlo simulations. This behavior is of particular interest in light of recent experimental results by Weddemann et al., who observed this phenomenon experimentally in a system of (permanent) magnetic particles [27]. We will focus on understanding the physical reason for this effect, and investigate the dynamics of the particles as well as that of the entire system. In particular, we study the influence of hydrodynamic interactions on this effect in depth. The Monte Carlo results that will be presented in this context are a contribution of Dr. Heiko Schmidle, who performed these simulations in the framework of his PhD thesis. The third and last major part of this thesis concerns the rotational ratchet effect. As explained above, this effect refers to a phenomenon, in which particles acquire a net torque due to an external field that lacks a net rotating component. Here, we are specifically interested in how dipolar interactions affect the rotational dynamics of the particles, and, thus, the thermal ratchet effect. The principal method that we use in this

investigation are Brownian dynamics simulations. Lastly, in the appendices, contributions of the author of this thesis to other projects are summarized and further details on some of the phenomena and methods used in this thesis are provided.

2. Publications

Parts of this thesis have been published in

- Jelena Jordanovic, Sebastian Jäger, and Sabine H. L. Klapp
Crossover from Normal to Anomalous Diffusion in Systems of Field-Aligned Dipolar Particles.
Phys. Rev. Lett. **106**, 038301 (2011)
- Sebastian Jäger and Sabine H. L. Klapp
Pattern formation of dipolar colloids in rotating fields: layering and synchronization.
Soft Matter **7**, 6606 (2011)
- Sebastian Jäger and Sabine H. L. Klapp
Non-equilibrium structure of rotationally driven dipoles: the role of the simulation method.
Magnetohydrodynamics **47**, 135 (2011)
- Sebastian Jäger, Heiko Schmidle, and Sabine H. L. Klapp
Nonequilibrium condensation and coarsening of field-driven dipolar colloids.
Phys. Rev. E **86**, 011402 (2012)
- Sebastian Jäger and Sabine H. L. Klapp
Rotational ratchets with dipolar interactions.
Phys. Rev. E **86**, 061402 (2012)
- Heiko Schmidle, Sebastian Jäger, Carol K. Hall, Orlin D. Velev, and Sabine H. L. Klapp
Two-dimensional colloidal networks induced by a uni-axial external field.
Soft Matter **9**, 2518 (2013)
- Sebastian Jäger, Holger Stark, and Sabine H. L. Klapp
Dynamics of cluster formation in driven dipolar colloids dispersed on a monolayer.
J. Phys.: Condens. Matter, submitted

3. Static interactions

In this chapter, we discuss different models that are commonly used to describe the interactions between colloidal particles. These interactions will be used in the later parts of this thesis.

3.1. The Lennard-Jones interaction

The Lennard-Jones (LJ) potential is an idealized isotropic pair potential that is commonly used in computer simulations [58]. It approximately describes the interaction between two electrically neutral atoms, molecules, or colloidal particles of (approximate) diameter σ . At a distance r , it is given by

$$U^{\text{LJ}}(r) = 4\epsilon \left[\left(\frac{\sigma}{r} \right)^{12} - \left(\frac{\sigma}{r} \right)^6 \right], \quad (3.1)$$

where ϵ is the depth of the minimum of the potential. The r^{-12} contribution to the potential models a repulsive interaction, which rises very steeply at distances less than σ . The $-1/r^6$ part, on the other hand, models an attraction, which stems from the van der Waals interaction.

3.2. The soft sphere interaction

Sometimes it is useful to consider only the repulsive part of the LJ potential (3.1). This part is called soft sphere (SS) interaction, which is given by

$$U^{\text{SS}}(r) = 4\epsilon \left(\frac{\sigma}{r} \right)^{12}. \quad (3.2)$$

This potential describes the interaction of a purely repulsive particle of a diameter of about σ . However, since the SS potential is soft, there is no simple “true” choice for the value of the diameter. Other definitions are possible and sometimes useful (see, e.g., Ref. [65]). In the following, we will consider σ to be the diameter of the particles.

Particles are often modeled as SSs, if attractive interactions between the colloidal particles are negligible. The lack of attraction can experimentally be achieved by, e.g., coating the particles with a surfactant [1]. The SS interaction is also used when the effects of other, additional interactions are to be investigated. The attractive part of the LJ interaction can have a significant influence on the phase and pattern formation behavior of the particles, which can make it difficult to isolate the effects of the additional interaction. See Sec. 3.7 for details.

Clearly, the force on a particle i due to particle j can be calculated via

$$\mathbf{F}_{ij}^{\text{SS}} = -\nabla_{\mathbf{r}_i} U^{\text{SS}}(r_{ij}). \quad (3.3)$$

Accordingly, the force acting on a particle i due to all the particles in a system is given by

$$\mathbf{F}_i^{\text{SS}} = -\nabla_{\mathbf{r}_i} \sum_{j \neq i} U^{\text{SS}}(r_{ij}). \quad (3.4)$$

3.3. The soft wall interaction

Soft walls can be understood as walls that are comprised of particles that interact with a given particle via a SS potential. Such a wall is infinitely extended into two dimensions and extends infinitely into one direction of the remaining spatial dimension.

A soft wall located at the x -position L that extends into positive values of x interacts via the potential [66, 67]

$$U^{\text{SW}} = -\frac{4}{45}\pi\epsilon_w\rho_V\sigma^3\left(\frac{\sigma}{x-L}\right)^9 \quad (3.5)$$

with the particles of the system. Here, ϵ_w is the SS parameter of the particles that the wall consists of [cf. Eq. (3.2)], ρ_V is their density, and the parameter σ_w their diameter.

3.4. Shifted interactions

In computer simulations, the short-range interactions between the particles are typically truncated after a certain distance. For the LJ and the SS potential this is very often the case at a distance of $r_c = 2.5\sigma$.

Simply cutting off the interactions, however, is not a feasible way of performing a truncation: The potential becomes discontinuous, which results in a discontinuity in the force and a loss of the conservation of energy. Both these problems can be addressed by introducing a shifted potential

$$U^{\text{S}}(r) = U^{\text{S}}(r) - U^{\text{S}}(r_c) + (r_c - r)\frac{dU^{\text{S}}}{dr}(r_c). \quad (3.6)$$

The second term on the right hand side ensures that $U^{\text{S}}(r_c) = 0$, thereby removing the discontinuity in the potential. The introduction of the last term on the right hand side rectifies the former problem. This term guarantees that the gradient of the potential, i.e., the force, remains continuous.

Applying Eq. (3.6) to the SS interaction potential yields the shifted SS (SSS) interaction:

$$U^{\text{SSS}}(r) = 4\epsilon\left(\frac{\sigma}{r}\right)^{12} - 4\epsilon\left(\frac{\sigma}{r_c}\right)^{12} - 48\epsilon\frac{r_c - r}{r}\left(\frac{\sigma}{r}\right)^{12} \quad (3.7)$$

3.5. The hard sphere interaction

The hard sphere (HS) interaction is another kind of an idealized pair interaction. It describes the interaction between particles that are of diameter σ . The hard sphere potential is defined as [58]

$$U^{\text{HS}}(r) = \begin{cases} 0 & \text{if } \sigma \leq r \\ \infty & \text{if } r < \sigma \end{cases}, \quad (3.8)$$

i.e., the particles cannot come closer to each other than σ and do not feel any influence from the other particles unless they are in direct contact.

3.6. The dipole-dipole interaction

The interaction energy between two dipoles of dipole moment $\boldsymbol{\mu}_i$ and $\boldsymbol{\mu}_j$ that are located at \mathbf{r}_i and \mathbf{r}_j is given by [68, 69]

$$U^{\text{D}}(\mathbf{r}_{ij}, \boldsymbol{\mu}_i, \boldsymbol{\mu}_j) = -\frac{3(\mathbf{r}_{ij} \cdot \boldsymbol{\mu}_i)(\mathbf{r}_{ij} \cdot \boldsymbol{\mu}_j)}{r_{ij}^5} + \frac{\boldsymbol{\mu}_i \cdot \boldsymbol{\mu}_j}{r_{ij}^3}, \quad (3.9)$$

where $\mathbf{r}_{ij} = \mathbf{r}_i - \mathbf{r}_j$.

The forces between two dipoles i and j can be calculated as in Eq. (3.3), i.e.,

$$\mathbf{F}_{ij}^{\text{D}} = -\nabla_{\mathbf{r}_i} U^{\text{D}}(\mathbf{r}_{ij}, \boldsymbol{\mu}_i, \boldsymbol{\mu}_j) \quad (3.10)$$

while the respective torques can be obtained by [58]

$$\mathbf{T}_{ij}^{\text{D}} = -\boldsymbol{\mu}_i \times \nabla_{\boldsymbol{\mu}_i} U^{\text{D}}(\mathbf{r}_{ij}, \boldsymbol{\mu}_i, \boldsymbol{\mu}_j). \quad (3.11)$$

Analogous to Eq. (3.4), the forces and torques due to all the particles in a system can be calculated via

$$\mathbf{F}_i^{\text{D}} = -\nabla_{\mathbf{r}_i} \sum_{j \neq i} U^{\text{D}}(\mathbf{r}_{ij}, \boldsymbol{\mu}_i, \boldsymbol{\mu}_j) \quad (3.12)$$

and

$$\mathbf{T}_i^{\text{D}} = -\boldsymbol{\mu}_i \times \nabla_{\boldsymbol{\mu}_i} \sum_{j \neq i} U^{\text{D}}(\mathbf{r}_{ij}, \boldsymbol{\mu}_i, \boldsymbol{\mu}_j). \quad (3.13)$$

In the following, we will assume the dipole moments of the dipolar particles to be fixed to their geometry. This assumption corresponds to neglecting the Néel relaxation of the magnetization, which is justified for not too small particles [47].

3.7. The dipolar soft sphere interaction

The dipolar soft sphere (DSS) interaction is a combination of the SSS interaction (3.7) and the dipole-dipole interaction (3.9). Hence, the corresponding potential is given by

$$U^{\text{DSS}}(\mathbf{r}_{ij}, \boldsymbol{\mu}_i, \boldsymbol{\mu}_j) = U^{\text{SSS}}(r_{ij}) + U^{\text{D}}(\mathbf{r}_{ij}, \boldsymbol{\mu}_i, \boldsymbol{\mu}_j). \quad (3.14)$$

In simulations of dipolar particles, one often uses a DSS potential or a Stockmayer potential (see, e.g., [70]). The latter additionally includes the short-range isotropic, attractive part of the LJ potential (3.1), which models the van der Waals interaction. This attractive part has a considerable influence on the phase behavior of the system. In particular, it can induce a vapor-liquid phase transition [71, 72] that has so far not been found in dipolar systems lacking a spherically symmetric, attractive interaction [62, 73]. Due to this influence on the phase behavior, the short-range attractive part is often neglected, if one is interested in the effects of the dipolar interactions on the dynamic, pattern formation, and phase behavior alone.

4. Simulation methods and equations of motion

Computer simulations are a valuable tool in the realm of physics. Traditionally, the properties of physical systems have been investigated by analytical means. However, in many complex systems, this approach is not feasible. For instance, solving the equations of motion in a many particle system is often an impossible endeavor. Computer simulations allow to sidestep such problems by numerical means.

In this chapter, we describe some of the prominent computer simulation techniques that allow for the investigation of the static and dynamic behavior of colloidal many-particle systems. We will use all of the methods that we present here in the later parts of this thesis.

4.1. Molecular dynamics

Molecular dynamics (MD) computer simulations are based on solving Newton's equations of motion. More precisely, one solves these equations at successive time steps starting from a given initial configuration of the particles.

The translational trajectory of a particle i in MD is calculated by solving Newton's equation

$$m_i \ddot{\mathbf{r}}_i = \mathbf{F}_i, \quad (4.1)$$

where m_i is the mass of the particle and \mathbf{F}_i the force acting on it. The corresponding rotational equation of motion for a particle i whose moment of inertia tensor satisfies $\mathbf{I}_i = I_i \mathbb{1}$ reads

$$I_i \dot{\boldsymbol{\omega}}_i = \mathbf{T}_i. \quad (4.2)$$

Here \mathbf{T}_i is the torque experienced by particle i and I_i is its moment of inertia.

The relation $\mathbf{I}_i = I_i \mathbb{1}$ holds for all spherical particles of constant density. In the following, we will only be concerned with such particles, i.e., $I_i = I \forall i$. Further, we will only consider particles of identical mass which means that $m_i = m \forall i$.

4.1.1. The leapfrog scheme

A commonly used way of solving Newton's equations of motion (4.1) and (4.2) in MD simulations is the leapfrog scheme [58,74]. The equations of motion are (approximately) solved at consecutive time steps in the following way: For the translation,

$$\mathbf{r}_i(t + \Delta t) = \mathbf{r}_i(t) + \dot{\mathbf{r}}_i(t + 1/2\Delta t)\Delta t \quad (4.3)$$

$$\dot{\mathbf{r}}_i(t + 1/2\Delta t) = \dot{\mathbf{r}}_i(t - 1/2\Delta t) + \mathbf{F}_i(t)\Delta t/m \quad (4.4)$$

is calculated, where Δt is a suitable time interval [58].

Similarly, the rotational equations of motion can be solved by [74]

$$\mathbf{e}_i(t + \Delta t) = \mathbf{e}_i(t) + \dot{\mathbf{e}}_i(t + 1/2\Delta t)\Delta t \quad (4.5)$$

$$\dot{\mathbf{e}}_i(t + 1/2\Delta t) = \dot{\mathbf{e}}_i(t - 1/2\Delta t) + \mathbf{G}_i(t)\Delta t/I - 2[\dot{\mathbf{e}}_i(t - 1/2\Delta t) \cdot \mathbf{e}_i(t)]\mathbf{e}_i(t). \quad (4.6)$$

Here, \mathbf{e}_i is the orientation of particle i and $\mathbf{G}_i = \mathbf{T}_i \times \mathbf{e}_i$.

This procedure only yields the velocity and angular velocity at a half time step. The velocities at a full time step can be calculated via [58]

$$\dot{\mathbf{r}}_i(t) = \frac{1}{2} [\dot{\mathbf{r}}_i(t + 1/2\Delta t) + \dot{\mathbf{r}}_i(t - 1/2\Delta t)] \quad (4.7)$$

and

$$\dot{\mathbf{e}}_i(t) = \frac{1}{2} [\dot{\mathbf{e}}_i(t + 1/2\Delta t) + \dot{\mathbf{e}}_i(t - 1/2\Delta t)]. \quad (4.8)$$

4.1.2. The Gaussian isokinetic thermostat

The Gaussian isokinetic thermostat ensures that the kinetic temperatures

$$T_{\text{trans}} = \frac{1}{d_{\text{T}} N k_B} \sum_{i=1}^N m r_i^2 \quad (4.9)$$

and

$$T_{\text{rot}} = \frac{1}{d_{\text{R}} N k_B} \sum_{i=1}^N I \omega_i^2 \quad (4.10)$$

of the system under consideration remain constant at every time step. In Eqs. (4.9) and (4.10), d_{T} and d_{R} denote the number of degrees of freedom of the translational and the rotational motion of the particles, respectively.

As implied by the name, the Gaussian isokinetic thermostat samples from an isokinetic ensemble. Even though not identical, this ensemble does in practice correspond (in equilibrium) to the canonical one (see, e.g., Ref. [75] for details).

In the following, the Gaussian isokinetic thermostat and its algorithmic implementation will be described.

Translational motion

The thermostatting is achieved by introducing an additional “friction coefficient” into the equations of motion. The modified equations can then be written as [58]

$$\dot{\mathbf{r}}_i = \mathbf{p}_i / m \quad (4.11)$$

$$\dot{\mathbf{p}}_i = \mathbf{F}_i - \xi(\mathbf{r}_1, \mathbf{r}_2, \dots, \mathbf{p}_1, \mathbf{p}_2, \dots) \mathbf{p}_i, \quad (4.12)$$

where,

$$\xi = \frac{\sum_i \mathbf{p}_i \cdot \mathbf{F}_i}{\sum_i |\mathbf{p}_i|^2}. \quad (4.13)$$

Depending on the kinetic energy of the system, the additional term either accelerates the dynamics of the system or slows them down.

These modified equations of motion can also be solved by a leapfrog algorithm [58]:

1. Begin by making an unconstrained half step

$$\dot{\mathbf{r}}'_i(t) = \dot{\mathbf{r}}_i(t - 1/2\Delta t) + \frac{1}{2} \mathbf{F}_i(t) \Delta t / m \quad (4.14)$$

2. Calculate

$$\chi = \sqrt{\frac{T}{T'_{\text{trans}}}}, \quad (4.15)$$

where T is the desired temperature of the system and T'_{trans} the kinetic temperature (4.9) calculated from the unconstrained velocities

3. Complete the velocity calculation by evaluating

$$\dot{\mathbf{r}}_i(t + 1/2\Delta t) = (2\chi - 1)\dot{\mathbf{r}}_i(t - 1/2\Delta t) + \chi\mathbf{F}_i(t)\Delta t/m \quad (4.16)$$

4. Update the position

$$\mathbf{r}_i(t + \Delta t) = \mathbf{r}_i(t) + \dot{\mathbf{r}}_i(t + 1/2\Delta t)\Delta t \quad (4.17)$$

This procedure yields an approximate solution to the modified equations of motion (4.11) and (4.12).

Note that the velocities at a full time step can be calculated as described in Sec. 4.1.1.

Rotational motion Analogously, Newton's equations of motion for the rotation can be modified (for linear particles) [74]:

$$\dot{\mathbf{e}}_i = \mathbf{u}_i \quad (4.18)$$

$$\dot{\mathbf{u}}_i = \frac{\mathbf{G}_i}{I} - \lambda_i\mathbf{e}_i - \alpha\mathbf{u}_i \quad (4.19)$$

Here, λ_i and α are two constraints that satisfy

$$\lambda_i = \mathbf{u}_i^2 \quad (4.20)$$

$$\alpha = \frac{2}{\Delta t} \left(\frac{1}{\beta} - 1 \right) \quad (4.21)$$

[see Eq. (4.23) for the definition of β]. The leapfrog scheme used to solve these equations is similar to the one for the translation [74]:

1. Make an unconstrained step

$$\dot{\mathbf{e}}'_i(t) = \dot{\mathbf{e}}_i(t - 1/2\Delta t) - [\dot{\mathbf{e}}_i(t - 1/2\Delta t) \cdot \mathbf{e}_i(t)]\mathbf{e}_i(t) + \frac{1}{2}\mathbf{G}_i(t)\Delta t/I \quad (4.22)$$

2. Calculate

$$\beta = \sqrt{\frac{T}{T'_{\text{rot}}}}, \quad (4.23)$$

where T'_{rot} is the rotational kinetic temperature (4.10) calculated from the unconstrained angular velocities

3. Complete the velocity calculation by using

$$\dot{\mathbf{e}}_i(t + 1/2\Delta t) = \mathbf{e}_i(t - 1/2\Delta t)(2\beta - 1) + \beta\mathbf{G}_i(t)\Delta t/I - 2\beta[\dot{\mathbf{e}}_i(t - 1/2\Delta t) \cdot \mathbf{e}_i(t)]\mathbf{e}_i(t) \quad (4.24)$$

4. Update the orientation

$$\mathbf{e}_i(t + \Delta t) = \mathbf{e}_i(t) + \dot{\mathbf{e}}_i(t + \Delta t)\Delta t \quad (4.25)$$

Following this algorithm approximately solves the rotational equations of motion (4.18) and (4.19).

4.2. Langevin dynamics

In colloidal suspensions, the particles of interest are surrounded by a solvent. To take the interactions of the solvent particles among themselves as well as with the colloidal particles explicitly into account is in most cases numerically excessively demanding. Langevin dynamics (LD) can be understood as trying to overcome this by introducing two additional terms into Newton's equations of motion: A term corresponding to the friction that the particles experience when traveling through a solvent and a random term mimicking the Brownian kicks of the solvent particles. The equations of motion then are [37, 76]

$$m\ddot{\mathbf{r}}_i = \mathbf{F}_i - \xi_T \dot{\mathbf{r}}_i + \mathbf{F}_i^G \quad (4.26)$$

$$I\dot{\boldsymbol{\omega}}_i = \mathbf{T}_i - \xi_R \boldsymbol{\omega}_i + \mathbf{T}_i^G, \quad (4.27)$$

where ξ_T and ξ_R are the translational and rotational friction coefficients. \mathbf{F}_i^G and \mathbf{T}_i^G are random Gaussian forces and torques on particle i with zero mean

$$\langle \mathbf{F}_i^G(t) \rangle = 0 \quad (4.28)$$

$$\langle \mathbf{T}_i^G(t) \rangle = 0, \quad (4.29)$$

whose variance is related to the friction coefficients via

$$\langle \mathbf{F}_i^G(t) \mathbf{F}_j^G(t') \rangle = 2k_B T \xi_T \delta_{ij} \delta(t - t') \mathbb{1} \quad (4.30)$$

$$\langle \mathbf{T}_i^G(t) \mathbf{T}_j^G(t') \rangle = 2k_B T \xi_R \delta_{ij} \delta(t - t') \mathbb{1}. \quad (4.31)$$

Eqs. (4.30) and (4.31) relate the variance of the Gaussian random forces and torques to the friction coefficients. These specific relations can be obtained by the fluctuation-dissipation theorem [77]: They ensure that the system remains at the temperature T , i.e., the random forces and torques balance out the energy losses due to the dissipation.

The equations of motion (4.26) and (4.27) can be integrated via the leapfrog scheme [37]. In that case, the averages of the random forces and torques over a time interval Δt satisfy

$$\langle \mathbf{F}_i^{G'} \rangle = 0 \quad (4.32)$$

$$\langle \mathbf{T}_i^{G'} \rangle = 0, \quad (4.33)$$

and [78]

$$\langle \mathbf{F}_i^{G'}(\Delta t) \mathbf{F}_j^{G'}(\Delta t) \rangle = 2k_B T \xi_T \delta_{ij} \Delta t^{-1} \mathbb{1} \quad (4.34)$$

$$\langle \mathbf{T}_i^{G'}(\Delta t) \mathbf{T}_j^{G'}(\Delta t) \rangle = 2k_B T \xi_R \delta_{ij} \Delta t^{-1} \mathbb{1}. \quad (4.35)$$

4.3. Brownian dynamics

Brownian dynamics (BD) simulations are similar to LD simulations. Both can be understood as taking the influence of a solvent medium on a basic single-particle level into account. The difference between both these methods, however, is that the inertial terms in the equations of motion are neglected in BD. Essentially, this means that one looks at time scales, at which the momenta of the colloidal particles have relaxed. As a consequence, this makes time scales

inaccessible in BD computer simulations that are smaller than this relaxation time [78, 79]. The equations of motion of BD are [51, 80, 81]

$$\dot{\mathbf{r}}_i = \frac{1}{k_B T} \sum_j D_0^T \mathbf{F}_j + \mathbf{R}_i^T \quad (4.36)$$

$$\dot{\boldsymbol{\omega}}_i = \frac{1}{k_B T} \sum_j D_0^R \mathbf{T}_j + \mathbf{R}_i^R. \quad (4.37)$$

Here,

$$D_0^T = \frac{k_B T}{3\pi\eta a} \quad (4.38)$$

and

$$D_0^R = \frac{k_B T}{\pi\eta a^3} \quad (4.39)$$

are the translational and rotational diffusion constant, respectively, where a is the diameter of the colloidal particles and η the viscosity of the solvent. The quantities \mathbf{R}_i^T and \mathbf{R}_i^R in Eqs. (4.36) and (4.37) are random contributions that satisfy

$$\langle \mathbf{R}_i^T \rangle = 0 \quad (4.40)$$

$$\langle \mathbf{R}_i^R \rangle = 0, \quad (4.41)$$

and

$$\langle \mathbf{R}_i^T(t) \mathbf{R}_j^T(t') \rangle = 2D_0^T \delta_{ij} \delta(t - t') \mathbb{1} \quad (4.42)$$

$$\langle \mathbf{R}_i^R(t) \mathbf{R}_j^R(t') \rangle = 2D_0^R \delta_{ij} \delta(t - t') \mathbb{1} \quad (4.43)$$

[cf. Eqs. (4.30) and (4.31)].

In simulations, these equations of motion can be solved via [64, 82–84]

$$\mathbf{r}_i(t + \Delta t) = \mathbf{r}_i(t) + \frac{1}{k_B T} D_0^T \mathbf{F}_i \Delta t + \mathbf{R}_i^{T'} \quad (4.44)$$

$$\mathbf{e}_i(t + \Delta t) = \mathbf{e}_i(t) + \frac{1}{k_B T} D_0^R \mathbf{T}_i \Delta t \times \mathbf{e}_i(t) + \mathbf{R}_i^{R'} \times \mathbf{e}_i(t), \quad (4.45)$$

which corresponds to solving the equations of motion via the Euler-Maruyama method [85, 86].¹

Here, the random variables $\mathbf{R}_i^{T'}$ and $\mathbf{R}_i^{R'}$ satisfy

$$\langle \mathbf{R}_i^{T'} \rangle = 0 \quad (4.46)$$

$$\langle \mathbf{R}_i^{R'} \rangle = 0, \quad (4.47)$$

and

$$\langle \mathbf{R}_i^{T'}(\Delta t) \mathbf{R}_j^{T'}(\Delta t) \rangle = 2D_0^T \delta_{ij} \Delta t \mathbb{1}, \quad (4.48)$$

$$\langle \mathbf{R}_i^{R'}(\Delta t) \mathbf{R}_j^{R'}(\Delta t) \rangle = 2D_0^R \delta_{ij} \Delta t \mathbb{1}. \quad (4.49)$$

¹Strictly speaking, to arrive at Eq. (4.45) via the Euler-Maruyama scheme, one first solves Eq. (4.37) and then calculates the new particle orientations with the obtained values of $\Delta\boldsymbol{\omega}_i$.

Note that the diffusion constants defined in Eqs. (4.38) and (4.39) are related to the friction coefficients ξ_T and ξ_R [Eqs. (4.26) and (4.27)] introduced in the previous section. Specifically, they are related according to

$$\xi_T = \frac{k_B T}{D_0^T} \quad (4.50)$$

and

$$\xi_R = \frac{k_B T}{D_0^R}. \quad (4.51)$$

Eqs. (4.50) and (4.51) are called ‘‘Einstein relations’’ and are again a fluctuation-dissipation relation.

4.4. Hydrodynamic interactions

LD and BD simulations take the influence of a solvent only on a very basic level into account: Only friction and random terms are considered that do not depend on the specific configuration of the colloidal particles. A real solvent, however, is influenced by the immersed colloidal particles and their movements, thereby mediating interactions between the particles.

Different simulation techniques exist that can take the effects of these hydrodynamic interactions (HIs) between colloidal particles into account. Very commonly used are lattice Boltzmann (LB) methods [87,88], multi-particle collision dynamics² (MPCD) [89], Stokesian dynamics (SD) [84,90], and BD with HIs [64,82].

The latter two methods solve the Navier-Stokes equation under suitable boundary conditions to model HIs (see below), while the former two methods use different approaches:

- In LB methods, the fluid is modeled by a probability density distribution f . This distribution is defined on a discrete lattice and is a function of the lattice positions as well as the allowed (only along a finite number of directions) velocities in the lattice. The probability density is updated according to the discretized Boltzmann equation. From this procedure, macroscopic fluid dynamics emerges.

One way to treat colloids in these simulations is to assume a solvent-colloid interaction, if f assumes a non-vanishing value within the boundary of a colloidal particle. The interactions then essentially take place via ‘‘collisions’’ between the colloids and the ‘‘inflowing’’ momentum described by the probability distribution f .

- In MPCD, the solvent particles are described by an ideal gas that interacts with the colloidal particles via collisions. The interactions of the solvent particles with each other are modeled by redistributing the kinetic energies of the particles within fixed cells. This ensures that, e.g., momentum is transported within the solvent.
- SD and BD with HIs are similar methods. In both cases the Navier-Stokes equation is solved (see below). The former method is more accurate but also much more computationally demanding: It requires an additional inversion of a (at least) $6N \times 6N$ matrix (in three dimensions), where N is the number of considered particles.

²MPCD is also called stochastic rotation dynamics (SRT)

In this thesis, we will use BD with HIs to account for the effects of the solvent-mediated interactions. This method is an extension of the BD algorithm presented in the previous section. Using this method makes it straightforward to isolate the effects of HIs, since the standard BD algorithm is recovered by switching the solvent-mediated interactions off. The resulting ease of assessing the influence of the HIs alone will be very useful later on.

A similar argument can be made for SD. However, here we are interested in the effects of HIs in large many-particle systems. The fact that BD with HIs is a considerably faster simulation technique allows us to investigate larger systems and explore longer time scales than would be possible with SD.

4.4.1. Hydrodynamic interactions on the diffusion tensor level

When considering HIs on the diffusion tensor level, the HIs between the colloids are implicitly taken into account. Implicitly means that the solvent is not considered on a particle level but that its effects are accounted for on, e.g., the basis of the Navier-Stokes (NS) and the continuity equation.

The Stokes equations

For incompressible solvents the NS equation is given by [91]

$$\rho_0 \frac{\partial \mathbf{u}(\mathbf{r}, t)}{\partial t} + \rho_0 \mathbf{u}(\mathbf{r}, t) \nabla \mathbf{u}(\mathbf{r}, t) = \eta \nabla^2 \mathbf{u}(\mathbf{r}, t) - \nabla p(\mathbf{r}, t) + \mathbf{f}(\mathbf{r}), \quad (4.52)$$

while the continuity equation can be written as

$$\nabla \cdot \mathbf{u}(\mathbf{r}, t) = 0. \quad (4.53)$$

Here, \mathbf{u} is the velocity field within the solvent, η is its viscosity, ρ_0 is its density, p is the pressure, and $\mathbf{f}(\mathbf{r})$ is the force density acting at a position \mathbf{r} .

The NS equation can be simplified in the limit of small Reynolds numbers. The limit of small Reynolds numbers corresponds to the inertial forces in the solvent being very small compared to the viscous ones. For the case of a spherical particle moving through a solvent, the Reynolds number is given by

$$\text{Re} = \frac{\rho_0 a v}{\eta}, \quad (4.54)$$

where a is the diameter of the particle and v its velocity with respect to the solvent. If $\text{Re} \ll 1$ and on sufficiently long time scales, Eq. (4.52) essentially reduces to [91]

$$\nabla p(\mathbf{r}, t) - \eta \Delta \mathbf{u}(\mathbf{r}, t) = \mathbf{f}(\mathbf{r}). \quad (4.55)$$

Eqs. (4.55) and (4.53) are called the creeping flow or Stokes equations.

Note that due to the linearity of the Stokes equations, the velocity of the fluid is directly proportional to the forces acting on it.

Hydrodynamic flow fields due to a point force

Consider a point force density acting at point \mathbf{r}' in the fluid:

$$\mathbf{f}(\mathbf{r}) = \delta(\mathbf{r} - \mathbf{r}') \mathbf{f}_0 \quad (4.56)$$

Since the Stokes equations are linear, the flow field due to this point force density is given by

$$\mathbf{u}(\mathbf{r}) = \mathbf{T}(\mathbf{r} - \mathbf{r}')\mathbf{f}_0. \quad (4.57)$$

Here, \mathbf{T} is the Oseen tensor and Green's function of the Stokes equations.

An expression for the Oseen tensor can be obtained by inserting Eq. (4.57) and an equivalent one for the pressure into the Stokes equations (4.55) and (4.53). One then finds

$$\mathbf{T}(\mathbf{r}) = \frac{1}{8\pi\eta r}(\mathbb{1} + \hat{\mathbf{r}}\hat{\mathbf{r}}) \quad (4.58)$$

for the Oseen tensor, where $\hat{\mathbf{r}} = \mathbf{r}/r$.

Hydrodynamic interactions for a single particle system

Clearly, with the above results in mind, the flow field due to a force distribution \mathbf{f} is given by

$$\mathbf{u}(\mathbf{r}) = \int d\mathbf{r}' \mathbf{T}(\mathbf{r} - \mathbf{r}')\mathbf{f}(\mathbf{r}'). \quad (4.59)$$

If we consider the forces to be located on the surface S of a sphere (i.e., a particle), it follows for the flow field that

$$\mathbf{u}(\mathbf{r}) = \int_S dS' \mathbf{T}(\mathbf{r} - \mathbf{r}')\mathbf{f}(\mathbf{r}'), \quad (4.60)$$

where \mathbf{f} is now the force per unit area that a surface element of the sphere/particle exerts on the fluid.

On the surface of the particle, the flow field has to obey certain boundary conditions. Typically, the fluid is assumed to stick to the particle, which means that the flow field satisfies

$$\mathbf{u}(\mathbf{r}) = \mathbf{u}' + \boldsymbol{\omega}' \times (\mathbf{r} - \mathbf{r}') \quad \forall \mathbf{r} \in S. \quad (4.61)$$

Here, \mathbf{u}' and $\boldsymbol{\omega}'$ denote the translational and rotational velocity of the particle, respectively, and \mathbf{r}' is its position. Additionally, one assumes that the fluid rests at infinite distances:

$$\mathbf{u}(\mathbf{r}) \rightarrow 0, r \rightarrow \infty \quad (4.62)$$

The equations of motion for a colloidal particle, which relate its velocity to the force acting on it, can then be arrived at by solving Eq. (4.60) under the boundary conditions (4.61) and (4.62).

Hydrodynamic interactions for a many particle system

Similarly, the relation between the forces and the velocities of a many-particle system can be derived. Instead of considering a force that is located on a single spherical surface, we now assume non-vanishing forces on the surfaces of N spheres. It then follows

$$\mathbf{u}(\mathbf{r}) = \sum_{i=1}^N \int_{S_i} dS' \mathbf{T}(\mathbf{r} - \mathbf{r}')\mathbf{f}_i(\mathbf{r}') \quad (4.63)$$

for the flow field, where \mathbf{f}_i is the force per unit area on the surface S_i .

In this case, sticky boundary conditions imply that

$$\mathbf{u} = \mathbf{u}_i + \boldsymbol{\omega}_i \times (\mathbf{r} - \mathbf{r}_i) \quad \forall \mathbf{r} \in S_i, i = 1, \dots, N. \quad (4.64)$$

Here, \mathbf{r}_i is the position of particle i and \mathbf{u}_i and $\boldsymbol{\omega}_i$ its translational and rotational velocity. Moreover, it is once again assumed that the fluid rests at infinite distances, i.e., that Eq. (4.62) holds.

Due to the linearity of the Stokes equations, the equations of motion are given by the linear relation [80,91]

$$\underline{\mathbf{u}} = \mathbf{D}\underline{\mathbf{S}}. \quad (4.65)$$

Here, the vector $\underline{\mathbf{u}}$ contains the velocities of the particles, i.e.,

$$\underline{\mathbf{u}} = \begin{pmatrix} \dot{\mathbf{r}}_1 \\ \dots \\ \dot{\mathbf{r}}_N \\ \boldsymbol{\omega}_1 \\ \dots \\ \boldsymbol{\omega}_N \end{pmatrix}, \quad (4.66)$$

and the vector

$$\underline{\mathbf{S}} = \begin{pmatrix} \mathbf{F}_1 \\ \dots \\ \mathbf{F}_N \\ \mathbf{T}_1 \\ \dots \\ \mathbf{T}_N \end{pmatrix} \quad (4.67)$$

is comprised of the forces and torques acting on the particles due to the interparticle pair interactions. The quantity \mathbf{D} is the grand diffusion tensor, which can here be written as [92]

$$\mathbf{D} = \begin{pmatrix} \mathbf{D}^{\text{TT}} & \mathbf{D}^{\text{TR}} \\ \mathbf{D}^{\text{RT}} & \mathbf{D}^{\text{RR}} \end{pmatrix}. \quad (4.68)$$

The subtensors \mathbf{D}^{TT} , \mathbf{D}^{TR} , \mathbf{D}^{RT} , and \mathbf{D}^{RR} are specified below. For a rigorous derivation of the equations of motion and the grand diffusion tensor see Refs. [91,93].

The diffusion tensor (4.68) is symmetric and positive definite. It does not have an exact analytic representation, i.e., only approximate expressions for (4.68) exist. Very commonly one considers the diffusion tensor up to third order in the inverse particle distance [84,90]. The subtensors

\mathbf{D}^{TT} , \mathbf{D}^{TR} , \mathbf{D}^{RT} , and \mathbf{D}^{RR} of the grand diffusion tensor \mathbf{D} are then given by³ [64, 82, 94]

$$\mathbf{D}_{ii}^{\text{TT}} = \frac{k_B T}{3\pi\eta a} \mathbb{1} \quad (4.69)$$

$$\mathbf{D}_{ij}^{\text{TT}} = \frac{k_B T}{8\pi\eta} \frac{1}{r_{ij}} \left[(\mathbb{1} + \hat{\mathbf{r}}_{ij} \hat{\mathbf{r}}_{ij}) + \frac{a^2}{6r_{ij}^2} (\mathbb{1} - 3\hat{\mathbf{r}}_{ij} \hat{\mathbf{r}}_{ij}) \right] \quad (4.70)$$

$$\mathbf{D}_{ii}^{\text{RT}} = \mathbf{D}_{ii}^{\text{TR}} = 0 \quad (4.71)$$

$$\mathbf{D}_{ij}^{\text{TR}} = \mathbf{D}_{ji}^{\text{RT}} = \frac{k_B T}{8\pi\eta} \frac{1}{r_{ij}^2} \boldsymbol{\epsilon} \hat{\mathbf{r}}_{ij} \quad (4.72)$$

$$\mathbf{D}_{ii}^{\text{RR}} = \frac{k_B T}{\pi\eta a^3} \mathbb{1} \quad (4.73)$$

$$\mathbf{D}_{ij}^{\text{RR}} = \frac{k_B T}{16\pi\eta} \frac{1}{r_{ij}^3} (3\hat{\mathbf{r}}_{ij} \hat{\mathbf{r}}_{ij} - \mathbb{1}), \quad (4.74)$$

where $\boldsymbol{\epsilon}$ is the Levi-Civita density, which satisfies $\epsilon_{123} = \epsilon_{231} = \epsilon_{312} = 1$, $\epsilon_{321} = \epsilon_{213} = \epsilon_{132} = -1$, and is equal to zero for other choices of the indices. The tensors above describe the different hydrodynamic couplings, i.e., the coupling between the translational motion of the particles (TT), between the translation and the rotational motion (TR) and vice versa (RT), and the coupling between the rotational motion (RR). The specific tensor given in Eqs. (4.69) and (4.70), i.e., \mathbf{D}^{TT} , is the well known Rotne-Prager tensor [95].

Note that in three-dimensional systems of N particles, \mathbf{D}^{TT} , \mathbf{D}^{TR} , \mathbf{D}^{RT} , and \mathbf{D}^{RR} are $3N \times 3N$ matrices. In quasi-two-dimensional systems, however, \mathbf{D}^{TT} is a $2N \times 2N$ matrix, \mathbf{D}^{RT} a $3N \times 2N$ dimensional one, and, accordingly, \mathbf{D}^{TR} a $2N \times 3N$ dimensional one. The dimension of \mathbf{D}^{RR} remains unchanged.

4.4.2. Brownian dynamics with hydrodynamic interactions

The equations of motion (4.65) do not include the effects of Brownian noise. To rectify this, a further set of equations of motion needs to be considered. Specifically, consider the following Langevin equations [82, 83, 96, 97]:

$$m\ddot{\mathbf{r}}_i = \sum_j \mathbf{F}_j - \sum_j (\boldsymbol{\xi}_{ij}^{\text{TT}} \dot{\mathbf{r}}_j + \boldsymbol{\xi}_{ij}^{\text{TR}} \boldsymbol{\omega}_j) + \sum_j \boldsymbol{\alpha}_{ij} \mathbf{f}_j \quad (4.75)$$

$$I\dot{\boldsymbol{\omega}}_i = \sum_j \mathbf{T}_j - \sum_j (\boldsymbol{\xi}_{ij}^{\text{RR}} \boldsymbol{\omega}_j + \boldsymbol{\xi}_{ij}^{\text{RT}} \dot{\mathbf{r}}_j) + \sum_j \boldsymbol{\alpha}_{ij} \mathbf{f}_j \quad (4.76)$$

Here, the friction tensors $\boldsymbol{\xi}^{\text{TT}}$, $\boldsymbol{\xi}^{\text{TR}}$, $\boldsymbol{\xi}^{\text{RT}}$, and $\boldsymbol{\xi}^{\text{RR}}$ are subtensors of the grand friction tensor

$$\boldsymbol{\xi} = \begin{pmatrix} \boldsymbol{\xi}^{\text{TT}} & \boldsymbol{\xi}^{\text{TR}} \\ \boldsymbol{\xi}^{\text{RT}} & \boldsymbol{\xi}^{\text{RR}} \end{pmatrix}. \quad (4.77)$$

Further, the quantities $\boldsymbol{\alpha}_{ij}$ that appear in Eqs. (4.75) and (4.76) are defined by

$$\boldsymbol{\xi}_{ij} = \frac{1}{k_B T} \boldsymbol{\alpha}_{il} \boldsymbol{\alpha}_{jl}^\dagger \quad (4.78)$$

³Calculating the diffusion tensor as described here is also called the method of the additivity of velocities [80]. Alternatively, it is also possible to calculate the resistance tensor \mathbf{R} ($\mathbf{R}\mathbf{u} = \mathbf{S}$) [90] and obtain the velocities by evaluating $\mathbf{u} = \mathbf{R}^{-1}\mathbf{S}$. This approach is called the additivity of forces [80].

while the random vectors \mathbf{f}_i satisfy

$$\langle \mathbf{f}_i \rangle = 0 \quad (4.79)$$

$$\langle \mathbf{f}_i(t) \mathbf{f}_j(t') \rangle = 2\delta_{ij} \delta(t - t') \mathbf{1}. \quad (4.80)$$

The Langevin Eqs. (4.75) and (4.76) describe the Brownian motion of a set of particles that are immersed in an incompressible solvent. More precisely, they take the influence of HIs on the level on the diffusion tensor into account. This fact is reflected in the relation [82]

$$\mathbf{D} = k_B T \boldsymbol{\xi}^{-1} \quad (4.81)$$

between the grand friction tensor (4.77) and the grand diffusion tensor (4.68).

To obtain an integration scheme for the equations of motion (4.75) and (4.76), these equations are integrated over time. Integrating over suitable time intervals, one obtains [64, 82, 83]

$$\mathbf{r}_i(t + \Delta t) = \mathbf{r}_i(t) + \frac{1}{k_B T} \sum_j \mathbf{D}_{ij}^{\text{TT}} \mathbf{F}_j \Delta t + \frac{1}{k_B T} \sum_j \mathbf{D}_{ij}^{\text{TR}} \mathbf{T}_j \Delta t + \mathbf{R}_i(\mathbf{D}, \Delta t) \quad (4.82)$$

and

$$\begin{aligned} \mathbf{e}_i(t + \Delta t) = \mathbf{e}_i(t) + \left(\frac{1}{k_B T} \sum_j \mathbf{D}_{ij}^{\text{RT}} \mathbf{F}_j \Delta t + \frac{1}{k_B T} \sum_j \mathbf{D}_{ij}^{\text{RR}} \mathbf{T}_j \Delta t \right) \times \mathbf{e}_i(t) \\ + \mathbf{R}_i(\mathbf{D}, \Delta t) \times \mathbf{e}_i(t) \end{aligned} \quad (4.83)$$

assuming that $\nabla_{\mathbf{r}_i} \cdot \mathbf{D}_{ij}^{\text{T}} = \nabla_{\mathbf{r}_i} \cdot \mathbf{D}_{ij}^{\text{TR}} = 0$. Note that this assumption is true for $\mathbf{D}_{ij}^{\text{TT}}$ and $\mathbf{D}_{ij}^{\text{TR}}$ as shown in Eqs. (4.69)-(4.72) [64]. The integration scheme (4.82) is called the Ermak-McCammon algorithm, which is very widely used in BD simulations with HIs [98].

The random displacements in Eqs. (4.82) and (4.83) satisfy

$$\langle \mathbf{R}_i \rangle = 0 \quad (4.84)$$

$$\langle \mathbf{R}_i(\Delta t) \mathbf{R}_j(\Delta t) \rangle = 2\mathbf{D}_{ij} \Delta t. \quad (4.85)$$

The actual calculation of these displacements in a computer simulation can be done by evaluating

$$\underline{\mathbf{R}} = \sqrt{2\Delta t} \mathbf{L} \cdot \boldsymbol{\xi}, \quad (4.86)$$

where $\underline{\mathbf{R}}$ is the vector comprised of all the \mathbf{R}_i , $\boldsymbol{\xi}$ is a vector of normally distributed random numbers, and \mathbf{L} is a lower triangular matrix that satisfies

$$\mathbf{D} = \mathbf{L} \cdot \mathbf{L}^{\text{T}}. \quad (4.87)$$

\mathbf{L} can be found via Cholesky decomposition (see, e.g., Ref. [99]) of the Hermitian, positive definite grand diffusion tensor \mathbf{D} .

Note that Eqs. (4.82) and (4.83) solve the equations of motion (4.65), if the random terms in the former equations are neglected. Hence, the Langevin Eqs. (4.75) and (4.76) differ from the equations of motion (4.65) only by the noise contributions, if the inertial terms are neglected (i.e., on sufficiently long time scales).

Finally, note that by setting to zero all hydrodynamic coupling tensors involving different particles $i \neq j$, the algorithm given in Eqs. (4.82) and (4.83) reduces to the standard algorithm for BD simulations [Eqs. (4.36) and (4.37)] without HIs.

4.5. Periodic boundary conditions

In computer simulations, one typically integrates the equations of motion for a number of particles in a simulation box. When using periodic boundary conditions, this box is surrounded by mirror images of the simulation box with the particles moving as their mirrored counterparts. If a particle leaves the simulation box, the particle reenters the box at the point where its mirror image moves into the box.

Now only the forces, torques, or interaction energies for the particles within the simulation box need to be calculated. Interactions acting on the particles outside of the box do not need to be evaluated and no equations of motion for such particles need to be solved.

4.6. Reduced units

For brevity and readability we write down some of the quantities here with their units reduced. These reduced quantities are denoted by a superscript “*”. In particular we use:

Quantity	Reduced as
distance vector	$\mathbf{r}^* = \mathbf{r}/\sigma$
time	$t^* = (m\sigma^2/\epsilon)^{-1/2}t$
field strength	$B_0^* = (\sigma^3/\epsilon)^{1/2}B_0$
angular frequency of the field	$\omega_0^* = (m\sigma^2/\epsilon)^{1/2}\omega_0$
density	$\rho^* = \sigma^3\rho$
translational diffusion constant	$D_0^{T*} = (\epsilon\sigma^2/m)^{-1/2}D_0^T$
rotational diffusion constant	$D_0^{R*} = (m\sigma^2/\epsilon)^{1/2}D_0^R$
translational friction coefficient	$\xi_T^* = (m\epsilon/\sigma^2)^{-1/2}\xi_T$
rotational friction coefficient	$\xi_R^* = (m\epsilon\sigma^2)^{-1/2}\xi_R$
dipole moment	$\mu^* = (\epsilon\sigma^3)^{-1/2}\mu$
moment of inertia	$I^* = (m\sigma^2)^{-1}I$
temperature	$T^* = k_B T/\epsilon$
torque	$\mathbf{T}^* = \mathbf{T}/\epsilon$

5. Long-range interactions in simulations

Long-range interactions are interactions that cannot simply be truncated after a prescribed distance. Doing so would significantly change the physical properties of the considered system. Interactions arising from a potential are typically of long-range if the potential falls off with a power smaller or equal to the number of spatial dimensions.¹

Typical examples of long-range interactions are Coulomb, dipolar, and hydrodynamic interactions. A multitude of different techniques exists to deal with specific long-range interactions in computer simulations. Examples are the reaction field method [55, 56], the fast multipole method [57], the Lekner method [100], and the Ewald summation method [58].

In this chapter, we want to present the Ewald summation method for dipolar particles, since these particles are of central importance in this thesis. The Ewald summation method is the most widely used and accepted technique to treat long-range dipolar interactions [58, 101]. Note only is the Ewald expression accurate, it can also be evaluated efficiently in computer simulations.

To derive the dipolar Ewald scheme, it is convenient to first consider the long-range interactions in ionic systems.

5.1. The Ewald sum in three-dimensional ionic bulk systems

Here, we will present the derivation of the Ewald expressions for the potential energy of a system consisting of charged particles in three dimensions. Derivations of and details on the Ewald summation method can be found in Refs. [58, 68, 102–105]. Here, we will closely follow the derivation detailed in Ref. [68].

To arrive at an Ewald expression for the energy of dipolar systems, it is convenient to first look at a system interacting via Coulomb interactions. Consider a cell consisting of N charged particles within a cubic volume V of side length L that is electrically neutral, i.e., $\sum_{i=1}^N q_i = 0$, where q_i is the charge of particle i . The potential energy of this N -particle system is given by

$$U_C = \frac{1}{2} \sum_{i=1}^N q_i \phi(\mathbf{r}_i), \quad (5.1)$$

where $\phi(\mathbf{r}_i)$ is the electrostatic potential that particle i experiences. If we introduce periodic replicas of the cell in all the spatial dimensions, we obtain

$$\phi(\mathbf{r}_i) = \sum'_{\mathbf{n}} \sum_{j=1}^N \frac{q_j}{|\mathbf{r}_{ij} + \mathbf{n}|} \quad (5.2)$$

for the electrostatic potential with $\{\mathbf{n}\} = \{(n_x L, n_y L, n_z L) | n_x, n_y, n_z \in \mathbb{Z}\}$. The prime at the first summation symbol indicates that the $j = i$ summation is omitted for $\mathbf{n} = 0$.

¹In that case the interaction energy of a single particle with all the other particles of an infinitely extended system is not a convergent expression. The expression can, however, be conditionally convergent. In the Ewald method, the summation of the conditionally convergent expression for the interaction energy is carried out in such a way that one arrives at a well defined value.

To derive an Ewald expression, consider the charge distribution

$$\rho_i(\mathbf{r}') = \sum_{\mathbf{n}}' \sum_{j=1}^N q_i \delta(\mathbf{r}' - \mathbf{r}_j + \mathbf{n}) \quad (5.3)$$

associated with the potential (5.2) (i.e., the charge distribution as seen by particle i). The key idea in the Ewald summation method is to rewrite this charge distribution in a suitable way to speed up the convergence of the electrostatic potential.

In a first step, a Gaussian charge density of opposite sign is associated with each δ -contribution in Eq. (5.3), i.e.,

$$\rho_{j,\mathbf{n}}(\mathbf{r}') = -q_j \left(\frac{\alpha}{\sqrt{\pi}} \right) \exp[-\alpha^2(\mathbf{r}' - \mathbf{r}_j + \mathbf{n})^2], \quad (5.4)$$

which satisfies

$$\int \rho_{j,\mathbf{n}}(\mathbf{r}') d\mathbf{r}' = -q_j. \quad (5.5)$$

Note that α is an arbitrary positive and real parameter that controls the width of the Gaussian charge density. Then we can define the charge distribution

$$\rho_i^{(1)} = \sum_{\mathbf{n}}' \sum_{j=1}^N [\delta(\mathbf{r}' - \mathbf{r}_j + \mathbf{n}) + \rho_{j,\mathbf{n}}(\mathbf{r}')], \quad (5.6)$$

which can be understood as a set of screened charges. The charge distribution $\rho_i^{(1)}$ results in the potential

$$\phi^{(1)}(\mathbf{r}_i) = \sum_{\mathbf{n}}' \sum_{j=1}^N q_j \frac{\text{erfc}(\alpha|\mathbf{r}_{ij} + \mathbf{n}|)}{|\mathbf{r}_{ij} + \mathbf{n}|}, \quad (5.7)$$

which decays much more rapidly than the one associated with the original distribution. Here, erfc is the complementary error function [106].

To account for the artificially introduced Gaussian charges, consider the difference

$$\rho_i(\mathbf{r}') - \rho_i^{(1)}(\mathbf{r}') = - \sum_{\mathbf{n}}' \sum_{j=1}^N \rho_{j,\mathbf{n}}(\mathbf{r}'), \quad (5.8)$$

which we separate into two parts:

$$\rho^{(2)}(\mathbf{r}') = - \sum_{\mathbf{n}} \sum_{j=1}^N \rho_{j,\mathbf{n}}(\mathbf{r}') \quad (5.9)$$

$$= \sum_{\mathbf{n}} \sum_{j=1}^N q_i \left(\frac{\alpha}{\sqrt{\pi}} \right)^3 \exp[-\alpha^2(\mathbf{r}' - \mathbf{r}_j + \mathbf{n})^2] \quad (5.10)$$

$$\rho_i^{(3)}(\mathbf{r}') = \rho_{i,0}(\mathbf{r}') \quad (5.11)$$

$$= -q_i \left(\frac{\alpha}{\sqrt{\pi}} \right)^3 \exp[-\alpha^2(\mathbf{r}' - \mathbf{r}_i)^2] \quad (5.12)$$

The sum in Eq. (5.10) can then be carried out without any restrictions, i.e., the charges now vary periodically in space.

This suggests to write down the corresponding potential in the reciprocal space spanned by the lattice vectors $\{\mathbf{k}\} = \{(2\pi m_x/L, 2\pi m_y/L, 2\pi m_z/L) | m_x, m_y, m_z \in \mathbb{Z}\}$. The resulting potential is then given by [68]

$$\phi^{(2)}(\mathbf{r}) = \frac{4\pi}{V} \sum_{\mathbf{k} \neq 0} \sum_{j=1}^N \frac{q_j}{k^2} \exp\left(-\frac{k^2}{4\alpha^2}\right) \exp(-i\mathbf{k} \cdot \mathbf{r}_{ij}) + \phi_{\text{LR}}^{(2)}(\mathbf{r}). \quad (5.13)$$

The convergence of Eq. (5.13) occurs rapidly due to the exponential damping with $-k^2/4\alpha^2$. The second term on the right hand side of Eq. (5.13) is the so-called long-range potential that represents the Fourier coefficients for $\mathbf{k} = 0$ in the expansion. It is given by

$$\phi_{\text{LR}}^{(2)}(\mathbf{r}) = \frac{4\pi}{V} \frac{\mathbf{r}_i \cdot \mathbf{M}}{2\epsilon + 1}, \quad (5.14)$$

if the central cell and all the replicas make up a large sphere that is surrounded by a medium with dielectric constant ϵ [68]. Further, note that

$$\mathbf{M} = \sum_{j=1}^N q_j \mathbf{r}_j. \quad (5.15)$$

The potential associated with the charge distribution $\rho_i^{(3)}$ [Eq. (5.12)] can be shown to be [68]

$$\phi^{(3)}(\mathbf{r}) = -q_i \frac{2\alpha}{\sqrt{\pi}}. \quad (5.16)$$

Combining Eqs. (5.7), (5.13), (5.14), and (5.16) enables us to write down the total electrostatic potential of the system as

$$U_{\text{C}}^{3\text{d}} = U_{\text{CR}}^{3\text{d}} + U_{\text{CF}}^{3\text{d}} + U_{\text{CS}}^{3\text{d}} + U_{\text{CLR}}^{3\text{d}}, \quad (5.17)$$

where

$$U_{\text{CR}}^{3\text{d}} = \frac{1}{2} \sum_{i=1}^N q_i \phi^{(1)}(\mathbf{r}_i) \quad (5.18)$$

$$= \frac{1}{2} \sum_{i=1}^N \sum_{j=1}^N \sum_{\mathbf{n}}' q_i q_j \frac{\text{erfc}(\alpha |\mathbf{r}_{ij} + \mathbf{n}|)}{|\mathbf{r}_{ij} + \mathbf{n}|} \quad (5.19)$$

$$U_{\text{CF}}^{3\text{d}} = \frac{1}{2} \sum_{i=1}^N q_i [\phi^{(2)}(\mathbf{r}_i) - \phi_{\text{LR}}^{(2)}(\mathbf{r}_i)] \quad (5.20)$$

$$= \frac{2}{\pi} \sum_{i=1}^N \sum_{j=1}^N \sum_{\mathbf{k} \neq 0} \frac{q_i q_j}{k^2} \exp\left(-\frac{k^2}{4\alpha^2}\right) \exp(-i\mathbf{k} \cdot \mathbf{r}_{ij}) \quad (5.21)$$

$$U_{\text{CLR}}^{3\text{d}} = \frac{1}{2} \sum_{i=1}^N q_i \phi_{\text{LR}}^{(2)}(\mathbf{r}_i) \quad (5.22)$$

$$= \frac{2\pi}{V} \frac{M^2}{2\epsilon + 1} \quad (5.23)$$

$$U_{\text{CS}}^{3\text{d}} = \frac{1}{2} \sum_{i=1}^N q_i \phi^{(3)}(\mathbf{r}_i) \quad (5.24)$$

$$= -\frac{\alpha}{\sqrt{\pi}} \sum_{i=1}^N q_i^2. \quad (5.25)$$

All of the above expressions converge very rapidly, which enables an efficient calculation of the particle interactions in simulations.

5.2. The Ewald sum in three-dimensional dipolar bulk systems

In a next step, we want to present the general idea behind the derivation of the Ewald sum for the dipole-dipole potential. Here, we again closely follow the derivation detailed in Ref. [68].

The total energy of a set of point dipoles in a bulk system with periodic replicas is given by

$$U_{\text{D}}^{3\text{d}} = \frac{1}{2} \sum_{i=1}^N \sum_{j=1}^N \sum_{\mathbf{n}}' U^{\text{D}}(\mathbf{r}_{ij} + \mathbf{n}, \boldsymbol{\mu}_i, \boldsymbol{\mu}_j), \quad (5.26)$$

where U^{D} is defined in Eq. (3.9). We observe that

$$U^{\text{D}}(\mathbf{r}_{ij}, \boldsymbol{\mu}_i, \boldsymbol{\mu}_j) = (\boldsymbol{\mu}_i \nabla_i) (\boldsymbol{\mu}_j \nabla_j) \psi(r_{ij}), \quad (5.27)$$

where

$$\psi(r_{ij}) = \frac{1}{r_{ij}} \quad (5.28)$$

is the electrostatic potential of a unit point charge. Hence, by making use of the fact that $q_i \rightarrow (\boldsymbol{\mu}_i \nabla_i)$ and $q_j \rightarrow (\boldsymbol{\mu}_j \nabla_j)$ one can obtain the Ewald expression for the dipole-dipole interaction

from the corresponding ionic one. The total potential energy of the dipolar system can hence be written as

$$U_D^{3d} = \frac{1}{2} \sum_{i=1}^N \sum_{j=1}^N \sum_{\mathbf{n}}' (\boldsymbol{\mu}_i \nabla_i) (\boldsymbol{\mu}_j \nabla_j) \psi(|\mathbf{r}_{ij} + \mathbf{n}|). \quad (5.29)$$

By using the results from the previous section [Eqs. (5.18), (5.20), and (5.22)], we find

$$\psi_R(r_{ij}) = \frac{\text{erfc}(\alpha r_{ij})}{r_{ij}}, \quad (5.30)$$

$$\psi_F(\mathbf{r}_{ij}) = \frac{4\pi}{V} \sum_{\mathbf{k} \neq 0} \frac{1}{k^2} \exp\left(-\frac{k^2}{4\alpha^2}\right) \exp(-i\mathbf{k} \cdot \mathbf{r}_{ij}), \quad (5.31)$$

and

$$\psi_{LR}(\mathbf{r}_i, \mathbf{r}_j) = \frac{4\pi}{V} \frac{\mathbf{r}_i \cdot \mathbf{r}_j}{2\epsilon + 1} \quad (5.32)$$

for the so-called real, Fourier, and long-range parts of ψ . Note that it is not possible to obtain an expression for the self contribution in this way. The reason for this is that Eq. (5.16) is a constant expression. For a derivation of the self energy contribution, we refer the reader to Ref. [68]. There, it is shown that the total self energy is given by

$$U_{DS}^{3d} = -\frac{2\alpha}{3\sqrt{\pi}} \sum_{i=1}^N \mu_i^2. \quad (5.33)$$

As in Eq. (5.17), the total interaction energy can be split up into four different contributions:

$$U_D^{3d} = U_{DR}^{3d} + U_{DF}^{3d} + U_{DLR}^{3d} + U_{DS}^{3d} \quad (5.34)$$

Calculating the energies, we find

$$U_{DR}^{3d} = \frac{1}{2} \sum_{i=1}^N \sum_{j=1}^N \sum_{\mathbf{n}}' (\boldsymbol{\mu}_i \nabla_i) (\boldsymbol{\mu}_j \nabla_j) \psi_R(r_{ij}) \quad (5.35)$$

$$= -\frac{1}{2} \sum_{i,j=1}^N \sum_{\mathbf{n}}' [B(|\mathbf{r}_{ij} + \mathbf{n}|) \boldsymbol{\mu}_i \cdot \boldsymbol{\mu}_j + C(|\mathbf{r}_{ij} + \mathbf{n}|) [\boldsymbol{\mu}_i \cdot (\mathbf{r}_{ij} + \mathbf{n})] [\boldsymbol{\mu}_j \cdot (\mathbf{r}_{ij} + \mathbf{n})]] \quad (5.36)$$

$$U_{DF}^{3d} = \frac{1}{2} \sum_{i=1}^N \sum_{j=1}^N (\boldsymbol{\mu}_i \nabla_i) (\boldsymbol{\mu}_j \nabla_j) \psi_F(r_{ij}) \quad (5.37)$$

$$= \frac{2\pi}{V} \sum_{\mathbf{k} \neq 0} \frac{1}{k^2} \exp\left(-\frac{k^2}{4\alpha^2}\right) \tilde{M}(\mathbf{k}) \tilde{M}^*(\mathbf{k}) \quad (5.38)$$

$$U_{DLR}^{3d} = \frac{1}{2} \sum_{i=1}^N \sum_{j=1}^N (\boldsymbol{\mu}_i \nabla_i) (\boldsymbol{\mu}_j \nabla_j) \psi_{LR}(r_{ij}) \quad (5.39)$$

$$= \frac{2\pi}{2\epsilon + 1} \frac{M^2}{V}, \quad (5.40)$$

where

$$\tilde{M}(\mathbf{k}) = \sum_{i=1}^N (\boldsymbol{\mu}_i \cdot \mathbf{k}) \exp(-i\mathbf{k} \cdot \mathbf{r}_i) \quad (5.41)$$

and

$$B(r) = -\frac{1}{r^3} \left[\frac{2\alpha r}{\sqrt{\pi}} \exp(-\alpha^2 r^2) + \operatorname{erfc}(\alpha r) \right] \quad (5.42)$$

$$C(r) = \frac{1}{r^5} \left[\frac{2\alpha r}{\sqrt{\pi}} (3 + 2\alpha^2 r^2) \exp(-\alpha^2 r^2) + 3\operatorname{erfc}(\alpha r) \right]. \quad (5.43)$$

The above Ewald expressions can be readily used in computer simulations. The expressions for the forces and torques, which are essential for MD, LD, and BD simulations, can be found in Appendix D.1.

Note that we use conducting boundary conditions throughout this thesis. As a consequence, we set $\epsilon = \infty$ in Eq. (5.39), which results in the long-range contribution to the energy vanishing.

5.3. The Ewald sum in quasi-two-dimensional dipolar systems

In quasi-two-dimensional systems, the particles are confined to a two-dimensional plane while they are free to rotate in all the spatial directions. In this section, we will present the Ewald sum of dipolar particles in such geometries. However, we will not derive this expression, since the derivation proceeds along similar lines as the ones in the previous sections. We refer the reader to [107–109] for further details.

The Ewald sum for the interaction energy of the quasi-two-dimensional system is given by

$$\begin{aligned} U_D^{2d} = & -\frac{1}{2} \sum_{i,j=1}^N \sum_{\mathbf{n}}' [B(|\mathbf{r}_{ij} + \mathbf{n}|) \boldsymbol{\mu}_i \cdot \boldsymbol{\mu}_j + C(|\mathbf{r}_{ij} + \mathbf{n}|) [\boldsymbol{\mu}_i \cdot (\mathbf{r}_{ij} + \mathbf{n})] [\boldsymbol{\mu}_j \cdot (\mathbf{r}_{ij} + \mathbf{n})]] \\ & + \frac{\pi}{A} \sum_{\mathbf{G} \neq 0} \left[\frac{\operatorname{erfc}(G/2\alpha)}{G} F_{\parallel}(\mathbf{G}) F_{\parallel}^*(\mathbf{G}) + \left[\frac{2\alpha}{\sqrt{\pi}} \exp\left(-\frac{G^2}{4\alpha^2}\right) \right. \right. \\ & \left. \left. - G \operatorname{erfc}\left(\frac{G}{2\alpha}\right) \right] F_{\perp}(\mathbf{G}) F_{\perp}^*(\mathbf{G}) \right] + \frac{2\sqrt{\pi}\alpha}{A} \sum_{i,j=1}^N \mu_i^z \mu_j^z - \frac{2\alpha^3}{3\sqrt{\pi}} \sum_{i=1}^N |\boldsymbol{\mu}_i^{\parallel}|^2 \end{aligned} \quad (5.44)$$

with

$$F_{\parallel}(\mathbf{G}) = \sum_{i=1}^N (\mathbf{G} \cdot \boldsymbol{\mu}_i^{\parallel}) \exp(i\mathbf{G} \cdot \mathbf{r}_i) \quad (5.45)$$

$$F_{\perp}(\mathbf{G}) = \sum_{i=1}^N \mu_i^{\perp} \exp(i\mathbf{G} \cdot \mathbf{r}_i). \quad (5.46)$$

In Eqs. (5.44), (5.45), and (5.46), $\boldsymbol{\mu}_i^{\parallel}$ denotes the in-plane components of the dipole moment $\boldsymbol{\mu}_i$, while μ_i^z denotes the out-of-plane one. Moreover, the lattice vectors are given by $\{\mathbf{G}\} = \{(2\pi m_x/L, 2\pi m_y/L) | m_x, m_y \in \mathbb{Z}\}$, where L is the length of the simulation box.

The Ewald expressions for the forces and torques in quasi-two-dimensional systems can be found in Appendix D.2.

5.4. Parallelization

Calculating the particle interactions in computer simulations can be a very time-consuming process. Particularly the evaluation of long-range interactions can require a significant amount of time. For the work of this thesis, we have parallelized the numerical algorithms of the calculations of the interactions. We optimized the short-range interactions as well as the long-range ones. In particular, we parallelized the evaluation of the Ewald sum [Secs. 5.2 and 5.3 and Appendices D.1 and D.2]. For this purpose, we used OpenMP [110], MPI [111], and CUDA [112].

OpenMP

Open Multiprocessing (OpenMP) is an API that allows for shared memory multiprocessing programming. In practice, it is a convenient way to address and utilize all the cores of a CPU.

MPI

A Message Passing Interface (MPI) application typically consists of multiple processes that communicate with each other. Computational problems can then be split up between these processes. In contrast to an application utilizing OpenMP, MPI processes can be distributed over different CPUs and computers.

CUDA

Compute Unified Device Architecture (CUDA) allows for the access of the resources of and communication with graphics processing units (GPU). The huge number of cores on a GPU can then be used to perform numerical calculations.

The OpenMP as well as the MPI parallelization were used extensively for the work of this thesis. These parallelizations offer a (almost) linear speed up with the number of cores and processors for sufficiently large systems.

Even though we also parallelized the Ewald sum with CUDA, the respective implementation was hardly used in practice, since too little performance was gained. The reason for this is the fact that every core on the GPU needs the positional information of all the particles to evaluate the Ewald expressions. As a consequence a considerable amount of data has to be transferred between the GPU and the CPU, which causes a significant slowdown of the simulation.

6. Phase transitions and density distributions

Some of the clustering phenomena that we will investigate later on are related to a first-order phase transition. Here, we will briefly introduce the terminology and concepts that are important in this regard. Moreover, we will introduce density functional theory in this chapter, which we will use in the analyzes of the structural and phase behavior of the systems studied in this thesis.

6.1. The vapor-liquid phase transitions

A phase transition is the transition from one state of a medium into another one. During a phase transition some of the properties of the medium, such as the density or the magnetization, undergo a change.

Phase transitions fall into different categories: Within the Ehrenfest classification, phase transitions are labeled by the lowest derivative of the free energy with respect to a thermodynamic variable that has a discontinuity. For instance, in a second order phase transition, the second derivative of the free energy is not continuous.

A vapor-liquid phase transition has characteristics of both a first as well as a second order phase transition. Consider two arbitrary state points in the phase diagram of a system exhibiting (only) a vapor-liquid phase transition. Clearly, two such points can be connected by a path in the phase diagram. If one of these state points corresponds to a vapor state and the other to a liquid state, the first and/or the second derivative of the free energy exhibit a discontinuity along such a path.

Paths at and above the so-called critical temperature lack the discontinuity of the first derivative. The phase transition is of second order and it is no longer possible to classify the fluid as either gaseous or liquid.

At the parameters at which the first derivative of the free energy is discontinuous, no thermodynamic equilibrium state exists. This region in the phase diagram is called the coexistence region. Within this region, density fluctuations can cause the system to phase separate during which domains of both the vapor and the liquid phase form. For suitable thermodynamic parameters in the coexistence region, infinitesimal fluctuations are sufficient to give rise to this process. The region in the phase diagram where this is true is called the spinodal or unstable region. Here, the system is linearly unstable against density fluctuations, i.e., any fluctuation in the density increases exponentially. The separation process in this region is called spinodal decomposition. It typically proceeds according to a power law with domains growing proportionally to t^α . The parameter α can have different values depending on the stage of domain formation [113–115]. A famous theory on the domain growth of phase separating systems is the Lifshitz-Slyozov theory [116]. In this theory, the parameter α is found to be equal to $1/3$.

Linear instability against density fluctuations is not given in the entire coexistence region. Finite density fluctuations are necessary to cause the system to decompose into different phases inside the binodal or metastable region. This decomposition process is called nucleation [117].

6.2. Density functional theory

Density functional theory (DFT) is a method that can be used to find the density distribution of systems in thermal equilibrium. At the same time, it allows for, e.g., the calculation of the Helmholtz free energy of a system. In this section, we describe the basic concepts of (canonical) DFT.

6.2.1. The extremum condition

The Helmholtz free energy functional (in the absence of an external field) can be written as [118]

$$\mathcal{F}[\rho] = \mathcal{F}^{\text{id}}[\rho] + \mathcal{F}^{\text{ex}}[\rho], \quad (6.1)$$

where ρ is the one-particle density distribution, \mathcal{F}^{id} the ideal part of the free energy, and \mathcal{F}^{ex} its excess part. The former contribution to the free energy stems from the configuration of the particles and is given by

$$\mathcal{F}^{\text{id}}[\rho] = k_B T \int d^3r \rho(\mathbf{r}) [\log(\Lambda^3 \rho(\mathbf{r})) - 1], \quad (6.2)$$

where $\Lambda = \sqrt{h^2/2\pi m k_B T}$ is the thermal wavelength and h the Planck constant. The latter contribution \mathcal{F}^{ex} is solely due to the interactions between the particles. Note that this excess free energy \mathcal{F}^{ex} is in general unknown. In practice, it is therefore often necessary to find suitable approximate expressions for \mathcal{F}^{ex} .

The central tenet of canonical DFT is that the Helmholtz free energy functional is extremal at the equilibrium density ρ_{eq} under the constraint that the particle number N is conserved. This means that [119]

$$\left. \frac{\delta \mathcal{F}[\rho]}{\delta \rho(\mathbf{r})} \right|_{\rho_{\text{eq}}} = 0 \quad (6.3)$$

under the condition that

$$\int d^3r \rho_{\text{eq}}(\mathbf{r}) = N. \quad (6.4)$$

From the Helmholtz free energy of a system, which corresponds to the value of the Helmholtz free energy functional at the equilibrium density, all the thermodynamic properties of the system can be derived [120].

6.2.2. Perturbation expansion of the canonical potential

It is very difficult to actually solve Eq. (6.3). To a large extent, this is due to the excess free energy being in general unknown. Hence, instead of considering the full excess free energy, one often considers its expansion up to second order in the density. This perturbation expansion of the free energy was originally proposed by Ramakrishnan and Yussouff in the context of fluid-solid transitions [121]. The difference between the Helmholtz free energy of a volume V of a system with non-uniform density ρ and a reference system with homogeneous density ρ_0 (up to second order in the density) is given by [122]

$$\begin{aligned} \frac{\Delta \mathcal{F}}{V} = & \frac{1}{\beta V} \int_V d^3r [\log(\Lambda^3 \rho(\mathbf{r})) - 1] - \frac{1}{\beta V} \int_V d^3r \rho_0 [\log(\Lambda^3 \rho_0) - 1] \\ & - \frac{1}{2\beta V} \int_V d^3r_1 \int_{\mathbb{R}^3} d^3r_2 c(\mathbf{r}_1 - \mathbf{r}_2) \Delta \rho(\mathbf{r}_1) \Delta \rho(\mathbf{r}_2). \quad (6.5) \end{aligned}$$

In Eq. (6.5), $\Delta\rho(\mathbf{r}) = \rho(\mathbf{r}) - \rho_0$ with $\int_V d^3r \Delta\rho(\mathbf{r}) = 0$ and c is the direct correlation function of the system at homogeneous density ρ_0 .

The direct correlation function alone contains the information about the particle interactions. It can be defined as a derivative of the excess free energy:

$$c(\mathbf{r}_1, \mathbf{r}_2) = -\beta \frac{\delta^2 \mathcal{F}^{\text{ex}}[\rho]}{\delta\rho(\mathbf{r}_1)\delta\rho(\mathbf{r}_2)} \quad (6.6)$$

Note that in a homogeneous system, the direct correlation function only depends on the distance vector between its two arguments:

$$c(\mathbf{r}_1 - \mathbf{r}_2) = c(\mathbf{r}_1, \mathbf{r}_2) \quad (6.7)$$

Eq. (6.5) allows for the calculation of the free energy difference between density distributions. In particular, Eq. (6.5) can be used to evaluate which density distribution is preferred by a system.

6.2.3. The direct correlation function

In order to find the Helmholtz free energy difference between two systems up to second order in the density, the direct correlation function of the system is needed. However, it is typically a very difficult task to obtain this function. Therefore, one often uses an approximate expression for the correlation function. In this section, we will present some of the most commonly used schemes to obtain suitable approximations.

The random phase approximation

Consider a system interacting via the pair potential

$$v_\lambda(\mathbf{r}_1, \mathbf{r}_2) = v_0(\mathbf{r}_1, \mathbf{r}_2) + \lambda w(\mathbf{r}_1, \mathbf{r}_2). \quad (6.8)$$

Here, v_0 is the interaction potential of a reference system and w is a perturbation in the potential. The excess free energy of the system characterized by the full potential v_1 can then be written as [118]

$$\mathcal{F}^{\text{ex}}[\rho] = \mathcal{F}_0^{\text{ex}}[\rho] + \frac{1}{2} \int \int \rho(\mathbf{r}_1)\rho(\mathbf{r}_2)w(\mathbf{r}_1, \mathbf{r}_2)d\mathbf{r}_1d\mathbf{r}_2 + \mathcal{F}^{\text{corr}}[\rho] \quad (6.9)$$

with

$$\mathcal{F}^{\text{corr}}[\rho] = \frac{1}{2} \int_0^1 d\lambda \int \int \rho(\mathbf{r}_1)\rho(\mathbf{r}_2)h(\mathbf{r}_1, \mathbf{r}_2, \lambda)w(\mathbf{r}_1, \mathbf{r}_2)d\mathbf{r}_1d\mathbf{r}_2. \quad (6.10)$$

Here, h is the total correlation function defined below [Sec. 6.2.3], which describes the spatial correlations between the particles.

The quantity $\mathcal{F}^{\text{corr}}$ in Eqs. (6.9) and (6.10) is the contribution to \mathcal{F}^{ex} due to correlations introduced by the perturbation w [118]. Neglecting this correlation contribution and calculating the direct correlation function via Eq. (6.6) yields [118]

$$c(\mathbf{r}_1, \mathbf{r}_2) \approx c_0(\mathbf{r}_1, \mathbf{r}_2) - \beta w(\mathbf{r}_1, \mathbf{r}_2), \quad (6.11)$$

where c_0 is the direct correlation function of the reference system. This approximation is called the random phase approximation (RPA) to the direct correlation function. It corresponds to treating the effects of the perturbation w in a mean-field approximation.

The Ornstein-Zernike equation

The Ornstein-Zernike (OZ) equation

$$h(\mathbf{r}_1, \mathbf{r}_2) = c(\mathbf{r}_1, \mathbf{r}_2) + \int d\mathbf{r}_3 c(\mathbf{r}_1, \mathbf{r}_3) \rho(\mathbf{r}_3) h(\mathbf{r}_3, \mathbf{r}_2) \quad (6.12)$$

is an integral equation relating the direct correlation function c to the total correlation function h . The total correlation function describes spatial correlations between the particles and can be written as [118]

$$h(\mathbf{r}_1, \mathbf{r}_2) = g(\mathbf{r}_1, \mathbf{r}_2) - 1, \quad (6.13)$$

where [105, 118]

$$g(\mathbf{r}_1, \mathbf{r}_2) = \frac{1}{\rho(\mathbf{r}_1)\rho(\mathbf{r}_2)} \left\langle \sum_i \sum_{j \neq i} \delta(\mathbf{r}_1 - \mathbf{r}_i) \delta(\mathbf{r}_2 - \mathbf{r}_j) \right\rangle \quad (6.14)$$

is the pair correlation function. Assuming spatial homogeneity, Eq. (6.12) simplifies to ($\mathbf{r} = \mathbf{r}_1 - \mathbf{r}_2$)

$$h(\mathbf{r}) = c(\mathbf{r}) + \rho_0 \int d\mathbf{r}' c(\mathbf{r} - \mathbf{r}') h(\mathbf{r}'). \quad (6.15)$$

This can easily be seen by recalling Eq. (6.7) and realizing that Eq. (6.14) reduces to

$$g(\mathbf{r}_1, \mathbf{r}_2) = \frac{V}{N^2} \left\langle \sum_i \sum_{j \neq i} \delta(\mathbf{r} - \mathbf{r}_{ij}) \right\rangle = g(\mathbf{r}) \quad (6.16)$$

for spatially homogeneous systems.

Solving the OZ Eq. (6.12) gives an expression for the direct correlation function (and the total correlation function), which is needed in the calculation of the free energy difference (6.5). In order to solve the OZ Eq. (6.12) a closure relation has to be prescribed. Two very commonly used closures are the Percus-Yevick closure and the mean spherical approximation. These will be described in the following.

The mean spherical approximation

The mean spherical approximation (MSA) is a closure that can be used in uniform systems of particles interacting via a hard core of diameter d plus a tail, which corresponds to potentials of the form

$$v(\mathbf{r}) = \begin{cases} \infty, & r \leq d \\ w(\mathbf{r}), & r > d \end{cases} \quad (6.17)$$

First, since the particles cannot come closer to each other than a distance d , one prescribes

$$g(r) = 0 \quad \text{if } r < d \quad (6.18)$$

in the MSA. Now note that it is widely accepted that the direct correlation function behaves asymptotically as the interparticle potential, which means that [118]

$$c(\mathbf{r}) \xrightarrow{r \rightarrow \infty} -\beta w(\mathbf{r}). \quad (6.19)$$

Hence, as a second relation, one imposes the behavior (6.19) on the direct correlation function for distances $r > d$, i.e.,

$$c(\mathbf{r}) = -\beta w(\mathbf{r}) \quad \text{if } r > d. \quad (6.20)$$

By using the relations (6.18) and (6.20), it becomes possible to solve the OZ Eq. (6.12) and find the total correlation function as well as the direct correlation function of the considered system.

The Percus-Yevick approximation

The Percus-Yevick (PY) approximation is a closure that has historically been very important, since it allows for an analytical calculation of the direct correlation function of a system of hard spherical particles of diameter d [cf. Sec. 3.5]. In the case of HSs, the PY closure relation is given by [118]

$$g(r) = 0, \quad r < d \quad (6.21)$$

$$c^{\text{PY}}(r) = 0, \quad r > d. \quad (6.22)$$

Here, the PY approximation can be seen as a limiting case of the MSA: By setting the tail potential w to zero in Eq. (6.17), the MSA closure relations (6.18) and (6.20) reduce to Eqs. (6.21) and (6.22).

Solving the OZ Eq. (6.12) by making use of the closure relations (6.21) and (6.22), one finds [118, 123, 124]

$$c^{\text{PY}}(x) = \begin{cases} -\lambda_1 - 6\eta\lambda_2x - \frac{1}{2}\eta\lambda_1x^3, & x < 1 \\ 0, & x > 1 \end{cases} \quad (6.23)$$

for the direct correlation function, where $x = r/d$, $\eta = \pi\rho d^3/6$ is the packing fraction, and

$$\lambda_1 = \frac{(1 + 2\eta)^2}{(1 - \eta)^4} \quad (6.24)$$

$$\lambda_2 = -\frac{(2 + \eta)^2}{4(1 - \eta)^4}. \quad (6.25)$$

Hard discs Hard discs (HDs) interact with each other via the HS potential (3.8). But in contrast to HSs, HDs refer to particles that interact via (3.8) in a two-dimensional geometry.

There does not exist an analytical expression for the direct correlation function of HDs in the PY closure. However, different approximations to the PY solution are known [125–127], with a very accurate one being given by [126, 127]

$$c_{2d}^{\text{PY}}(x) = -\Theta(1 - x)c(0)[1 - 4\eta + 4\eta\omega_2(x/2) + s_2x]. \quad (6.26)$$

Here, Θ is the Heaviside step function, $x = r/d$, and $\eta = \pi\rho/4$ is the two-dimensional packing fraction of the disc-like particles. Moreover,

$$c(0) = -\frac{1 + \eta + 3p\eta^2 - p\eta^3}{(1 - \eta)^3} \quad (6.27)$$

with

$$p = \frac{7}{3} - \frac{4\sqrt{3}}{\pi}, \quad (6.28)$$

$$\omega_2(x) = \frac{2}{\pi} [\arccos x - x\sqrt{1-x^2}], \quad (6.29)$$

and

$$s_2 = \frac{3\eta^2}{8} \left[\frac{8(1-2p) + (25-9p)p\eta - (7-3p)p\eta^2}{1 + \eta + 3p\eta^2 - p\eta^3} \right]. \quad (6.30)$$

7. Pattern formation of dipolar colloids in rotating fields: layering and synchronization in three dimensions

A characteristic feature of dipolar interactions is their anisotropy. Specifically, dipolar particles tend to favor a head-to-tail alignment. When driven by an external rotating field, the interactions can, on average, become attractive in the entire plane of the field and repulsive along its rotational axis. These averaged interactions can then facilitate the formation of layers for suitable thermodynamic parameters [40, 128].

The crucial assumption for the effective interaction to emerge is that the particles follow the field synchronously [37, 128]. While this is obviously fulfilled in systems of induced dipoles, less is known about the corresponding behavior of particles with permanent dipole moments, such as the (ferromagnetic) particles of a ferrofluid. Here, the individual orientations can be different from the one of the rotating field and thus synchronization can break down. Some time ago, Murashov and Patey showed in a computer simulations study [37] that layering can, in principle, also occur in systems of permanent dipoles. However, they considered only some selected state points.

In this chapter we use computer simulations and theoretical methods to explore, for a (permanent) magnetic many-particle system, the link between the collective, self-assembly behavior into layers, on the one hand, and the single-particle dynamics, on the other hand.

Specifically, we investigate a ferrofluid subjected to a rotating in-plane field, where the ferrofluid is modeled by a system of DSSs both by LD computer simulations and theory. As a first main result, we present in Sec. 7.3 a full nonequilibrium “phase” diagram indicating the domain of layer formation in the plane spanned by the frequency and strength of the driving field at constant equilibrium thermodynamic parameters. Secondly, to identify the role of mutual synchronization of the particles, we investigate in Sec. 7.5 the rotational dynamics within layered and unlayered states by analyzing suitable distribution functions. A similar strategy has recently been proposed in a dynamic density functional study of rod-like particles in rotating fields [129]. In Sec. 7.6 we show that the breakdown of layering observed at high frequencies in the ferrofluid system can be described by a single-particle theory similar to those used for field-driven single nanoparticles in viscous media [45]. In Sec. 7.7, we propose a simple equilibrium density functional approach to investigate the role of translational entropy for layering in synchronized ferrofluid systems. Sec. 7.8 is devoted to examining the influence of hydrodynamic interactions on the layering phenomenon. In particular, we look into whether layering is stable under the inclusion of solvent-mediated interactions. As a last point, we investigate the influence of the simulation method on the layer formation and the collective dynamic behavior of the particles in Sec. 7.9. We close the chapter with a brief summary and conclusions [Sec. 7.10].

Note that large parts of this chapter have been published in Refs. [38, 39].

7.1. Model and simulation methods

In our simulations we model the colloidal suspension, the colloidal particles of which carry a permanent dipole moment, by a system of DSSs [cf. Eq. (3.14)]. The solvent is not explicitly taken into account.

We investigate the system using LD simulations [see Sec. 4.2] with the corresponding equations of motion being given by Eqs. (4.26) and (4.27). In addition to the random, conservative, and friction torques, we consider an additional torque contribution stemming from an external field. The modified rotational equation of motion then takes the form

$$I\dot{\boldsymbol{\omega}}_i = \mathbf{T}_i^{\text{DSS}} + \mathbf{T}_i^{\text{ext}} - \zeta_{\text{R}}\boldsymbol{\omega}_i + \mathbf{T}_i^{\text{G}}, \quad (7.1)$$

where

$$\mathbf{T}_i^{\text{ext}} = \boldsymbol{\mu}_i \times \mathbf{B}^{\text{ext}}. \quad (7.2)$$

The quantity \mathbf{B}^{ext} is the applied external field, which rotates with frequency ω_0 in the $x-y$ -plane and is given by

$$\mathbf{B}^{\text{ext}}(t) = B_0(\mathbf{e}_x \cos \omega_0 t + \mathbf{e}_y \sin \omega_0 t). \quad (7.3)$$

To deal with the long-range dipolar interactions, we used the Ewald summation method with conducting boundaries in our simulations [see Sec. 5.2]. The equations of motion were integrated with a leapfrog algorithm as described in Sec. 4.1.1.

For convenience, we make use of reduced units as introduced in Sec. 4.6. Unless stated otherwise, the simulations were carried out with 864 particles at density $\rho^* = 0.1$, dipole moment $\mu^* = 3$, moment of inertia $I^* = 0.025$, and temperature $T^* = 1.35$. To verify our results, we also ran simulations with up to 4000 particles. The translational and rotational diffusion constant were chosen to be $D_0^{\text{T}*} = 0.1$ and $D_0^{\text{R}*} = 3$, respectively, and we used a time step of $\Delta t^* = 0.0025$. These values are consistent with those chosen in earlier LD studies of rotating dipolar systems [37]. We note, however, that the effects reported here also appear for other values of $D_0^{\text{T}*}$ and $D_0^{\text{R}*}$.

7.2. Zero field system

The zero field system that represents our starting point is characterized by a large dipolar coupling strength $\lambda = \mu^2/(k_B T \sigma^3) = \mu^{*2}/T^* \approx 6.7$ and a relatively low density. As expected for such a strongly coupled system, the particles self-assemble into chainlike structures [20, 130]. This can be seen in the snapshot depicted in Fig. 7.1(a). Our reason for considering a system of a coupling strength this high is that this seems to be a prerequisite for layer formation. Indeed, irrespective of the field strength, we did not observe any layering for values of λ that are smaller than approximately 4.6 (at the temperature $T^* = 1.35$).

Contrary to λ , our choice of the density is less restricted, since the layering phenomenon persists over a wide range of densities (at least up to $\rho^* = 0.4$). However, choosing the small density of $\rho^* = 0.1$ has the advantage of the layers being easily discernible.

7.3. The layering effect

We now consider the same system in rotating fields of various strengths B_0^* and frequencies ω_0^* . For sufficiently large B_0^* and not too high frequencies (see below), the particles arrange themselves

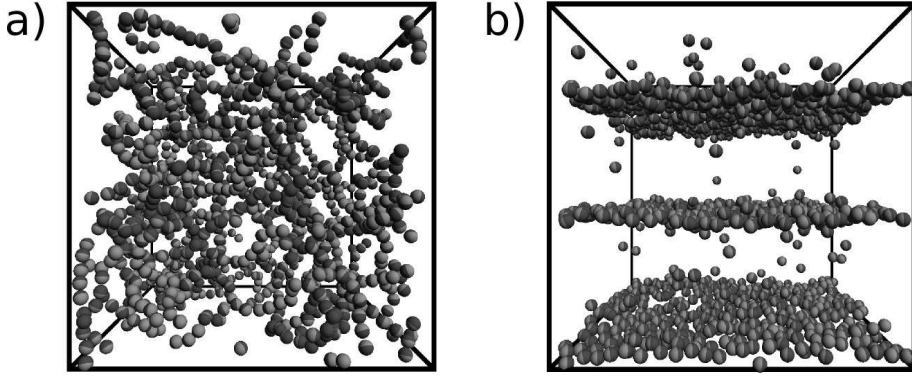


Figure 7.1.: (a) Snapshot of the system in zero field at $\rho^* = 0.1$, $T^* = 1.35$, and $\mu^* = 3$. (b) Snapshot of a system in a layered state. The strength and frequency of the field are $B_0^* = 12$ and $\omega_0^* = 15$, respectively.

into layers. An example of this is shown in Fig. 7.1(b). This phenomenon was first explained by Halsey, Anderson, and Martin [128]. They realized that the time-averaged potential between two particles i and j that rotate with the same angular frequency (given by the external field) and are aligned with each other, i.e., rotate circularly in a synchronized fashion with

$$\boldsymbol{\mu}_i(t) = \boldsymbol{\mu}_j(t) = \mu(\mathbf{e}_x \cos \omega_0 t + \mathbf{e}_y \sin \omega_0 t), \quad (7.4)$$

is given by

$$U^{\text{ID}}(\mathbf{r}_{ij}) = \tau^{-1} \int_{t_0}^{t_0+\tau} U^{\text{D}}(\mathbf{r}_{ij}, \boldsymbol{\mu}_i(t), \boldsymbol{\mu}_j(t)) dt = -\mu^2 \frac{(1 - 3 \cos^2 \Theta_{ij})}{2r_{ij}^3}. \quad (7.5)$$

In this equation, U^{D} is the dipole-dipole potential [see Eq. (3.9)], $\tau = 2\pi/\omega_0$ is the oscillation period, and Θ_{ij} is the angle between the interparticle vector \mathbf{r}_{ij} and the direction perpendicular to the plane of the field. As shown by the last line in Eq. (7.5), the time-averaged potential corresponds to an inverted dipolar (ID) potential, which is attractive if the angle Θ_{ij} satisfies $\cos^2 \Theta_{ij} < 1/3$, i.e., if the particles i and j are approximately in the same plane with respect to the field. Conversely, if the angle Θ_{ij} satisfies $1/3 < \cos^2 \Theta_{ij}$, the particles repel each other. This direction dependence of the ID potential explains why layers are a favorable configuration for a driven system in which essentially all the particles rotate synchronously. Note that for the above argument to hold, the translational motion of the particles must be small compared to their rotational motion [128].

In this context it is interesting to inspect the translational structure within the layers. In Fig. 7.2 we present simulation snapshots illustrating the typical in-plane structure of the system at low and high driving frequencies, respectively. At low frequencies one observes the presence of chains with head-to-tail alignment of the dipole moments. These chains do not rotate with the field. Such a rotation would be impossible due to the simple fact that there are too many neighboring particles. Instead the particles arrange themselves into new chains with other particles once the original configuration becomes energetically unfavorable [cf. Figs. 7.2(a) and 7.2(b)]. This process of rearranging is only possible for slowly rotating fields. Note that chains

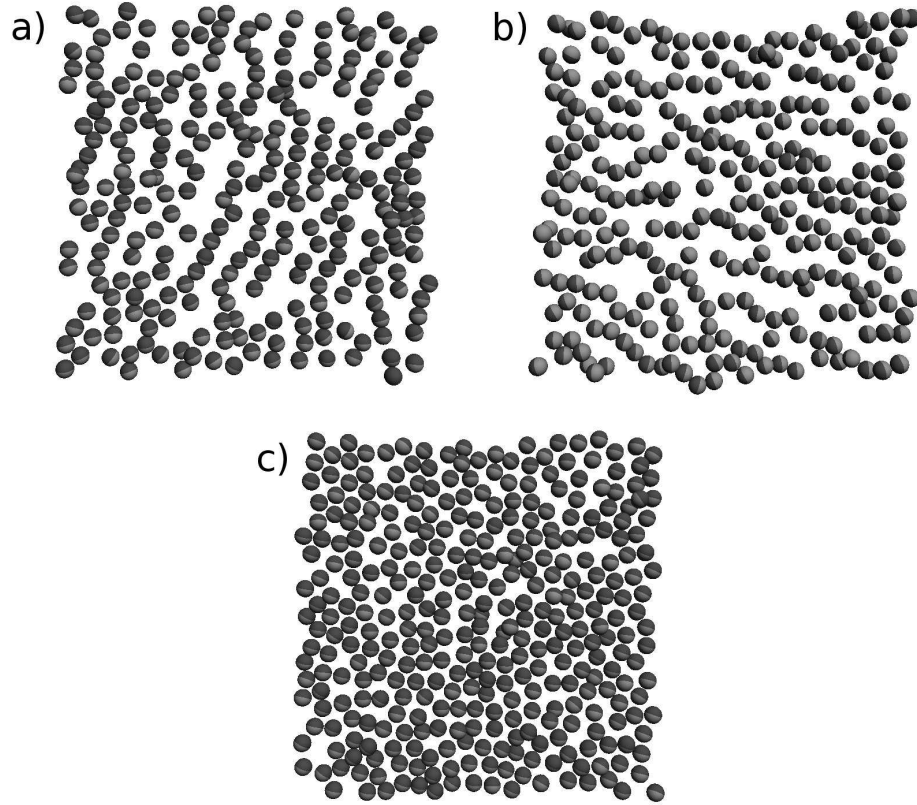


Figure 7.2.: Snapshot of the in-layer structure at $B_0^* = 9$, $\omega_0^* = 2$ (a) and $B_0^* = 10$, $\omega_0^* = 54$ (c). Snapshot (b) shows the layer in (a) after a quarter of the rotational period of the field has passed. The density within the layers can vary depending on the number of layers emerging.

are present in the layers at all times. With increasing ω_0 the chains disappear and the structure becomes more disordered and increasingly homogeneous as can be seen in Fig. 7.2(c). Note, that the disappearance of the chains progresses slowly and continuously, which makes it difficult to determine a precise driving frequency after which chains do not form anymore. Furthermore, there is no pronounced hexagonal order as observed in earlier studies [36], even though the particles tend to have six nearest neighbors at high ω_0 . This absence of pronounced in-plane order is probably a consequence of the low density considered ($\rho^* = 0.1$) and the Brownian random forces. Furthermore, depending on the initial conditions, we typically observe two or three layers in our simulation box ($N = 864$), which corresponds to an average vertical distance between the layers of about seven to ten particle diameters [see Fig. 7.1(b)].

In the following we aim to determine more precisely the range of frequencies and field strengths at which layering occurs. To do that, we need a suitably defined order parameter. We tested several ones and compared them with one another. The order parameter that we will use here is given by

$$\psi = \frac{1}{N} \sum_{i=1}^N \langle n_i \rangle, \quad (7.6)$$

where N is the total number of particles and n_i is defined as follows: Consider a sphere of radius r_0 around particle i . Divide that sphere into two parts, one of which is given by the points within the sphere whose distance vector to particle i together with the z -axis encloses an angle Θ satisfying $-0.5 < \cos \Theta < 0.5$ [see Fig. 7.3]. If there are more (less) particles in this equatorial volume than in the polar volume around particle i , set $n_i = 1$ (-1); if there are the same number of particles, set $n_i = 0$. Note that the radius r_0 was set to 8σ . Smaller as well as larger radii r_0

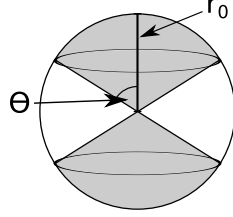


Figure 7.3.: Sketch of the polar and equatorial regions used in the definition of the order parameter ψ [Eq. (7.6)].

decrease the performance of the order parameter as we found by comparing the order parameter with the actual order observed in the system.

Representative examples for the behavior of the resulting order parameter at constant angular frequency but increasing field strength are given in Fig. 7.4. As can be seen, in all the cases the value of ψ grows with the field strength until it almost reaches a value of 1. Since the layers are usually not perfectly defined in our LD simulations, the order parameter typically takes on values that are slightly smaller than 1 even at very high field strengths.

One also finds from Fig. 7.4 that there is a qualitative difference in the behavior of ψ at high and low frequencies: The order parameter grows much more steeply at large frequencies, which means that the layers do not slowly emerge upon increasing the field strength but appear very rapidly.

By inspecting snapshots corresponding to a given value of the order parameter, it turned out that the value $\psi_0 \approx 0.6$ may serve as an (approximate) lower limit for layer formation.

Based on this criterion, we have scanned a broad range of frequencies and field strengths for the occurrence of layers. The results of this exploration of the parameter space are summarized in Fig. 7.5. Note that every simulation was started from a random configuration to avoid hysteresis-like effects.

The figure shows that the $\omega_0^* - B_0^*$ diagram is separated into a layered and a non-layered region. Upon increasing the frequency from zero, the boundary first remains at roughly constant field strength, until it begins to rise with the frequency. This behavior is mirrored in Fig. 7.4. The larger the frequency, the higher the field strength at which the order parameter attains large values.

In the following sections, we will discuss the emergence and breakdown of layering in the different frequency regimes in more detail. Before doing so, it is worth to briefly comment on a technical issue encountered in our exploration of the parameter space [see Fig. 7.5] that concerns the behavior of the rotational temperature T_{rot} [see Eq. (4.10)]. Upon increasing the driving frequency ω_0^* from zero (at fixed B_0^*), we typically also find T_{rot} to increase, while its translational counterpart T_{trans} [see Eq. (4.9)] stays approximately constant (close to the input value T). Similar temperature drifts have been observed in other nonequilibrium systems such as fluids in shear flow. In the latter context, the temperature is often redefined with respect to

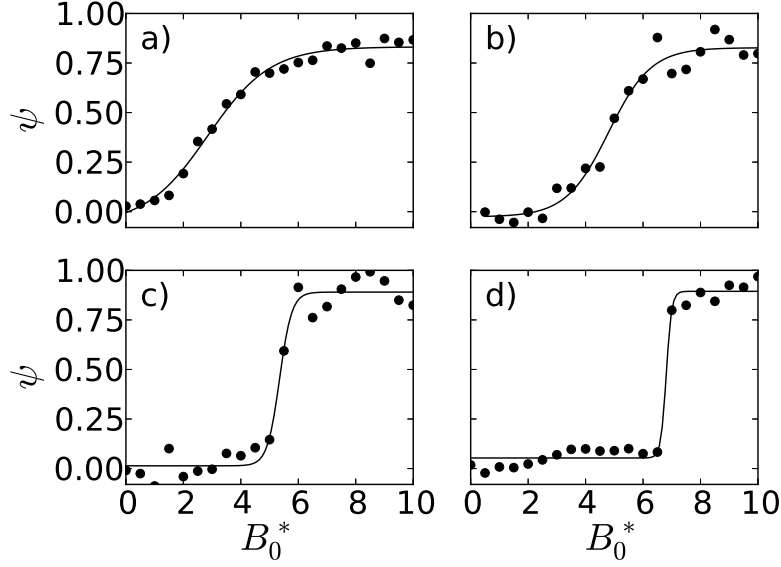


Figure 7.4.: The order parameter ψ at constant angular frequency (a) $\omega_0^* = 1$, (b) 20, (c) 30, (d) 40.

the differences between the actual velocity of the particle and that of the flow field [131]. Using a similar definition here (involving the difference between ω_i and ω_0), we find that this temperature is still not equal to T , but remains essentially constant over a broad range of frequencies. We also note that both the temperature drift and the actual location of the layer boundary in the $\omega_0^* - B_0^*$ diagram depend on the chosen value of the rotational friction constant.

7.4. Magnetization dynamics

As a starting point to understand the rotational dynamics within the layered and unlayered states, respectively, we consider in this section the behavior of the system-averaged, i.e., macroscopic, magnetization vector

$$\frac{\mathbf{M}(t)}{M_0} = \frac{1}{N\mu} \sum_{i=1}^N \boldsymbol{\mu}_i(t) \quad (7.7)$$

where $M_0 = N\mu$. The time-dependence of the Cartesian components of \mathbf{M} for three representative frequencies (and a large field strength) is illustrated in Fig. 7.6. Within the layered state ($\omega_0^* = 40$), the x - and y -components perform regular oscillations following those of the external field at constant phase difference. Furthermore, the amplitudes of M_x/M_0 and M_y/M_0 are close to their saturation value at all times. The z -component, on the other hand, is essentially zero. Taken altogether, the magnetization in the layered state can be written as

$$\mathbf{M}(t) \approx M_0[\mathbf{e}_x \cos(\omega_0 t + \delta) + \mathbf{e}_y \sin(\omega_0 t + \delta)], \quad (7.8)$$

where δ is the constant phase difference between $\mathbf{M}(t)$ and $\mathbf{B}^{\text{ext}}(t)$.

Substantially different behavior is found at frequencies beyond the layered regime, as illustrated by the data for $\omega_0^* = 60$ and 100 in Fig. 7.6. It is seen that the x - and y -component still

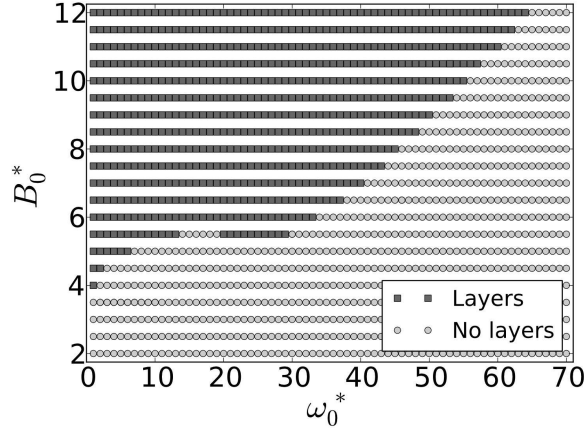


Figure 7.5.: Occurrence of layers depending on field strength and frequency of the driving field. The system parameters are chosen as described in Sec. 7.1.

perform oscillations, but their amplitudes are much smaller than in the layered state and, moreover, continuously decrease with increasing ω_0 . The z -component, on the other hand, remains negligible (as in the layered state). Interestingly, the change between the two behaviors of $\mathbf{M}(t)$ occurs rather suddenly. This is illustrated in Fig. 7.7, where we plot the absolute value of the total magnetization, i.e.,

$$\frac{M}{M_0} = \frac{1}{M_0} \langle |\mathbf{M}| \rangle \quad (7.9)$$

as a function of the frequency ω_0^* (at constant B_0^*). Also included are data for the in-plane magnetization $M_{\parallel} = \langle |\mathbf{M}(t) \cdot (\mathbf{e}_x + \mathbf{e}_y)| \rangle$. Consistent with Fig. 7.6(c), we find that the total and in-plane magnetization are essentially identical at all frequencies. In particular, both quantities display a pronounced drop at $\omega_0^* \approx 56$ corresponding to the boundary of the layered regime in Fig. 7.5.

So far we have focused on the behavior of the magnetization at a selected (large) field strength. However, motivated by the presence of an unlayered regime at small fields and frequencies [see Fig. 7.5], we plot in Fig. 7.8 the absolute value of $\mathbf{M}(t)$ as function of B_0^* at various fixed values of ω_0^* . The appearance of layers is indicated by the black circles, showing that a degree of magnetization of more than 80 percent is required for layer formation to occur. In the unlayered regime the values of M/M_0 are clearly substantially smaller. Note, however, that at small driving frequencies the increase of M/M_0 upon increasing B_0^* is not as sudden as that depicted in Fig. 7.7 (upon decreasing ω_0^*). Indeed, by comparing Figs. 7.8 and 7.4 we find that the magnetization behaves quite similar to the layer order parameter ψ discussed before. This underlines our view that layer formation and synchronous rotational motion are intimately related.

7.5. Microscopic rotational dynamics in the layered state

As mentioned earlier, the key argument for the appearance of the layers is that the time-averaged interaction between two fully synchronized rotating dipoles favors an in-plane configuration. In the following, we will investigate in more detail to what extent this assumption is actually fulfilled within the layered region indicated in Fig. 7.5 on a microscopic level. To this end, we consider

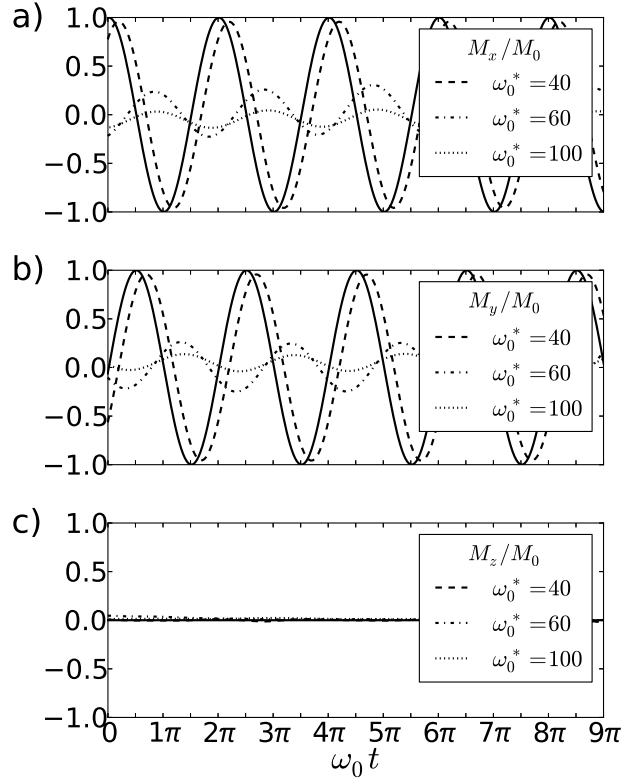


Figure 7.6.: Time dependence of the (a) x -, (b) y -, and (c) z -components of the normalized magnetization in a layered system ($\omega_0^* = 40$) and two unlayered systems ($\omega_0^* = 60$, $\omega_0^* = 100$) at constant field strength $B_0^* = 10$. The solid lines show the corresponding normalized components of the external field.

the distribution f of the phase differences ϕ_i between the dipolar vector of particle i in the $x - y$ -plane and the external field. More precisely, we define f as

$$f(\phi) = \frac{1}{N\Delta\phi} \left\langle \sum_{i=1}^N \Theta(\phi_i - n\Delta\phi) - \Theta(\phi_i - (n+1)\Delta\phi) \right\rangle, \quad (7.10)$$

where Θ is the Heaviside function, $\Delta\phi$ is the interval length to which we want to resolve the distribution, n is a positive integer or zero that satisfies $n\Delta\phi \leq \phi < (n+1)\Delta\phi$, and, as before, $\langle \dots \rangle$ denotes a time-average.

We start by considering systems that are driven by fields of considerable strength ($B_0^* = 10$) with frequencies that admit layer formation [cf. Fig. 7.5]. Results for the distribution f at three such frequencies ω_0^* are given in Fig. 7.9. For each value of ω_0^* one observes a single, pronounced peak, reflecting a synchronized state, in which the particles follow the field at constant phase difference. Note that the larger ω_0^* , the larger the phase difference between the particles and the field. This is not too surprising since an increase in the driving frequency implies an increase in the rotational friction due to the (implicit) solvent and the presence of neighboring particles. Further note that even though Eq. (7.10) contains a time-average, the phase distributions of these layered systems are essentially independent of time.

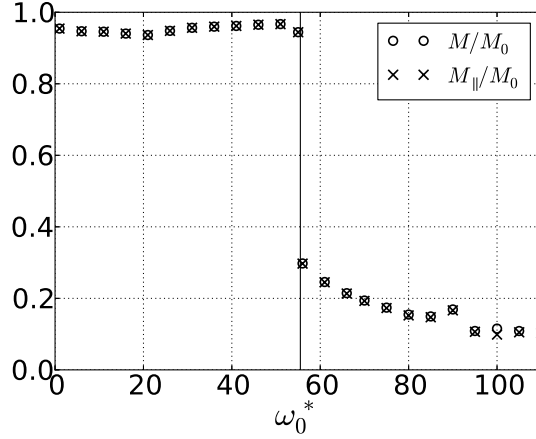


Figure 7.7.: Absolute value of the (in-plane) magnetization (M_{\parallel}) M normalized with respect to its saturation value over driving frequencies at $B_0^* = 10$. The vertical line indicates where layering breaks down.

To investigate the degree to which the particles actually rotate in the plane of the field, we also consider the distribution of the z -components of the angular frequencies

$$g(\omega_z^*) = \frac{1}{N\Delta\omega} \left\langle \sum_{i=1}^N \Theta(\omega_{i,z}^* - n\Delta\omega) - \Theta(\omega_{i,z}^* - (n+1)\Delta\omega) \right\rangle.$$

In an ideal situation, in which the dipoles rotate perfectly with the field, the distribution g would have a single, sharp peak at $\omega_z^* = \omega_0^*$. Simulation results for g in the true many-particle system are shown in Fig. 7.10, where we have picked out the states already considered in Fig. 7.9. As expected in the layered regime, the functions g are characterized by one central peak around $\omega_z^* \approx \omega_0^*$. However, we also see that there is a significant broadness in the distribution (as there is in the corresponding peaks of f).

Finally, above a certain frequency, the layers disappear. This is reflected in the emergence of a double-peaked structure in the distribution of the phase differences, as illustrated in Fig. 7.11(a). Moreover, we found that the non-averaged distribution of the phase differences is not independent of the time anymore. However, since we could not identify any systematic time-dependence in this regime, we restrict ourselves to considering the averaged distribution. The first peak in f at $\phi \approx \pi/4$ is due to particles that can still temporarily follow the field, whereas particles that are not able to do so anymore cause the structure of the rest of the distribution. The breakdown of layering is also visible in the distribution g . Contrary to what is seen in a layered system, the angular frequencies of the majority of the particles are distributed around $\omega_z^* \approx 0$ as shown in Fig. 7.11(b). The much smaller peak at approximately the frequency of the external drive shows that only a small fraction of the particles follow the field at any given time. This fraction is further decreased as the frequency ω_0^* of the driving field increases. Typical distributions f and g at values of ω_0^* outside the layered regime are shown in Figs. 7.12(a) and (b), respectively. Note that the roughly symmetric distribution of ω_z^* around approximately zero in Fig. 7.12(b) indicates that the particles are as likely to rotate in the direction of the field as they are to rotate into the opposite direction.

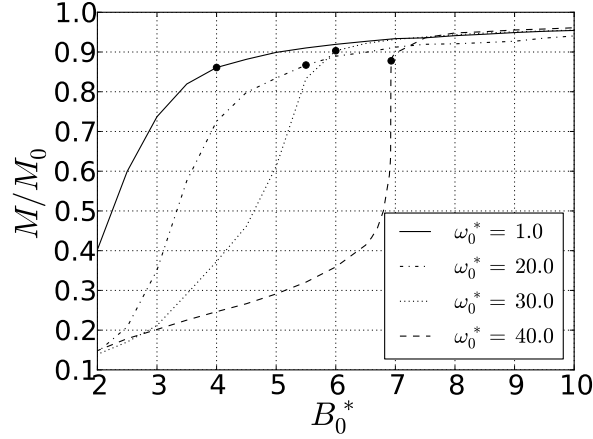


Figure 7.8.: Absolute value of the magnetization normalized with respect to its saturation value over field strength at different rotational frequencies. The dots indicate after which point the system is considered layered according to our order parameter.

Further note that at the large values of B_0^* considered in this section, the transition between states with the particles following the field at fixed phase difference and states where this is not true anymore happens in a very small range of frequencies.

7.6. Effective single-particle theory

To understand the character of the high-frequency boundary between layered and non-layered states in more detail, we now aim to construct an effective theory that describes a single dipolar particle rotating in a viscous medium. A similar consideration has been suggested for optically torqued nanorods by Shelton et al. [45]. Clearly, such a single-particle approach cannot grant us direct insight into the formation of layers. However, it may help us to improve our understanding of the rotational dynamics isolated from many-particle effects. For simplicity, we assume that the rotational motion of the particle is restricted to the plane of the field and that it experiences rotational friction with friction constant γ . Then the rotational equation of motion is given by

$$I\ddot{\phi} + \gamma\dot{\phi} = \gamma\omega_0 - \mu B_0 \sin \phi, \quad (7.11)$$

where ϕ is the phase difference between the direction of the external field and the orientation of the dipole. We first consider the simplified case of negligible moments of inertia, i.e., an overdamped situation. Then Eq. (7.11) reduces to the first order equation

$$\frac{d\phi}{d\tau} = \frac{\omega_0}{\omega_c} - \sin \phi, \quad (7.12)$$

where $\omega_c = \mu B_0 / \gamma$ and $\tau = \omega_c t$. This nonlinear differential equation appears in various contexts such as the description of overdamped pendula, superconducting Josephson junctions, and the synchronized emission of light by fireflies [45, 132]. For $0 \leq \omega_0 < \omega_c$ it has two fixed points characterized by $\dot{\phi} = 0$ (i.e., constant phase difference): One solution is a global attractor with $\phi = \arcsin(\omega_0/\omega_c)$, and the other one is unstable with $\phi = \pi - \arcsin(\omega_0/\omega_c)$. These two solutions

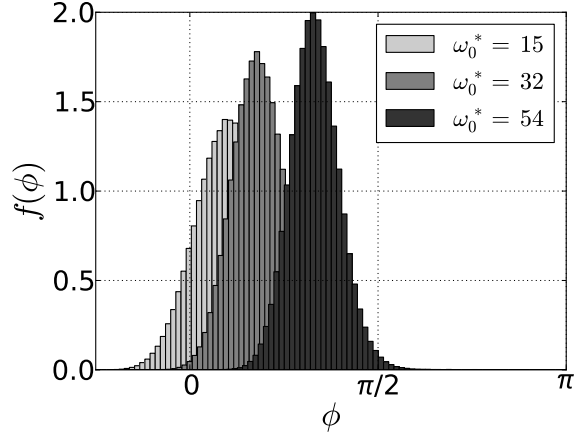


Figure 7.9.: Distribution of the phase differences at $B_0^* = 10$ and three frequencies ω_0^* with $\Delta\phi = \pi/48$. The systems are in layered states [see Fig. 7.5].

correspond to the phase differences at which the torque due to friction equals the torque that is due to the field. At $\omega_0 = \omega_c$, i.e., at $\phi = \pi/2$, the two solutions form a saddle-node bifurcation and there are no fixed points for $\omega_0 > \omega_c$. At these high frequencies, the maximal torque that can be exerted by the field is insufficient to balance the frictional torque. The solution emerging after the bifurcation is a limit cycle with $\phi > 0$.

To which extent does the single-particle approach describe the true many-particle system of our BD simulations? In Fig. 7.13(a), the frequencies ω_c [with $\gamma \equiv \xi_R$, see Eq. (4.27)] are plotted into the $\omega_0^* - B_0^*$ -state diagram (Fig. 7.5). At large frequencies ω_0^* and field strengths B_0^* , the straight line representing ω_c has a slope similar to that of the boundary of the layered regime. This supports the idea that it is the (rotational) friction which eventually yields a breakdown of the layering by preventing the particles from performing a synchronized rotation with the field.

A further observation from Fig. 7.13(a) is that the true boundary frequencies (at given B_0^*) are somewhat smaller than ω_c . One seemingly obvious reason for these deviations is that the effective theory neglects all the many-particle effects. Moreover, it does not take the Brownian random contributions into account that mimic the solvent “kicks” in Eq. (4.27). Both these factors could introduce perturbations of the effective field that acts on a particle. Thereby the synchronized state could be destabilized already at frequencies $\omega < \omega_c$. However, as it turns out, the more significant reason for the premature stop of layering is that the BD equations of motion involve (rotational) inertial terms, which are neglected in our single-particle approach.

To check this point, we have performed additional BD simulations with a lower moment of inertia ($I^* = 0.01$). The resulting frequencies characterizing the boundary of the layered state are shown in Fig. 7.13(b) along with the original result ($I^* = 0.025$) and the line ω_c . Clearly, decreasing the moment of inertia moves the true boundary substantially closer to the single-particle result.

Finally, we note that the influence of the inertial (rotational) term can also be captured within our effective single-particle theory. For $I \neq 0$, Eq. (7.11) can be written as

$$\frac{d^2\phi}{d\tau'^2} + \nu \frac{d\phi}{d\tau'} = \frac{\omega_0}{\omega_c} - \sin\phi \quad (7.13)$$

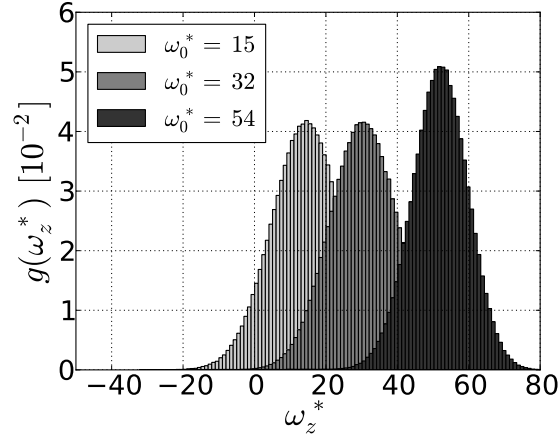


Figure 7.10.: Distributions of the z -component of the angular frequencies. Parameters are as in Fig. 7.9. The interval $\Delta\omega$ is set to 1.

with $\nu = \gamma/\sqrt{\mu B_0 I}$ and $\tau' = \sqrt{\mu B_0/I}t$. Similar to (7.11), this differential equation has a bifurcation at ω_c [132], which means that the location of the line ω_c in Fig. 7.13(a) remains unchanged [132]. As before, the only stable solution at driving frequencies that are larger than ω_c is a limit cycle. But additionally, for sufficiently small ν , it has a second bifurcation for some ω' with $\omega' < \omega_c$ as shown by Argentina et al. while investigating the transition between annihilation and preservation of colliding waves [133]. This second bifurcation introduces a regime in which the limit cycle can coexist with the stable rotation. Fig. 7.13 seems to indicate that this situation does indeed occur in the system: Some of particles in the system follow the field while the others perform another kind of rotational motion. However, from the perspective of a many-particle system, one may speculate it to be more likely that the presence of the second solution perturbs the rotation with constant phase difference (i.e., $\dot{\phi} = 0$).

7.7. A density functional approach to layering in a perfectly synchronized system

We now consider systems at relatively low driving frequencies ($\omega_0^* \lesssim 30$), where, for sufficiently large field strengths B_0^* , the dipole vectors can follow the field in a perfectly synchronized fashion (see the discussion in the preceding section). According to our “phase” diagram in Fig. 7.5, the field strength required to induce such synchronous and, at the same time, layered states, is about $B_0^* \approx 4 - 6$ for $\omega_0^* \lesssim 30$. The corresponding dipole-field coupling parameter $\mu B_0/k_B T = \mu^* B_0^*/T^* \approx 12$ is significantly larger than the dipole-dipole coupling parameter ($\lambda \approx 6.7$). Nevertheless, as seen in Figs. 7.4(a) and (b) as well as in Fig. 7.8, increasing B_0^* from zero at low driving frequencies yields a rather slow increase of the order parameter ψ and the magnetization amplitude.

Given the apparent interconnectedness between the rotational dynamics of the individual dipoles and the layering of the particles, we ask in the present section whether synchronization leads automatically to layering. Indeed, even in a perfectly rotating system, one would expect that the spatial symmetry-breaking associated with layering yields a decrease of translational

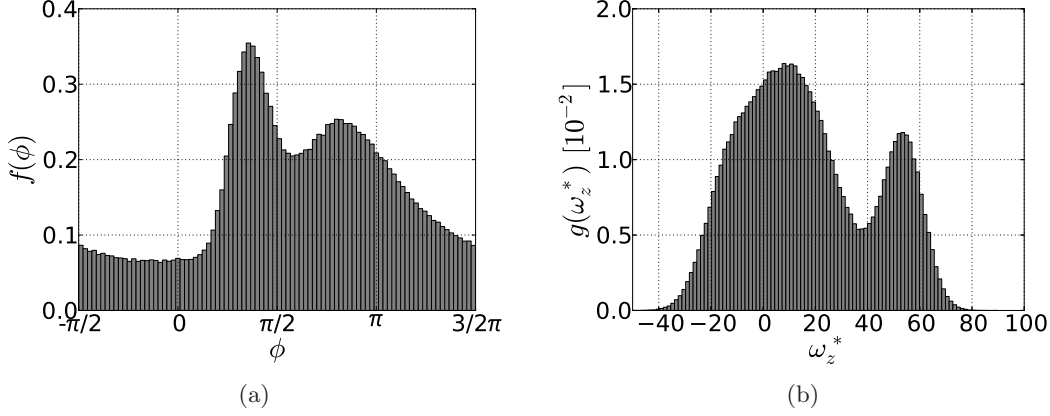


Figure 7.11.: (a) Distribution of the phase differences of the system at $B_0^* = 10$ and $\omega_0^* = 55.8$, i.e., just outside of the region of layer formation. The resolution is $\Delta\phi = \pi/40$. (b) Distribution of ω_z^* for a system at $B_0^* = 10$ and $\omega_0^* = 55.8$ with $\Delta\omega = 1$.

entropy and thus may be unfavorable.

To investigate this question we employ equilibrium DFT [see Sec. 6.2] for a system in which the dipole rotations are perfectly synchronized. Under such conditions the particles effectively interact via the time-averaged (inverted) dipolar potential given in Eq. (7.5). By using this potential, the problem thus reduces to searching for an equilibrium phase transition in a system with effectively static interactions.

Our density functional approach is based on the perturbation expansion of the Helmholtz free energy given in Eq. (6.5). We employ the RPA [cf. Sec. 6.2.3] to calculate the direct correlation function. Assuming a HS interaction [cf. Sec. 3.5] in addition to the inverse dipolar potential U^{ID} [Eq. (7.5)], the RPA amounts to setting

$$c(\mathbf{r}) = \begin{cases} c^{\text{PY}}(r), & r \leq \sigma \\ -\beta U^{\text{ID}}(\mathbf{r}), & r > \sigma, \end{cases} \quad (7.14)$$

where c^{PY} denotes the Percus-Yevick direct correlation function for hard spheres [cf. Eq. (6.23)]. To check the accuracy of the RPA in our system, we have also calculated $c(\mathbf{r})$ numerically by solving MSA integral equations [cf. Sec. 6.2.3]. However, the changes in the free energies were found to be marginal.

As a simple ansatz for the density profile in the layered state, we use

$$\rho(\mathbf{r}) = \rho(z) = \rho_0 + \tilde{\rho} \cos(kz). \quad (7.15)$$

Inserting this ansatz into Eq. (6.5), we find

$$\frac{\Delta\mathcal{F}}{A} = \frac{1}{\beta} \int_0^{\lambda_L} dz \rho(z) \log \left(\frac{\rho(z)}{\rho_0} \right) - \lambda_L \frac{\tilde{\rho}^2}{4\beta} \tilde{c}(k), \quad (7.16)$$

where $\Delta\mathcal{F}$ is the free energy of the volume $A \cdot \lambda_L$, A is an area in the $x - y$ -direction and $\lambda_L = 2\pi/k$. Further, \tilde{c} is the Fourier transform of c and $\tilde{c}(k) \equiv \tilde{c}(k\mathbf{e}_z)$. In the RPA, we have

$$\tilde{c}(k) = 4\pi \left[\int_0^\sigma dr r^2 j_0(kr) c^{\text{PY}}(r) + \mu^2 \beta \frac{j_1(k\sigma)}{k\sigma} \right], \quad (7.17)$$

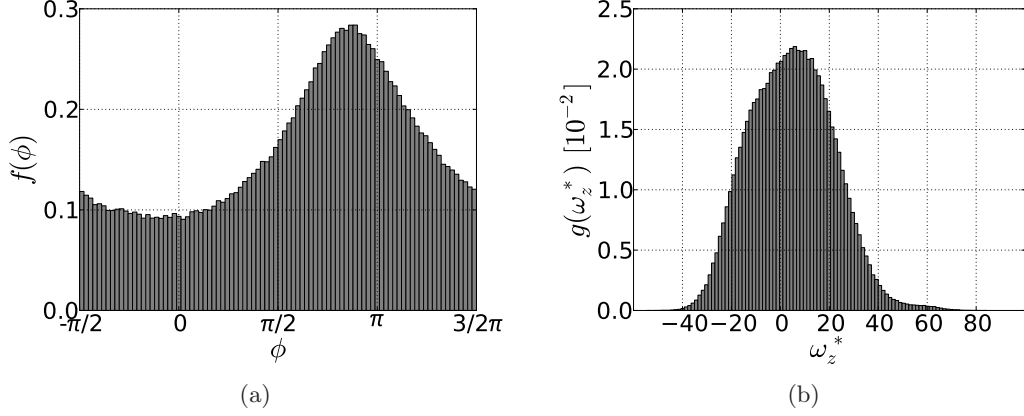


Figure 7.12.: (a) Distribution of phase differences of the system at $B_0^* = 10$ and $\omega_0^* = 60$. The system is unlayered. (a) Distribution of ω_z^* of the system at $B_0^* = 10$ and $\omega_0^* = 60$. The system is unlayered.

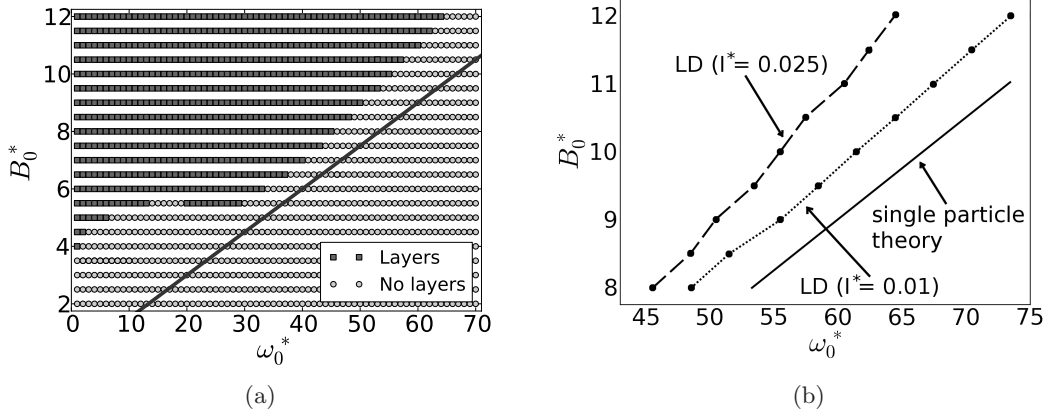


Figure 7.13.: (a) The solid line shows the critical frequencies $\omega_c = \mu B_0 / \xi_R$ that are predicted by the single-particle theory in the BD frequency-field strength diagram [see Fig. 7.5]. (b) Influence of the moment of inertia on the end of layer formation (dashed line: $I^* = 0.025$, dotted line: $I^* = 0.01$, dots: actual simulation results). The solid line indicates the frequencies ω_c^* .

where j_n are spherical Bessel functions of order n [106]. (For the treatment of the dipolar interactions in Eq. (7.17), see Ref. [134].) We now use Eq. (7.16) to search for a phase transition between the homogeneous and the layered state. In principle, this search requires a minimization of $\Delta\mathcal{F}/A$ with respect to both the parameters $\tilde{\rho}$ and k that characterize the inhomogeneity of the system [see Eq. (7.15)]. It turns out, however, that $\Delta\mathcal{F}/A$ becomes minimal with respect to k for $k \rightarrow 0$, which corresponds to an infinite distance between the layers. Clearly, this is not compatible with the implicit assumption of a finite wavelength. Therefore we have fixed the parameter $k = 2\pi/\lambda_L$ to physically reasonable values, i.e., to values suggested by our LD simulations. At $\rho_0^* = 0.1$, we find an average layer distance of approximately 7.2σ (see below). This leaves the

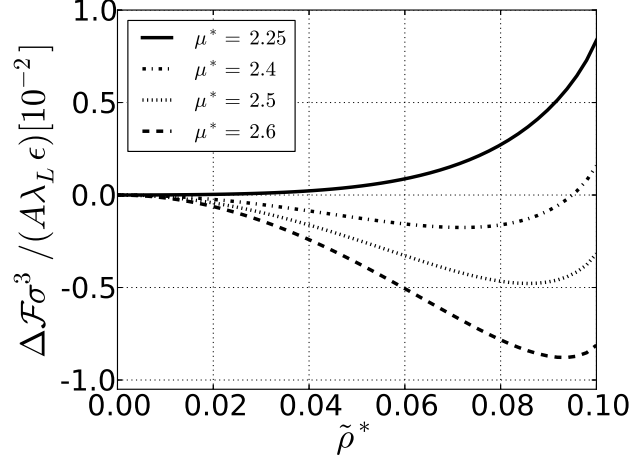


Figure 7.14.: Free energy difference between a layered and a homogeneous state as a function of the coefficient $\tilde{\rho}$ [see Eq. (7.15)] at different values of the parameter μ^* . The case $\tilde{\rho} = 0$ corresponds to the homogeneous solution. The overall density is set to $\rho_0^* = 0.1$.

coefficient $\tilde{\rho}$ as the only minimization parameter. Results for the function $\Delta\mathcal{F}(\tilde{\rho})/(A\lambda_L)$ with fixed distance $\lambda_L = 7.2\sigma$ between the layers at various values of the parameter μ^* are plotted in Fig. 7.14.

The different curves in Fig. 7.14 reveal a behavior typical of a second-order phase transition. For $\mu^* \lesssim 2.27$, the free energy has only one minimum at $\tilde{\rho} = 0$ corresponding to an homogeneous state. This changes at $\mu_c^* \approx 2.27$: For larger values of μ^* , the solution at $\tilde{\rho} = 0$ represents a maximum, and the only minimum occurs for $\tilde{\rho} > 0$. The corresponding negative values of $\Delta\mathcal{F}/A$ indicate that it is indeed the layered state which is now globally stable.

We have repeated the DFT calculations for a number of densities in the range $0.01 \leq \rho_0^* \leq 0.4$. To find reasonable values for the corresponding wavelengths λ_L in the layered state, we ran LD simulations at fixed dipole moment $\mu^* = 3.4$, frequency $\omega_0^* = 8$, and field strength $B_0^* = 50$. With this choice of the parameters, the particles are almost perfectly aligned, justifying the key assumption of our DFT approach. Fitting the resulting distances as functions of ρ_0 , we found the approximate relation $d/\sigma \approx 1.05\rho_0^{*-0.84}$, which was then used as an input in the DFT (i.e., $\lambda_L = d$).

The resulting phase diagram in the $\rho_0^* - \mu^*$ -plane is plotted in Fig. 7.15. It is seen that the DFT predicts a layering transition for all but the smallest densities ($\rho_0^* \gtrsim 0.01$) in the shown parameter range, with the actual values of μ_c^* varying substantially with ρ_0^* . Indeed, the lowest threshold is found at $\rho_0^* \approx 0.2$. Also shown in Fig. 7.15 are LD results for the appearance of layers in nearly perfectly synchronized systems ($\omega_0^* = 8$, $B_0^* = 50$) at various values of μ^* . As in Sec. 7.3, the presence of layers was detected on the basis of the order parameter defined in Eq. (7.6), yet with a slightly different definition of the cutoff radius entering the order parameter ($r_0 = d$). Comparing LD and DFT, it is seen that the DFT predicts the true phase boundary in perfectly synchronized systems in a qualitatively correct manner (including the strong increase of μ_c^* upon $\rho_0^* \rightarrow 0$). Moreover, the DFT results are also quite reasonable from a quantitative point of view.

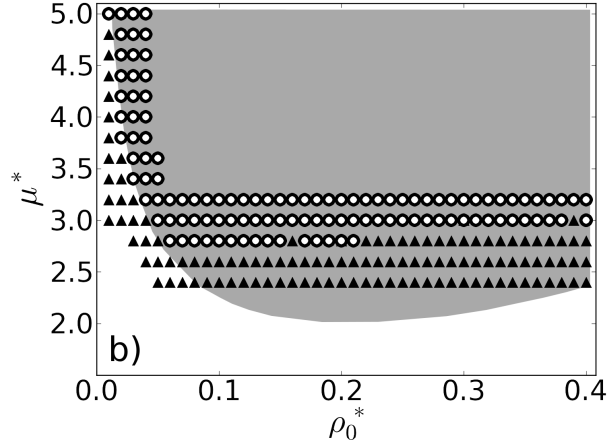


Figure 7.15.: Equilibrium phase diagram of a perfectly synchronized system. The gray area indicates the stability range of the layered state according to our DFT calculations. Also shown are LD results (at $\omega_0^* = 8$, $B_0^* = 50$) with the open circles (solid triangles) representing layered (non-layered) states.

From a physical perspective, clearly the most important conclusion is that even in a perfectly synchronized system, a sufficient decrease of interaction energy (i.e., a sufficiently large dipolar coupling strength) stemming from the time-averaged dipolar potential is required to overcome the entropy cost due to layering.

Finally, we briefly discuss our DFT results in the light of a recent Monte Carlo study by Smalenburg and Dijkstra [135], who obtained full equilibrium phase diagrams of systems interacting with inverted dipolar interactions. To model the short-range part of the interaction, Smalenburg and Dijkstra used either just hard spheres or hard spheres with an additional Yukawa repulsion [135]. In the first case, layer-like structures were only observed in the gas-liquid coexistence region. On the contrary, the Yukawa system exhibits a stable layered phase with fluid-like in-plane structure. Comparing these latter results to our DFT predictions, we find that the predicted strength of the inverted dipolar interactions required for layer formation is indeed comparable. On the other hand, we find the onset of layer formation at much lower densities. Apart from the obvious approximations in our theory, we also attribute these deviations to the fact that the repulsive Yukawa interaction used in Ref. [135] is much stronger than our soft sphere one.

7.8. Influence of hydrodynamic interactions

In this section, we want to look into the influence of HIs on the layer formation and the synchronization behavior of the particles. In particular, we are interested in the stability of the layer formation phenomenon under the inclusion of HIs.

To investigate the influence of the presence of a solvent, we use BD simulations with HIs as described in Sec. 4.4. We consider the diffusion tensor up to third order in the inverse particle distance and make use of an Ewald summation technique for the HIs [see Appendix E]. The number of particles in these simulations is chosen to be 256.

Let us begin by considering the magnetization at different driving frequencies of identical

systems ($\mu^* = 3.5$, $B_0^* = 10$) with and without HIs included. Fig. 7.16 shows that the normalized magnetization starts with a value close to one in both cases. Recalling Secs. 7.4 and 7.5, this indicates the presence of a very synchronized state. The value of the magnetization drops as the frequency of the field is increased. The addition of the HIs, however, has hardly any influence on this behavior. The deviations from the not hydrodynamically interacting system are minimal.

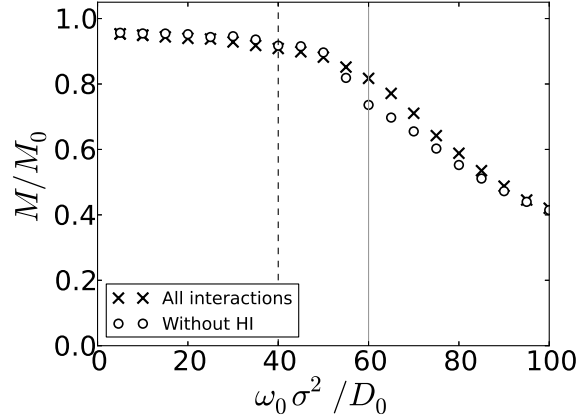


Figure 7.16.: Magnetization of a system at $\mu^* = 3.5$ and $B_0^* = 10$ with and without the presence of HIs. The vertical lines indicate where layer formation stops with (dashed) and without (solid) the solvent-mediated interaction included.

The layer formation itself, on the other hand, is more strongly influenced: As illustrated in Fig. 7.16 by the vertical lines, the layers disappear at $\omega_0 \sigma^2 / D_0^T \approx 40$ if HIs are taken into account, while a driving frequency of $\omega_0 \sigma^2 / D_0^T \approx 60$ is necessary for the same to occur in the system without solvent-mediated interactions.

The effective potential (7.5), which is responsible for the layer formation, was derived under the assumption that the translational motion of the particles during one rotational period of the field is negligible. However, a consequence of the HIs in the considered system is very likely an increase in translational motion of the particles stemming from the flow fields created by the rotationally driven particles [due to the TR coupling, cf. Sec. 8.5.2]. Hence, we speculate that the earlier breakdown in the hydrodynamically interacting system can be explained by the effective particle interaction describing the actual interaction less accurately than in the not hydrodynamically interacting system. In particular, the larger the driving frequency, the more motion is induced in the system. For more details, see the hydrodynamic results presented in Sec. 8.5.2 for two-dimensional systems.

Let us now compare Figs. 7.7 and 7.16 with each other. The former shows the behavior of the magnetization in our LD simulations, while the latter shows its behavior in BD simulations with and without HIs included. Compared to the BD results, the magnetization drops considerably faster in the LD case once the particles cannot follow the field anymore. Clearly, this is due to the retained inertial terms in the LD simulations. In fact, on decreasing the moment of inertia in our LD simulations, we find a behavior of the magnetization as shown in Fig. 7.16.

The slow falloff of the magnetization in BD can be understood by considering Fig. 7.17. Here, the derivative of the phase difference with respect to time over the phase difference is plotted for systems at $B_0^* = 90$ and $\omega_0 \sigma^2 / D_0^T = 90$. This is decidedly outside of the synchronized regime,

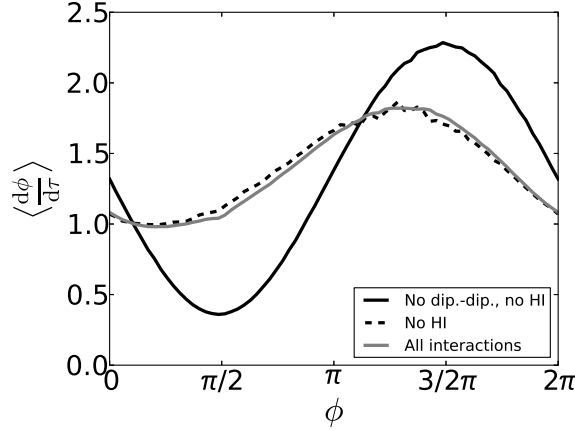


Figure 7.17.: Derivative of the phase difference with respect to time over the phase difference for systems with different interactions included. Shown are systems without HI and dipole-dipole interactions, without HI, and with all interactions included. The systems are at $B_0^* = 90$, $\omega_0\sigma^2/D_0^T = 90$, and $\mu^* = 3$. Note that the random (rotational) Brownian contributions are neglected here: Not excluding them causes the results to be highly noisy even after considerable simulation times.

since $\omega_c\sigma^2/D_0^T \approx 67$ [cf. Sec. 7.6].¹ The behavior for three different systems is shown: A system of particles that do not interact with each other, a system of particles interacting only via DSS interactions, and a system additionally interacting via HIs. The first system behaves as predicted by Eq. (7.12), i.e., $\langle d\phi/d\tau \rangle$ is minimal at $\phi = \pi/2$ and maximal at $3/2\pi$. The behavior of the system that includes dipole-dipole interactions retains these two qualitative features: There exists a minimum as well as a maximum in $\langle d\phi/d\tau \rangle$. However, the extrema are less pronounced and shifted to smaller phase differences. The system that additionally interacts hydrodynamically behaves essentially identical to the dipole-dipole system, supporting the magnetization behavior shown in Fig. 7.16.

The explanation for the slow decrease in the magnetization seen in Fig. 7.16 can be found in the existence of the minimum in the derivatives of the phase differences shown in Fig. 7.17: At the minimum the phase difference of the particles changes the slowest resulting in a large number of particles being aligned with each other. This implies that the magnetization has a high value despite the lack of synchronization of the particles with the field. The closer the driving frequency is to the critical frequency, the lower the value of the minimum in $\langle d\phi/d\tau \rangle$ and the higher the magnetization of the system.

In conclusion, the results of this section show that the layer formation phenomenon is stable under the inclusion of HIs. Layers still form and the synchronization process seems to be unaffected at the considered thermodynamic and field parameters. However, the breakdown of layer formation occurs at slightly smaller frequencies if HIs are present.

¹Note that $\langle d\phi/d\tau \rangle(\phi) \neq 0$ for all ϕ in Fig. 7.17. From this fact we can immediately infer that there is no synchronization in the system.

7.9. The role of the simulation method

As shown in the previous sections, the physical reason for the layer formation is the synchronized rotation of the dipole moments with the field, and, hence, with one another. Due to the inherent nonequilibrium character of this phenomenon, it is an important question how the dynamic behavior would change with a different choice of the equations of motion. This is precisely the goal of the present section, where we compare the layering and synchronization behavior observed in LD with that emerging in corresponding MD simulations. To highlight the differences we restrict ourself in the present section to the investigation of some particularly interesting state points.

Here, we use MD simulations in the isokinetic ensemble and LD simulations to investigate the system. The details of the former technique are described in Sec. 4.1. Note that we use a Gaussian isokinetic thermostat [see Sec. 4.1.2] in our MD simulations, which is often used in nonequilibrium simulations [37, 136]. In contrast, in our LD simulations, the temperature is maintained by the balance of frictional and random forces (and torques).

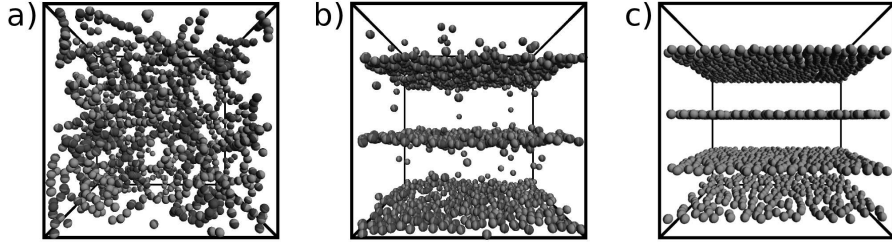


Figure 7.18.: (a) Snapshot of the system in zero field (LD). (b) Snapshot from a LD simulation of a system in a layered state. The strength and frequency of the field are $B_0^* = 12$ and $\omega_0^* = 15$, respectively. (c) Snapshot from a MD simulation of a system in a layered state ($B_0^* = 12, \omega_0^* = 10$).

To start with, Fig. 7.19 shows the behavior of the order parameter ψ [see Eq. (7.6)] at constant driving frequency $\omega_0^* = 5$ of the field in MD and LD. In both simulation methods, the order parameter increases with increasing field strength. As shown in Secs. 7.3-7.5, layer formation relies on the synchronization of the particles with the field. Hence, the rise of the order parameters is explained by the increasing level of alignment, i.e., synchronization, of the particles with the field. Even though ψ behaves quite similarly in MD and LD at fixed ω_0^* , there are some notable differences. First, ψ rises more steeply in the MD simulations than in the LD ones, implying that layers emerge at smaller field strengths in MD than in LD. According to Fig. 7.19, the system is layered for $B_0^* \geq 3.5$ in MD while a field strength of $B_0^* = 5$ is necessary in LD. A further difference is that the order parameter in the MD simulations actually reaches a value of 1, showing that the system ends up in a perfectly layered state. Irrespective of field strength and frequency, this never happens in LD simulations. Figs. 7.18(b) and (c) illustrate this point: The snapshot from the MD simulations [Fig. 7.18(b)] shows a system with sharply defined layers, while the LD snapshot shows less well defined ones. These differences can be attributed to the non-conservative, random and frictional forces, which appear in the LD equations of motion but not in the MD ones. In particular, the random forces broaden the layers thereby preventing them from being as well defined as in MD simulations, which keeps the order parameter at lower values. The last difference, which is also a manifestation of the random contributions, are

the fluctuations in the function ψ that are present in LD but not in MD. We interpret these fluctuations as a consequence of the fluctuating forces. These perturb the layer structures and particle distributions in between the layers, which results in slightly varying order parameters.

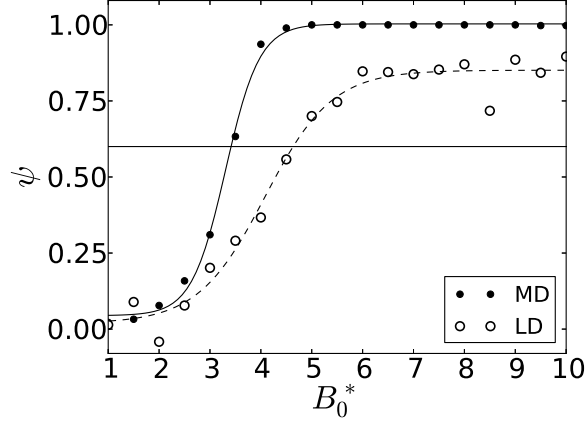


Figure 7.19.: Behavior of the order parameter ψ at constant driving frequency $\omega_0^* = 5$ for MD and LD. The horizontal line indicates where $\psi = 0.6$. Systems with $\psi \geq 0.6$ are considered as layered.

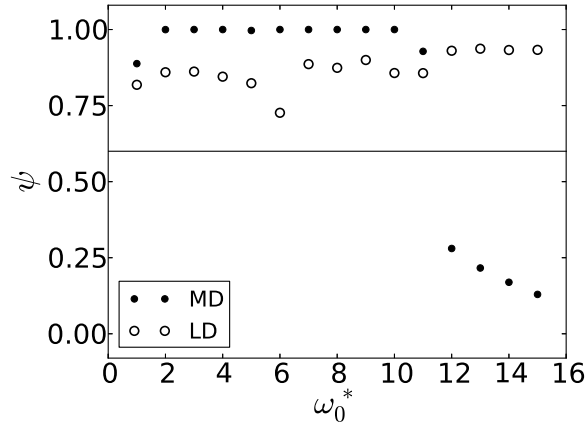


Figure 7.20.: Behavior of the order parameter ψ at constant field strength $B_0^* = 10$ for MD and LD simulations. The horizontal line indicates where $\psi = 0.6$.

In a next step, we investigate the role of the driving frequency for the layer formation behavior in MD and LD. To this end, we choose a field strength that is sufficiently high to guarantee layer formation and synchronization with the field at lower driving frequencies. Fig. 7.20 shows the order parameter ψ at $B_0^* = 10$ as a function of ω_0^* . The order parameter assumes high values for small frequencies, reflecting the layered nature of the system in both MD and LD. However, ψ drops considerably at $\omega_0^* = 12$ in MD, leaving the system in a non-layered state. This behavior is not mirrored in the LD simulations, where ψ stays above the value that separates the layered

from the unlayered regime. To understand the different dynamic behavior, we note that the two simulation methods differ in the way the system is thermostatted. In MD the isokinetic thermostat ensures that $T_{\text{rot}}^* = 1.35$ [see Eq. (4.10)] is satisfied at all times. This means that if all the particles rotate with the same velocity, the maximal rotational frequency admitted by the thermostat is roughly $\omega_0^* \approx 10.4$. Hence, we would expect a drop in the degree of synchronization of the particles beyond this value of the driving frequency. To look into this, we again turn to Fig. 7.21, which depicts the time-averaged absolute value of the magnetization normalized with respect to its saturation value [cf. Eq. (7.9)]. Fig. 7.21 shows that M drops significantly between $\omega_0^* = 10$ and 11 in MD, confirming that the degree of synchronization does indeed decrease drastically when the driving frequency exceeds $\omega_0^* \approx 10.4$. Consequently, beginning at this value of ω_0^* , an increasing number of particles is not able to follow the field anymore, which ultimately results in the breakdown of layer formation at $\omega_0^* \approx 12$ [cf. Fig. 7.20]. Thus, the strictly imposed temperature in MD prevents the formation of layers after a rotational frequency that typically is considerably smaller than in LD. Indeed, the breakdown of synchronization in LD occurs only at $\omega_0^* \approx 56$ (for $B_0^* = 10$).

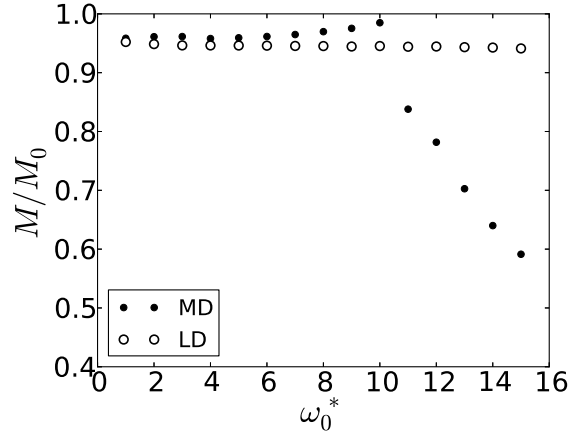


Figure 7.21.: Time-average of the absolute value of the magnetization M normalized with respect to its saturation value $M_0 = N\mu$.

7.10. Conclusions

In this chapter we have combined LD, MD, and BD computer simulations, an effective single-particle theory, and an (equilibrium) density functional approach to explore the dynamic behavior of systems of dipolar particles in planar rotating fields.

One main result from our LD simulations is a nonequilibrium “phase” diagram identifying the domain of layered states in the ω_0 - B_0 plane (at constant particle density and dipolar coupling strength). At low driving frequencies, the change from unlayered to layered (and fully synchronized) structures occurring upon increase of B_0 is related to a quasi-equilibrium phase transition, i.e., a many-particle phenomenon. The transition is induced by the competition between the time-averaged, inverted dipolar interactions favoring in-plane configurations and the loss of translational entropy accompanying the one-dimensional translational order. While this competition also occurs for systems of induced magnetic particles, the additional complication

in the present system of permanent dipoles is that the field first needs to overcome the dipolar fluctuations. Though we have neglected this issue in our DFT approach, we would expect that the fluctuations just shift the transition predicted by the DFT towards larger field strengths.

Completely different behavior is found at high frequencies and field strengths. Under these conditions, the picture of synchronously rotating dipoles (with constant phase difference relative to the field) breaks down. Instead, one observes a mixture of rotating and counter-rotating or resting particles, as our analysis of various angle distributions reveals. The desynchronization induces, at the same time, a breakdown of the translational, layered structure. Despite this complex many-particle behavior, we have shown that the boundary can be well described in terms of the critical frequency $\omega_c(B_0)$ that arises from a bifurcation in an effective single-particle approach for the rotational motion in a viscous medium. This indicates that the appearance of the high-frequency boundary is essentially a friction-induced effect.

A similar frequency-induced desynchronization effect has recently been discussed by Härtel et al. [129], who investigated a system of interacting elongated particles in a rotating electric field via dynamic DFT. Assuming a constant number density, the important dynamic variable within the density functional approach is the orientational distribution as function of time. At low and very high frequencies, the distribution behaves similar to our distribution f in that there is either a single peak (reflecting synchronized motion with a constant phase difference) or no peak at all. In the transition regime, however, Härtel et al. detected various new dynamic states characterized by time-dependent oscillations and splitting of the peak in the distribution as well as an overtaking by the driving field. We did not observe such states, not even when looking at the time-dependence of our orientational distributions (or the magnetization). It remains to be investigated whether these qualitative differences in the rotational motion of anisotropic many-particles systems are just due to differences in the specific model system, or due to the fact that our results are based on a microscopic approach rather than on the density field approach used in Ref. [129]. Indeed, the relation between the microscopic and mesoscopic dynamics in driven systems is an issue also discussed in other, related contexts, such as the shear-induced dynamics of nanorods [137].

We should also stress the differences between the behavior of our system, where the particles carry permanent dipole moments, and systems of induced dipoles such as suspensions of paramagnetic particles. In the latter case, the issue of synchronization and, more generally, the rotational dynamics of individual particles is clearly irrelevant, since the induced dipole moments are by definition parallel to the field. Note, however, that our density functional calculations presented in Sec. 7.7, which foot on the assumption of perfect synchronization, can be applied to systems of induced dipoles without any changes.

In this chapter, we have also investigated the influence of solvent-mediated interactions. Most importantly, we have shown layer formation to be stable under the inclusion of HIs. However, these interactions shift the breakdown of layer formation to lower driving frequencies of the field. On the other hand, the rotational behavior of the particles seems to hardly be affected (at the considered thermodynamic parameters).

Further, we have compared layer formation in MD and LD simulations with each other. Due to the absence of random forces, the minimal field strength required for layer formation is smaller in MD simulations than in corresponding LD simulations. Apart from this difference, layer formation at constant angular frequency progresses similarly for both simulation methods. At constant driving frequency of the field, however, qualitative differences appear. In MD, the synchronization of the particles with the field, which is imperative for the formation of layers, breaks down at much lower frequencies than in comparable LD simulations. In LD the breakdown

seems to basically be a friction-induced effect. In MD, on the other hand, the thermostat, i.e., the constant temperature, prevents the particles from rotating with adequate speed after a certain driving frequency. In contrast to LD, this frequency should be independent of the strength of the applied field. In this regime, synchronization of the particles with the field is lost. Hence, our analysis shows that the method of thermostatization significantly influences the dynamic behavior of the particles, and, in consequence, the field-induced formation of layers.

Finally, it is worth to briefly comment on the relevance of our dimensionless model parameters in the context of real systems. The equilibrium parameters considered here (density $\rho^* = 0.1$, dipolar coupling strength $\lambda \approx 6.7$) correspond to those of a strongly coupled ferrofluid exhibiting chain formation [31]. Regarding the driving field, however, most of our dimensionless frequencies ω_0^* are probably beyond the currently accessible range. In many experiments involving rotating fields, the size of the (typically paramagnetic) particles considered is about $1 \mu\text{m}$ [19, 40]. A driving frequency of $\omega_0^* = 10$ (which is well within the layered domain) then corresponds to an actual frequency of about 10 kHz if we assume room temperature ($T = 293 \text{ K}$) and a mass density of 5 g/cm^3 . This is 1-2 orders of magnitudes larger than the frequencies used in the literature [19, 40]. Ferrocolloidal particles, which have permanent dipoles (such as the ones considered here), are often much smaller with sizes of about 10 nm. In that case, $\omega_0^* = 10$ corresponds to a driving frequency of about 1 GHz.

These considerations suggest that realistic driven systems will be fully synchronized and layered according to our “phase” diagram in Fig. 7.5. We note, however, that the actual location of the desynchronization line encountered upon increasing ω_0^* depends on the friction constant used in our LD simulations; i.e., increasing the friction constant shifts the line towards lower frequencies (consistent with the single-particle theory).

8. Nonequilibrium condensation and coarsening of field-driven dipolar colloids in two dimensions

So far, we have discussed the effects of rotating fields on dipolar particles in a three-dimensional geometry. Recently, it was shown by Weddemann and coworkers in an experimental study [27, 138] that a particularly interesting self-organization process occurs when (permanently) dipolar colloidal particles in a quasi-two-dimensional geometry are exposed to (in-plane) rotating fields. In this case, the external fields can be observed to induce the formation of two-dimensional clustered structures. Weddemann et al. were the first to describe this phenomenon for particles carrying a permanent dipole moment. However, particles with an induced dipole moment show a similar behavior [40, 139, 140].

As in Ch. 7, the clustering phenomenon is rooted in the synchronization of the particles with the field. In a two-dimensional geometry, the effective, time-averaged interaction between two particles in a synchronized system becomes isotropic and attractive causing the agglomeration of the particles. Clearly, in this system, the collective (rotational) dynamic behavior of the particles is (again) of crucial importance.

In this chapter, we want to provide a novel interpretation of the two-dimensional cluster formation process. Specifically, we show that this self-organization process is a consequence of an equilibrium phase transition between a vapor and a condensed phase. Moreover, the observed cluster formation corresponds to spinodal decomposition in the coexistence region of the phase transition. This process introduces an additional dynamic component into the system, since the cluster growth associated with spinodal decomposition is a dynamic many-particle effect in itself.

This chapter is organized as follows: After introducing the model and the different simulation techniques, we first discuss the full nonequilibrium “phase” diagram indicating the region of cluster formation in the domain of frequency and strength of the external field at constant equilibrium thermodynamic parameters. Then we present the principal point of this chapter: We show that the nonequilibrium cluster formation is essentially an equilibrium phase transition. To do this, we calculate an equilibrium phase diagram, in the construction of which an effective non-time-dependent interparticle interaction is used, and examine the growth of the characteristic domain size of the clusters. In a last step, we extensively investigate the influence of HIs on the formation, the dynamics, and the internal structure of the clusters. In our hydrodynamic simulations, we not only account for the translational hydrodynamic couplings, but for all the couplings between the translational and rotational motions of the particles. The chapter is then closed with a brief summary and conclusions.

The results presented in this chapter have to a large extent been published in Refs. [49, 141]. Further note that we briefly discuss a similar system in Appendix A. Instead of an in-plane field, we study the effects of an out-of-plane field in a quasi-two dimensional geometry.

8.1. Model and simulation methods

To model the (dipolar) colloidal particles in our simulations we use a DSS potential [Eq. (3.7)]. In these simulations, the particles are confined to a quasi-two-dimensional geometry. This means that the dipoles can rotate freely in all the spatial directions while their translational motion is restricted to the $x - y$ -plane. The external field rotates in this plane, i.e., it is given by Eq. (7.2).

As in Ch. 7, we use LD simulations to understand the dynamical properties of the system. We integrate the equations of motion (4.26) and (7.1) with a Leapfrog algorithm [Sec. 4.1.1] using a time step of $\Delta t^* = 0.0025$. The friction coefficients are chosen as in the previous chapter ($\xi_T^* = 13.5$ and $\xi_R^* = 0.45$) and we use either 4900 or 1225 particles in our simulations.

Further, to investigate the equilibrium phase behavior of the system [based on a time-averaged potential, see Eq. (7.5)], we use Monte Carlo (MC) simulations in the grand canonical ensemble.¹ In general, first-order phase transitions are plagued by a large free energy barrier separating both phases, making unbiased sampling very inefficient. In order to overcome the barrier we use an extension of a method proposed by Wang and Landau [142]. In the standard Wang-Landau method the entire density of states is sampled, which is infeasible in dipolar systems due to the computational cost. To account for this we fix the temperature and chemical potential in our simulations to limit the number of accessible states. Furthermore, we introduce an additional weight-function to the Metropolis MC sampling algorithm. This function is computed on the fly and adapted in such a way that it improves the sampling of states which have not been visited sufficiently often. This allows us to sample both phases efficiently despite them being separated by a free energy barrier. Details of the method applied to dipolar systems in two dimensions can be found in [143].

In the case of LD and MC simulations, we again deal with the long-range dipolar interactions by using the Ewald summation method [cf. Sec. 5]. However, in contrast to Ch. 7, we now use the Ewald sum for quasi-two-dimensional dipolar systems [see Sec. 5.3].

Finally, to investigate the influence of a solvent within our implicit model, we use BD simulations that include HIs between the particles. As shown in Sec. 4.4, these interactions are incorporated up to third order in the diffusion tensor for the translation-translation coupling, the rotation-rotation coupling, and the translation-rotation (and vice versa) coupling. The time evolution equations that are used can be found in Sec. 4.4. In these simulations, we consider $N = 324$ particles in a simulation box that is bounded by soft walls [cf. Sec. 4.4], i.e., we do not use periodic boundary conditions. Therefore, it is not necessary to use special techniques (e.g., Ewald sums) to treat the long-range dipole-dipole interactions. The forces and torques can be calculated directly via Eq. (3.9).

8.2. Synchronization and cluster formation

In this section, we present results from LD simulations, the goal being to determine the conditions (i.e., frequencies, field strengths) for which cluster formation occurs. We also introduce the equilibrium model resulting from a time-average of the interactions in the driven system. A snapshot of a quasi-two-dimensional system ($\rho\sigma^2 = 0.3$, $T^* = 1.0$) of strongly coupled dipolar particles ($\lambda = \mu^2/k_B T \sigma^3 = \mu^{*2}/T^* = 9$) at zero field is shown in Fig. 8.1(a). As is typical for such dipolar systems the particles align in a head-to-tail configuration, which, in a two-dimensional geometry, results in the formation of chains and rings [144].

¹Note that the Wang-Landau MC simulations were performed by Dr. Heiko Schmidle.

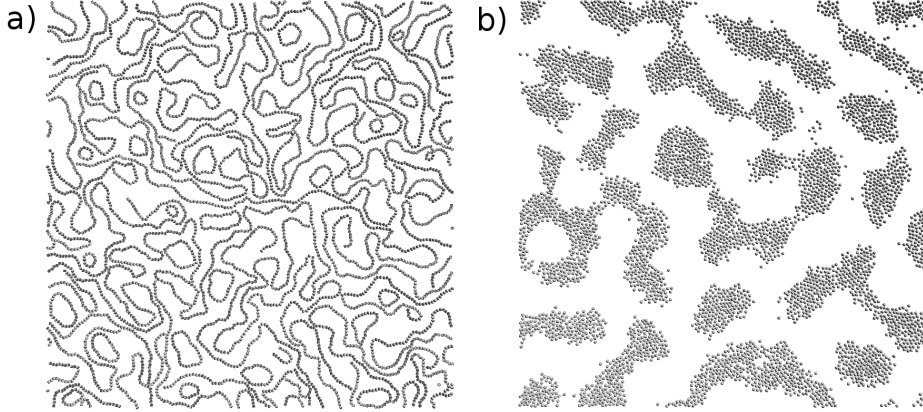


Figure 8.1.: Snapshots showing a system ($\rho\sigma^2 = 0.3$, $T^* = 1.0$) in (a) zero field and (b) exposed to a rotating field of strength $B_0^* = 50.0$ and frequency $\omega_0^* = 20$. Snapshot (b) was taken at time $t^* = 375$ after the start of the simulation. 4900 particles were used. Note that the configuration shown in (b) is not in equilibrium [cf. Sec. 8.3]

If we expose such a strongly coupled system to a rotating in-plane field [see Eq. (7.3)] of sufficient strength and frequency, we observe that the particles agglomerate into two-dimensional clusters. An example of this can be seen in Fig. 8.1(b). The observed clustering behavior already indicates that there are attractive interactions in the system, which play a crucial role. The origin of these interactions can be rationalized as in Ch. 7. Assume that the particles do not move in space and that they rotate synchronously with the field:

$$\boldsymbol{\mu}_i(t) = \boldsymbol{\mu}_j(t) = \mu[\mathbf{e}_x \cos(\omega_0 t + \delta) + \mathbf{e}_y \sin(\omega_0 t + \delta)] \quad (8.1)$$

Averaging the dipolar interaction potential between two particles over one rotational period of the field then yields the averaged potential

$$U^{\text{ID}}(\mathbf{r}_{ij}) = -\frac{\mu^2}{2r_{ij}^3}. \quad (8.2)$$

As in Sec. 7.3, the dipolar potential was averaged over one rotational period of the field. Note that the potential (8.2) corresponds to Eq. (7.5) with $\Theta_{ij} = \pi/2$, i.e., to the particles being in the same plane.

To systematically investigate the appearance of synchronization and clustering, we scanned a wide range of frequencies and field strengths in a system containing 1225 particles. We consider a system as clustered if the particles have on average more than 2.3 neighbors within a distance of 1.7σ from their center. The latter value was used, since it is slightly larger than the typical distance between neighboring particles in a clustered system at high frequencies of the field. This was found by looking at the first minimum of respective pair correlation functions. The fact that we require 2.3 neighbors on average ensures that two-dimensional aggregates are counted as clusters while chainlike structures are disregarded. Using larger values for the required number of neighbors results in a shift of the boundary between the synchronous region and the clustered region to higher frequencies. Responsible for this is the fact that the clusters become tighter with rising frequencies due to the effective interaction between the particles becoming more isotropic.

The results of this investigation of the space of the field parameters can be seen in Fig. 8.2. Depicted are three distinct regions, denoted “synchronous-not clustered”, “synchronous-clustered”, and “not synchronous-not clustered”. The first region is comprised of systems in which the particles rotate synchronously with the field but do not form clusters. Within this region, chains in the direction of the field can be observed at low frequencies while spatial inhomogeneities, i.e., very loose clusters, begin to appear at slightly larger frequencies. As also becomes apparent here, a minimal B_0 is required for the field to align the particles with itself.

In the second region, the synchronous rotation continues but is now accompanied by the formation of two-dimensional clusters. This indicates that the effective interparticle potential becomes sufficiently isotropic within this region to be reasonably described by the averaged dipolar potential (8.2).

In the third region, we find neither synchronization nor cluster formation. Clearly, the lack of synchronization is the direct cause of the breakdown of cluster formation [cf. Eq. (8.2)]. The loss of synchronization occurs, since the torques on the particles due to the external field become unable to overcome the torques due to the rotational friction (similarly to what is seen in three dimensions [38]).

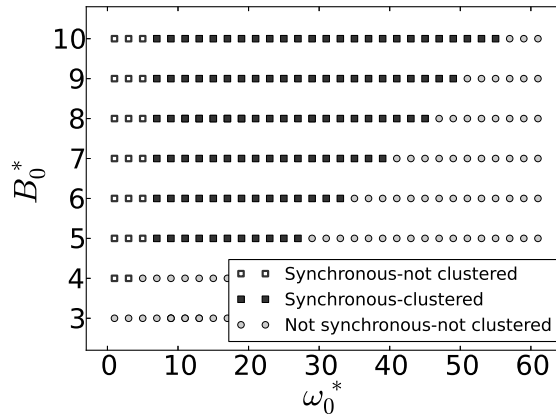


Figure 8.2.: Synchronization behavior and cluster formation depending on frequency ω_0^* and strength B_0^* of the field. The density and temperature of the system used were $\rho\sigma^2 = 0.2$ and $T^* = 1.0$, respectively.

In the previous chapter, we have presented a similar diagram for layer formation of rotationally driven dipolar particles in three dimensions. The mechanism leading to the formation of layers is quite similar to the one described here resulting in a ω_0^* - B_0^* -diagram that resembles the one depicted in Fig. 8.2. Synchronization breaks down at high frequencies close to a critical frequency $\omega_c(B_0)$, leading to the breakdown of layer formation and cluster formation. Also, the strength of the field needs to be sufficiently high to align the particles with itself. A difference can be found in the minimal driving frequency that is required for the respective pattern formation to occur: Layers in three dimensions appear at smaller frequencies than clusters do in two dimensions. This implies that symmetry breaking perpendicular to the field is less dependent on the frequency of the field than within its plane.

8.3. Relation to condensation

Now we ask to what extent the clustering behavior of the nonequilibrium, yet fully synchronized, field-driven system can be understood by that of a system interacting via Eq. (8.2), i.e., the effective potential U^{ID} . At sufficiently high strengths and frequencies of the field, this potential can be expected to describe the interaction between the particles very well without including an explicit time-dependence. This allows us to test the following hypothesis: The observed cluster formation in the driven system stems from an equilibrium, first-order phase transition between a vapor and a condensed phase that arises due to the effective interparticle interaction U^{ID} . To this end, we perform Wang-Landau MC simulations of a system interacting via the effective potential U^{ID} combined with the repulsive potential U^{rep} [see Eq. (3.7)].^{2,3}

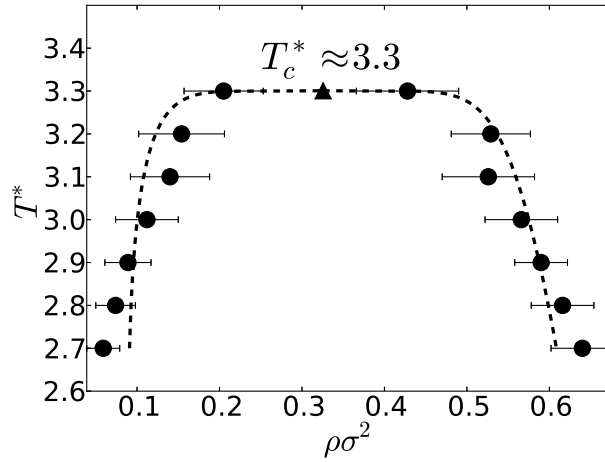


Figure 8.3.: Phase diagram in the T - ρ domain of a system interacting via the effective potential U^{ID} [see Eq. (8.2)] and the repulsive potential U^{rep} [see Eq. (3.7)] at $\mu^* = 3$. The symbol T_c (indicated by the triangular mark) denotes the critical temperature, the dots correspond to the most often sampled densities, and the error bars to the width of the sampled distributions (cf. Ref. [143] for details). The solid line corresponds to the binodal representing coexisting gas and liquid states.

The key result we obtained from these simulations is the phase diagram presented in Fig. 8.3. The presence of the binodal in the phase diagram confirms our hypothesis: The non-driven system does indeed have an equilibrium phase transition between a vapor and a condensed phase.

Now we compare this phase diagram with the thermodynamic state point of the driven nonequilibrium system that is shown in Fig. 8.1(b). We find that the latter cannot be directly placed into Fig. 8.3, since its temperature is smaller than the ones displayed. However, the temperature of the state point ($\rho\sigma^2 = 0.3$, $T^* = 1$) is considerably smaller than the critical temperature T_c , while its density is very close to the one of the critical point. This implies that the state lies well within the two-phase region of the phase diagram. Note that there are very few particles in between the clusters in Fig. 8.1b. However, this is simply due to the temperature being low

²Note that the Wang-Landau MC simulations were performed by Dr. Heiko Schmidle.

³We calculated the energy contribution of (8.2) via the well known dipolar Ewald sum. This can be done, since the dipole-dipole energy essentially reduces to U^{ID} , if the dipoles are oriented perpendicular to the monolayer (cf. Ref. [135]).

in relation to the critical temperature T_c . These findings suggest that the cluster formation observed in the (fully synchronized) field-driven system is in fact spinodal decomposition. We will come back to this point in Sec. 8.4.

Given our equilibrium binodal in Fig. 8.3, it is interesting to briefly compare our results with corresponding ones from a recent MC study of Smallegang and Dijkstra [135]. These authors calculated full phase diagrams of systems of particles interacting via the effective potential U^{ID} in three dimensions. Consistent with our findings in two dimensions, the authors found a vapor-liquid coexistence region.

Additionally, Smallegang and Dijkstra uncovered an adjacent vapor-solid coexistence region [135]. We suspect that a corresponding region also exists in our two-dimensional system, although this is not easily shown without free energy calculations. We also suspect that the type of coexistence (vapor-liquid or vapor-solid) would influence the structure of the clusters within the two-phase region. To investigate this, we performed test simulations of systems (interacting via U^{ID}) at several state points within the binodal of the phase diagram [Fig. 8.3]. Two exemplary snapshots are given in Fig. 8.4. Visual inspection suggests a solid-like (hexagonal) order at a temperature of $T^* = 0.7$ [Fig. 8.4(a)], but not at $T^* = 1.5$ [Fig. 8.4(b)]. To measure the degree of order quantitatively, we have calculated the bond order parameter

$$\psi_6 = \frac{1}{N} \sum_{n=1}^N \frac{1}{|\mathcal{N}_n|} \left| \sum_{k \in \mathcal{N}_n} \exp(i6\pi\phi_{nk}) \right| \quad (8.3)$$

for these two systems. For the one at $T^* = 0.7$, we found $\psi_6 \approx 0.78$, which is substantially higher than $\psi_6 \approx 0.53$, which we found for the $T^* = 1.5$ system. In Eq. (8.3), N is the number of particles in the simulation box, \mathcal{N}_n is the set of neighbors of particle n , and ϕ_{nk} is the angle between a fixed but arbitrary axis and \mathbf{r}_{nk} . Further, two particles are considered neighbors, if r_{nk} is smaller than the distance at which the first minimum of the pair correlation function is located. The relative difference in hexagonal order between the two systems indicates that the one at $T^* = 0.7$ is indeed inside a vapor-solid coexistence region, while the lack of order in the $T^* = 1.5$ system points to it still being within the vapor-liquid coexistence region. The temperature $T^* = 1.0$ discussed before [Figs. 8.1 and 8.2] lies somewhere in between. However, more precise statements on the location of the triple point (or the very existence of a stable liquid phase) are impossible at this point.

8.4. Dynamic coarsening

We now come back to our conjecture in Sec. 8.3 that the clustering process observed in the driven system corresponds to spinodal decomposition. To test this hypothesis, we investigated the time evolution of the cluster sizes ℓ . For phase separating systems it is well established that ℓ exhibits power law behavior [116], i.e., $\ell \propto t^\alpha$, with the corresponding exponents depending on the growth stage. Such a behavior is also seen in MD simulations. In particular, domains with growth proportional to $t^{1/2}$ [113, 114] and t [115] have been identified.

These power laws are universal in MD simulations but they do not necessarily apply to LD simulations with their modified equations of motion. This was shown, e.g., by Lodge and Heyes for the case of BD [145]. At the same time, however, the clusters in Ref. [145] were still found to grow with a power law. To check for the existence of cluster growth with a power law in non-overdamped BD simulations, i.e., LD simulations, we first investigated a “reference system”

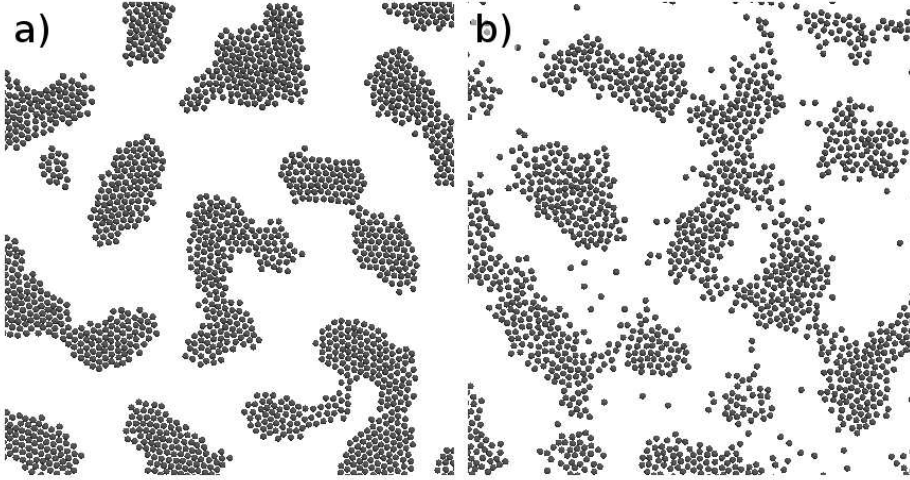


Figure 8.4.: Snapshots of (parts of) systems interacting via the effective potential U^{ID} at two different temperatures and density $\rho\sigma^2 = 0.3$. The temperature of the system depicted in (a) is $T^* = 0.7$, the one of the system in (b) $T^* = 1.5$. The snapshots were taken at time $t^* = 262.5$ after the start of the simulation.

whose equilibrium behavior is well studied. Specifically, we considered a two-dimensional LJ [see Sec. 3.1] system at $\rho\sigma^2 = 0.3$, $T^* = 0.45$ with the critical point being at $\rho\sigma^2 \approx 0.335$, $T^* \approx 0.533$ [146]. Investigating the domain size, we did indeed find a power law dependence $\ell \propto t^\alpha$ with $\alpha \approx 0.30$. Note that the cluster size was obtained by measuring the distance at which the pair correlation function assumes a value of one for the first time if the radial bins are taken to be larger than the particle diameters (cf. Refs. [113, 114, 147, 148]).

Similarly, we checked the cluster growth for a driven dipolar system and a system interacting via the potential U^{ID} . In the simulations we used 4900 particles and a density and temperature of $\rho\sigma^2 = 0.3$ and $T^* = 1.5$, respectively, which put the systems well inside the coexistence region of Fig. 8.3. The domain sizes over time that were extracted from the simulations are shown in Fig. 8.5. As can be seen, the cluster sizes of these two systems are very similar at any given time (on average the values deviate about 10% from each other). In particular, the characteristic domain sizes grow with a power law $\ell \propto t^\alpha$ with α being equal to 0.36 in both cases. We note that this is almost identical to the Lifshitz-Slyozov growth law ($\ell \propto t^{1/3}$) [cf. Sec. 6.1] [116].

From these two results we conclude that the nonequilibrium system does indeed undergo spinodal decomposition. First, the cluster growth proceeds with a power law, which is typical within the spinodal region. Second, the growth behavior remains unchanged even if the interactions between the driven dipoles are replaced with the effective ones. This emphasizes the similarity between those two systems and indicates that the phase diagram for the effective system in Fig. 8.3 remains significant for the driven and synchronized system.

8.5. Influence of hydrodynamic interactions

Due to the drive of the external field, the systems considered here are far out of equilibrium. Consequently, HIs could have a significant effect on the behavior of the colloidal particles. The drive of the external field, for instance, constantly generates rotational motion in the particles.

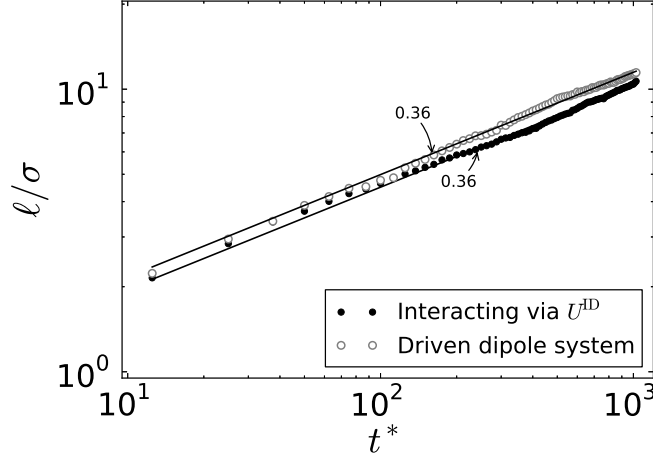


Figure 8.5.: Cluster growths for a system interacting via the effective potential and a system that is driven by an external rotating field at density $\rho\sigma^2 = 0.3$ and temperature $T^* = 1.5$ (state inside the coexistence region of Fig. 8.3). The strength and frequency of the external field are $B_0^* = 50$ and $\omega_0^* = 20$, respectively.

This motion can cause the creation of flow field in the solvent surrounding the colloids, which, in turn can result in considerable motion of the particles. Here, in this section, we want to ask to which extent HIs influence the dynamics and the cluster formation of the colloidal system.

To study the effect of solvent-mediated interactions on the system considered in this chapter, we perform BD simulations with HIs [see Sec. 4.4]. As already stated in Sec. 8.1, we consider $N = 324$ particles in a simulation box that is bounded by soft walls [Eq. (3.5) with $4\pi\epsilon_w\rho_V\sigma^3/45 \equiv 4\epsilon$], i.e., we do not use periodic boundary conditions. Therefore, it is not necessary to use special techniques (e.g., Ewald sums) to treat the long-range dipole-dipole interactions. The influence of the walls on the HIs is neglected.

In the following, we specialize to systems at temperature $T^* = 1$ and dipole moment $\mu^* = 3$. This choice corresponds to a dipolar coupling strength of $\lambda = \mu^{*2}/T^* = 9$. As we have seen, such a coupling strength is sufficiently large to enable the system to form clusters for suitable field strengths and frequencies. The density of the particles in the simulation box is of no importance in the investigated systems, since the particles typically agglomerate into a single cluster.

8.5.1. Dynamics on the particle level

First, consider the simulation snapshots of systems after clusters have formed that can be seen in Figs. 8.6(a) and (b). The former shows a snapshot of a system ($B_0^* = 50$, $\omega_0\sigma^2/D_0^T = 240$), whose particles do not interact via HIs, while HIs are included in the system associated with the latter snapshot. Since the formation of clusters can be observed in both the systems, we note as a first result that cluster formation is not prevented by the presence of HIs. As already noted at the beginning of this section, this is not a priori clear, since HIs can induce additional motion in a nonequilibrium system and the averaged potential (8.2) is only valid as an approximation to the true interparticle interaction if the translational motion of the particles during one rotational

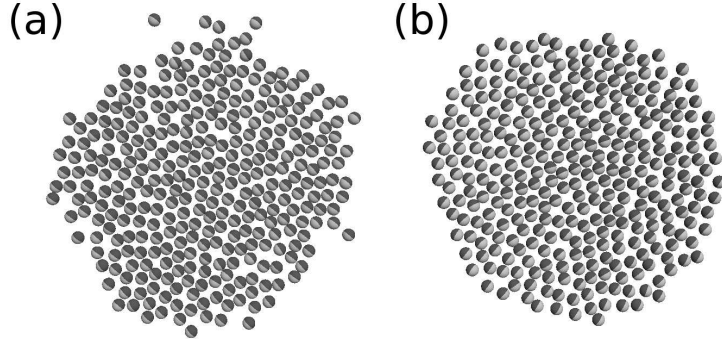


Figure 8.6.: Snapshots of systems at $B_0^* = 50$ and $\omega_0 \sigma^2 / D_0^T = 240$ after clusters have formed. (a) Without and (b) with HIs.

period of the field is small. This is certainly the case for the system without HIs: Inspecting the mean squared displacements (averaged over all the particles)

$$\text{MSD}(t) = \frac{1}{N} \left\langle \sum_{i=1}^N [\mathbf{r}_i(t) - \mathbf{r}_i(0)]^2 \right\rangle \quad (8.4)$$

at $B_0^* = 50$ and $\omega_0 \sigma^2 / D_0^T = 240$, we find that the field rotates about 30 times before a particle traverses a distance of its own diameter σ .

The driving frequency $\omega_0 \sigma^2 / D_0^T = 240$ chosen in Fig. 8.6 corresponds to $\omega_0 \approx 54$ MHz, if we assume the values of the diffusion constant ($D_0^T \approx 38 \mu\text{m}^2/\text{s}$) and particle size ($\sigma = 13$ nm) that are given in Ref. [64] for a ferrofluid.⁴

As we have seen in the previous sections, cluster formation in infinitely extended quasi-two-dimensional systems corresponds to spinodal decomposition within the coexistence region of a phase transition. This is not exactly true for the cluster formation we observe in the present section. The finite systems considered here do not undergo a phase transition. However, the used system is well suited as a model system to investigate the influence of the HIs on the dynamic behavior of the individual clusters.

In the following we ask how the collective rotational behavior of the particles changes if solvent-mediated interactions are taken into account. First, consider Fig. 8.7, which shows whether cluster formation occurs for selected state points in the field strength-frequency domain. Presented are results for both the cases with and without HIs included. Compared to the simple BD system cluster formation breaks down at smaller frequencies in the hydrodynamically interacting system. In the former, cluster formation can be observed up to $\omega_0 \sigma^2 / D_0^T \approx 450$ (at $B_0^* = 50$) while cluster formation ceases at $\omega_0 \sigma^2 / D_0^T \approx 350$ when HIs are present.

To understand the breakdown of cluster formation in more detail, we now examine the rotational motion of the particles. As explained above, synchronized rotation is necessary for

⁴In Sec. 7.10, it was stated that a driving frequency of $\omega_0^* = 10$ corresponds to about 1 GHz for ferrofluidic particles. At $B_0^* = 10$ such driven particles would perform a synchronized rotation in our LD simulations [cf. Fig. 7.5]. Arguably, at this field strength, synchronization would not occur at $\omega_0 \sigma^2 / D_0^T = 240$ in our BD simulations (see below) despite the driving frequency ($\omega_0 \approx 54$ MHz) being considerably smaller. The explanation for this discrepancy lies in the fact that the translational and rotational diffusion constants were chosen independently in Ch. 7, resulting in significantly less translational motion in the LD simulations.

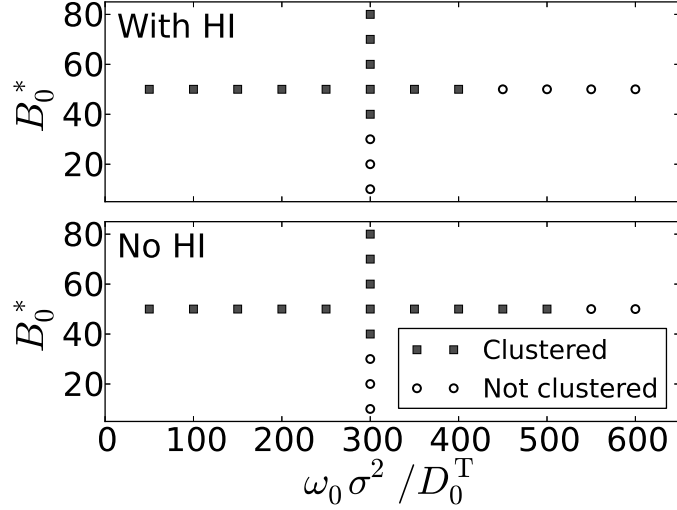


Figure 8.7.: Cluster formation (top) with and (bottom) without HIs in the field strength-frequency domain. Squares/circles indicate where cluster formation occurs/does not occur. The systems are at temperature $T^* = 1$ and dipole moment $\mu^* = 3$.

Eq. (8.2) to hold, i.e., is a prerequisite for cluster formation. Fig. 8.8 shows the absolute value of the magnetization normalized with respect to its saturation value [see Eqs. (7.7) and (7.9)] over the driving frequency $\omega_0 \sigma^2 / D_0^T$ of a system [$B_0^* = 50$, cf. Fig. 8.7] with all the hydrodynamic couplings and without HIs included. The magnetization indicates how aligned the particles are in a given state, i.e., indicates if they follow the field. As can be seen, the magnetization starts with values close to one for both the systems, corresponding to an aligned state. At $\omega_0 \sigma^2 / D_0^T \approx 270$ the magnetization begins to drop for the system that includes HIs. The magnetization in the system without HIs remains at $M/M_0 \approx 1$ up to $\omega_0 \sigma^2 / D_0^T \approx 420$.

This magnetization behavior implies that the particles in the hydrodynamically interacting system are less aligned with each other for $\omega_0 \sigma^2 / D_0^T \gtrsim 270$. In particular, the synchronization breaks down at lower frequencies resulting in a premature breakdown of cluster formation.

Comparing these results to the hydrodynamic results for layer formation presented in Sec. 7.8, we find similarities as well as differences. To start with, layer formation as well as cluster formation are stable under the inclusion of HIs. Also, in both systems, the HIs cause the breakdown of the respective structure formation at lower driving frequencies as compared to the not hydrodynamically interacting case. However, the magnetization behavior is much more influenced by the HIs in the present case. We speculate that this behavior is due to two reasons: First, the distances between the particles are much smaller in a cluster than in a layer [at the density $\rho^* = 0.1$ considered in Sec. 7.8] reducing the influence of the HIs. Second, the particles are spatially much more homogeneously distributed in an individual layer than in a two-dimensional cluster. This homogeneity could result in the HIs on the particles canceling each other out to a certain degree.

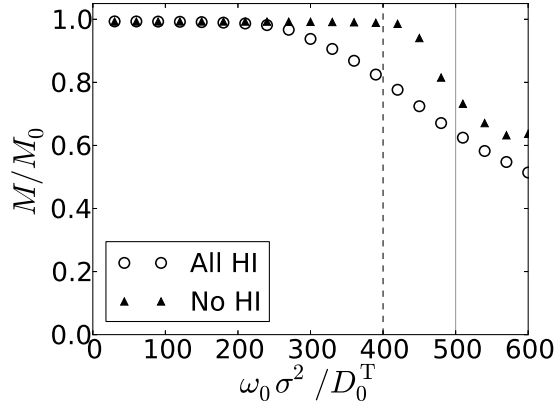


Figure 8.8.: Magnetization normalized with respect to its saturation value over the driving frequency of the external field for a system with and without HIs. The fields used are of strength $B_0^* = 50$. The vertical line indicate where cluster formation ceases with (dashed) and without (solid) HIs.

8.5.2. Cluster dynamics

We now turn to understanding the influence of HIs on the dynamics of the entire cluster. To that end, consider Fig. 8.9, which shows snapshots of the evolution of rotationally driven systems. The snapshots in the top row show a system in which HIs are not taken into account, while HIs are present in the snapshots in the lower row. The important point that is illustrated by Fig. 8.9 is that the cluster formation process is considerably accelerated by the HIs. At the intermediate time ($t' = tD_0^T/\sigma^2 = 10.8$), only a single cluster remains in the hydrodynamically interacting system [Fig. 8.9(e)], while it takes much longer for the not hydrodynamically interacting system to reach the same state [cf. Figs. 8.9(b) and (c)].

To quantify the influence of the HIs and to understand the influences of the different hydrodynamic couplings [cf. Sec. 4.4], consider Fig. 8.10, which shows the mean distance

$$\bar{d}(t) = \frac{2}{N(N-1)} \sum_{i=1}^N \sum_{j<i} r_{ij}(t) \quad (8.5)$$

between the particles for a system at $B_0^* = 50$ and $\omega_0\sigma^2/D_0^T = 240$. These particular field parameters were chosen for three reasons: First, the frequency is sufficiently high to ensure that the effective potential (8.2) describes the interparticle interaction well. Second, as seen in Fig. 8.7, cluster formation occurs for both a hydrodynamically as well as a not hydrodynamically interacting system. Third, the magnetization of the systems with these choices of $\omega_0\sigma^2/D_0^T$ and B_0^* is maximal and identical irrespective of the presence of HIs [cf. Fig. 8.8].

Specifically, Fig. 8.10 shows the evolution of \bar{d} over time for particles interacting via HIs including all the hydrodynamic couplings, for particles lacking the hydrodynamic rotation-translation/translation-rotation (RT/TR) coupling, particles lacking the rotation-rotation (RR) coupling, and particles not interacting via HIs at all [see Sec. 4.4]. In all the cases, \bar{d} assumes a constant minimal value at long times. To understand this, recall that we consider a single simulation box filled with particles here. In an infinite system, the cluster would keep growing

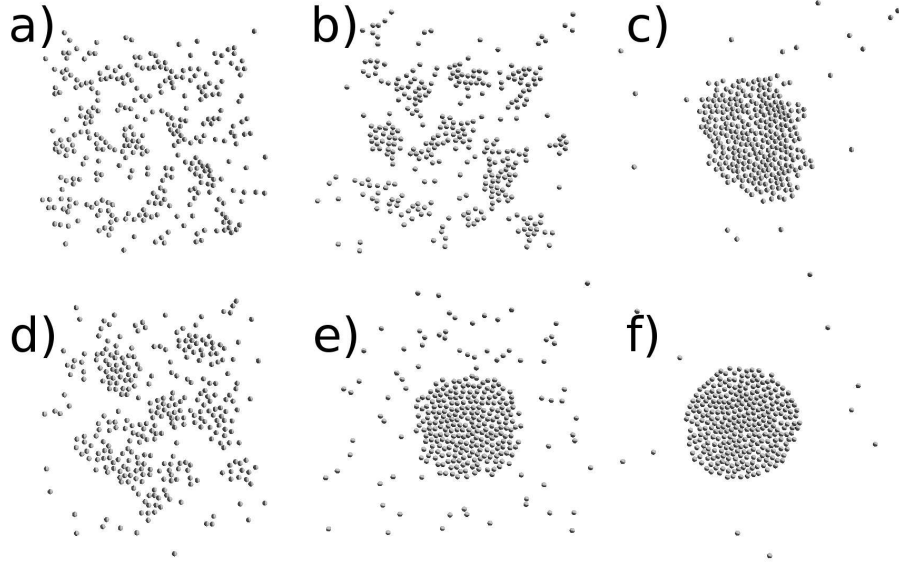


Figure 8.9.: Snapshots of a system ($\mu^* = 3$, $T^* = 1.0$, $\omega_0\sigma^2/D_0^T = 200$, $B_0^* = 80$) at different times without (top) and with (bottom) HIs. The snapshots in the first column were taken at $t' = tD_0/\sigma^2 = 2.5$ and the ones in the second column at $t' = 10.8$ after the start of the simulation. The ones in (c) and (f) correspond to the state of the system at $t' = 138.5$ and 43, respectively. These simulations do not include periodic boundary conditions. Instead, the particles are confined to a simulation box that is very large compared to the space that the particles are initially put into, ensuring minimal particle-wall interactions. Consequently, the snapshots do not show the entire simulation box but are centered on the clusters.

in time indefinitely with a power law behavior [114–116], since the process corresponds to spinodal decomposition. Here, however, the growth process stops once all the particles have been incorporated into the cluster and a stationary state is reached.

In the systems that include solvent-mediated interactions (All HI, No RT/TR, No RR), the value of \bar{d} drops significantly faster than in the case without any HIs. Consequently, the average distance between the particles decreases faster, which means that the cluster formation process is sped up. The acceleration is neither influenced by the lack of the RT/TR nor the RR coupling, which implies that the TT coupling alone is responsible for this effect. Note, however, that the lack of the presence of the RT/TR coupling expresses itself by a different value of \bar{d} at long times [see Fig. 8.10].

The RT/TR coupling does have another interesting influence on the dynamic behavior of the particles. In Fig. 8.11, the mean angular frequency of the particles with respect to the cluster center over the distance from the center is shown for a system at $B_0^* = 50$ and $\omega_0\sigma^2/D_0^T = 240$. Values for the hydrodynamically interacting case with all the couplings included as well as the case lacking the RT/TR coupling are presented. In the system that includes the RT/TR coupling, the angular velocity of the particles differs from zero at all the displayed distances from the cluster center r_c^* . Hence, the particles perform a rotation around the cluster center in the rotational direction of the external field. The system lacking the RT/TR coupling does not show such a rotational behavior. As can be seen in Fig. 8.11, the mean angular frequency of the particle

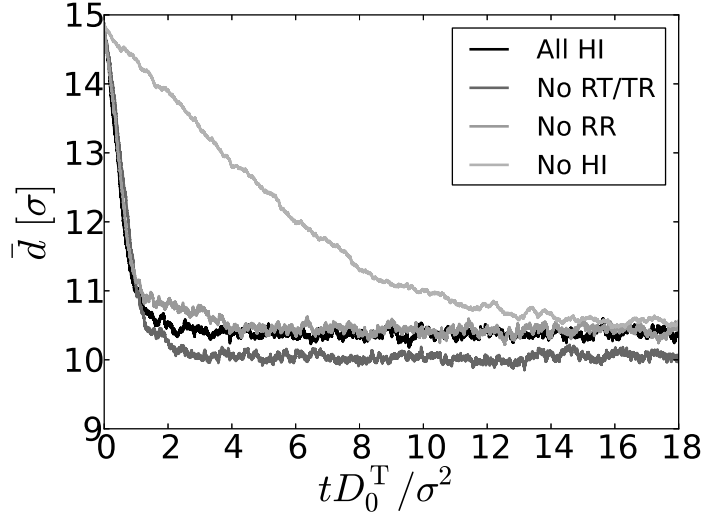


Figure 8.10.: Mean distance between the particles over time \bar{d} in a system ($B_0^* = 50$, $\omega_0\sigma^2/D_0^T = 240$) with all hydrodynamic interactions included (All HI), without the hydrodynamic RT/TR coupling (No RT/TR), without the hydrodynamic RR coupling (No RR), and without all HIs (No HI).

around the cluster center is essentially zero at all distances.

This collective rotation is caused by the individual, field-driven rotations of the particles. The rotational motion of the particles creates a flow field that induces translational motion in all the other particles [see the argument given below Eqs. (4.69)-(4.74)]. Therefore, the TR coupling alone is responsible for this behavior. The RT coupling does not contribute in any way to the cluster rotation.

To understand the reason for the collective rotational behavior, consider two particles that are located at a distance from each other on the x -axis in a right-handed coordinate system. Due to the TR coupling, anticlockwise rotation (following the application of a torque) of the particle at the larger value of x results in the other particle moving in the negative y -direction. By realizing that the flow fields follow the rotation of the particle, this process can be easily understood. On the other hand, an anticlockwise rotation of the particle at smaller values of x causes the other particle to move into the positive y -direction (for a sketch, see Ref. [82]).

As we have seen in Sec. 8.5.1, HIs result in a premature breakdown of cluster formation, i.e., a breakdown at smaller driving frequencies of the field (relative to the case without HIs). It stands to reason that the cluster rotation induced by the HIs has a significant influence on this behavior. The particles perform additional translational motion (around the cluster), which makes the effective potential (8.2) less accurate as a description for the interparticle interaction at a given driving frequency. The more the particles move during one period of the field, the less does the effective potential capture the actual interaction between the particles.

Moreover, note that the RR coupling does not seem to have any significant influence on the dynamic behavior of the cluster. That is, it does not contribute to the accelerated cluster formation or the cluster rotation. The former is illustrated by Fig. 8.10, which shows that the mean distance \bar{d} behaves essentially identically to the system with all the HIs included. The fact

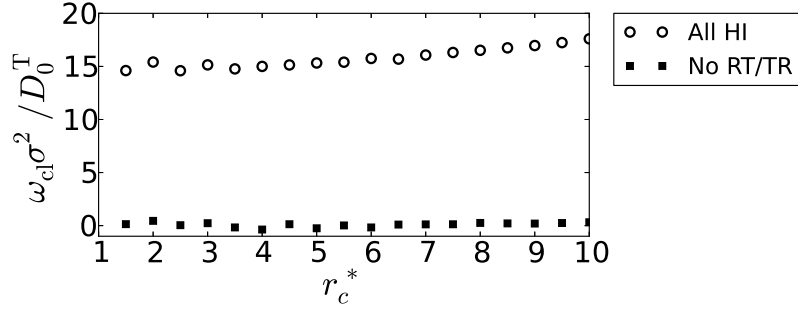


Figure 8.11.: Mean angular frequency $\omega_{cl}\sigma^2/D_0^T$ around the cluster center of the particles over distance from particle center r_c^* for a system at $B_0^* = 50$ and $\omega_0\sigma^2/D_0^T = 240$. Shown are values for a system interacting via all the hydrodynamic couplings and for a system lacking the RT/TR coupling.

that the cluster rotation is not influenced by the RR coupling can be seen in Fig. 8.11. Despite the presence of the RR coupling, the cluster does not rotate if the RT/TR coupling is absent.

Finally, note that it would have been very interesting to see the actual domain growth of the clusters when HIs are present similar to what is plotted in Fig. 8.5. However, the fact that we did not use periodic boundary conditions in these simulations makes an accurate determination of the domain size growth in the presence of HIs very difficult.

8.5.3. Internal structure of the cluster

In a recent experimental study, Weddemann et al. [27] showed the existence of cluster formation in two-dimensional systems of (permanently) dipolar particles that are driven by a rotating external field. In particular, the authors of [27] observed the formation of hexagonally ordered particle agglomerates in their experiments.

In Sec. 8.3, we were able to reproduce clusters of hexagonal order at very low temperatures inside of the two-phase coexistence region. We conjectured that the hexagonally ordered clusters occur in the vapor-solid coexistence region, i.e., at coupling strengths above the ones related to the vapor-liquid region.

As shown in the previous section, HIs can have a significant influence on the collective motion of the particles. Here, we want to investigate, whether HIs preserve the internal cluster structure. Despite experimental evidence of the hexagonal order, this fact is debatable since it remains unclear to what degree the rotational motion of the magnetic particles in the experimental work [27] follows the dipole moment.

In order to gain insight into the emergent (hexagonal) structures in the present, finite systems, we consider the bond order parameter (8.3) at different dipolar coupling strengths λ . The systems considered in the following are of sufficiently high coupling strengths ensuring that cluster formation does indeed occur.

In Fig. 8.12, ψ_6 as function of the dipolar coupling strength λ for systems ($B_0^* = 50$) with and without HIs at $\omega_0\sigma^2/D_0^T = 240$ and 300 is shown. We note that ψ_6 is essentially independent of time in the stationary situation, where all the particles are part of the cluster. At $\omega_0^* = 300$, the bond order parameter increases with λ for both the hydrodynamically as well as the not hydrodynamically interacting system. If HIs are not present, an increase from $\psi_6 \approx 0.52$ at

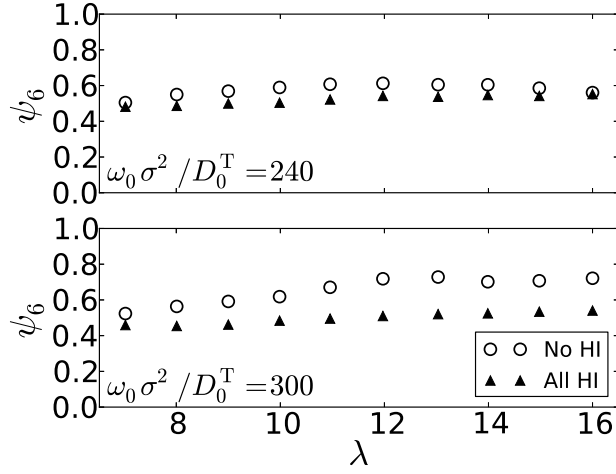


Figure 8.12.: Hexagonal order parameter ψ_6 over coupling strength λ for a system ($B_0^* = 50$, $T^* = 1$) with and without HIs at (top) $\omega_0\sigma^2/D_0^T = 240$ and (bottom) $\omega_0\sigma^2/D_0^T = 300$.

$\lambda = 7.02$ to $\psi_6 \approx 0.72$ at $\lambda = 16$ can be observed. This increase qualitatively agrees with the one observed in the LD simulations in Sec. 8.3. In the system with HIs included, the bond order parameter ψ_6 increases considerably less with increasing coupling strength. However, there is still significant order in the system.

In the system with $\omega_0\sigma^2/D_0^T = 240$ and HIs included, ψ_6 behaves similarly to the case with $\omega_0\sigma^2/D_0^T = 300$ and HIs. If these interactions are not taken into account, however, less hexagonal order than in the $\omega_0\sigma^2/D_0^T = 300$ system can be observed. The smaller frequency allows for more translational motion during one rotational period of the field, resulting in more spatial inhomogeneity.

Now consider Fig. 8.13, which shows the pair correlation functions of a system ($B_0^* = 50$, $\omega_0\sigma^2/D_0^T = 300$) with and without HIs included. The pair correlation function of the not hydrodynamically interacting system shows a double peaked maximum after the first minimum, which is typical for a hexagonally ordered system. The hydrodynamically interacting system, on the other hand, does not have this feature. Hence, the particles tend to have six angularly equally distributed neighbors as shown by the value of ψ_6 [cf. Fig. 8.12], but seem to lack the long-range positional order of a hexagonally structured system. Further, the extrema are much more pronounced in the system without HIs, indicating a more ordered state.

In conclusion, in both systems in Fig. 8.12, the HIs tend to weaken the hexagonal (or hexatic) order present in the system. The lower value of ψ_6 in systems with HIs can be explained by the collective cluster rotation induced by the hydrodynamic TR coupling. The particles rotate around the cluster center and do not stay at fixed lattice sites. This behavior results in a reduction of the bond order parameter and the hexagonal structure in the system.

Finally, note that Prof. Holger Stark has recently conducted an investigation of the structure of a closely related system [149]. The system consisted of particles that only interact via HIs, are confined to a monolayer, and have fixed angular velocities. It was found that hexagonal particle agglomerations rotate, with the hexagonal order melting and recrystallizing periodically. In the system focused on in this section, no such phenomenon could be observed. We attribute this to

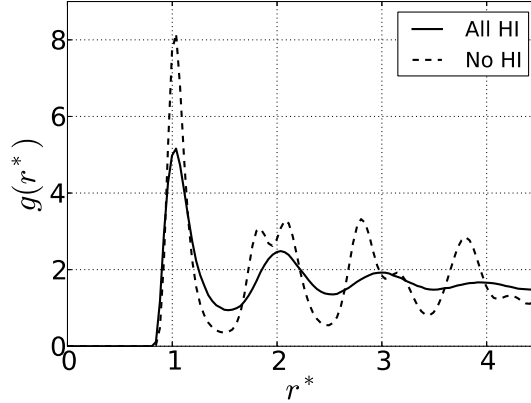


Figure 8.13.: Pair correlation functions of systems at $B_0^* = 50$ and $\omega_0\sigma^2/D_0^T = 300$ with and without HIs included.

the presence of dipolar interactions in our system and a lack of Brownian motion in [149].

8.6. Conclusions

In this chapter we have investigated the formation of two-dimensional aggregates in monolayers of dipolar particles that are driven by rotating external in-plane fields.

The first result of this chapter is a nonequilibrium “phase” diagram, which shows the regions of synchronization and cluster formation in the $\omega^* - B_0^*$ -domain. At high frequencies, the synchronization of the particles with the field breaks down, which results in a breakdown of cluster formation. Similarly, we do not find cluster formation at low frequencies. Here, the effective interaction between the particles is not well enough described by U^{ID} , since the particles move considerably during one rotational period of the field. This changes in between those frequencies, where the particles rotate synchronously and sufficiently fast, which leads to the formation of clusters.

Next, we established the clustering phenomenon to be a consequence of a phase transition between a vapor and a condensed phase. This was done in two steps: We began by uncovering a phase transition via Wang-Landau MC simulations in a system interacting via the effective potential U^{ID} . Recall that this potential describes the interactions between the particles very well in the driven system at sufficiently high frequencies of the field. Then we examined the domain growth of the driven system within the binodal region of the phase diagram. As expected for spinodal decomposition, we found the characteristic cluster size to grow with a power law. Additionally, it essentially agrees with the domain growth of the non-driven system interacting via the effective potential U^{ID} . These facts lead us to conclude that the clustering process corresponds to the pattern formation occurring inside the coexistence region of a vapor-liquid phase transition.

We concluded our analysis with an investigation of the influence of HIs on the driven system. The cluster dynamics and formation is influenced in three major ways by HIs. First, HIs accelerate the cluster formation process. While the particles approach each other, flow fields are created that drag other particles along. Second, we have shown HIs to induce a collective

cluster rotation. Without HIs no such rotation can be observed. The driven rotating particles pull the solvent with them in their rotational motion, which results in the translational motion of the particles around the cluster center. This phenomenon is related to the findings of a recent study, in which the interplay of HIs and confinements was investigated [150]. It was shown that suitable confinements can be used to create directed translational motion from particle rotations, suggesting that it might be interesting to examine the effects of different confinements on the driven dipolar particles investigated here. As a last major point, we have shown cluster formation to cease at lower driving frequencies of the field. We attribute this to an earlier breakdown of synchronization if HIs are present and an increase in translational motion due to the collective cluster rotation.

Usually, HIs seem to affect colloidal nonequilibrium clustering phenomena less significantly than in the present system. As an example, consider the process of colloidal gelation in two-dimensional Lennard-Jones systems [151]. In contrast to our system, the agglomeration of the particles in [151] is only marginally influenced by the HIs. In general, however, HIs can significantly alter nonequilibrium processes. For instance, HIs can enhance ratchet effects [52, 53] or synchronize the motion of eukaryotic [48] or bacterial [152] flagella.

Given the findings of this chapter, it is interesting to compare them to recent experimental results. Indeed, cluster formation in monolayers resulting from a rotating external field has been observed multiple times [27, 40, 138–140]. In most of these publications induced dipolar particles are brought to self-assemble into two-dimensional aggregates. The only paper in which particles with a permanent dipole moment were used (Ref. [27]) features a dipole-dipole coupling strength ($\lambda = \mu^2/k_B T \sigma^3$) that is dominated by the dipole-field coupling strength ($\lambda_{\text{DF}} = \mu B_0/k_B T$). There, the ratio $\lambda_{\text{DF}}/\lambda$ is about 6, which is larger than the largest ratio that appears in Fig. 8.2. Consequently, we expect the particles in [27] to rotate synchronously with the field, resulting in the effective interaction U^{ID} and the observed cluster formation.

The clusters found in the literature are typically hexagonally ordered. In our LD simulations this becomes more and more true with increasing frequency and strength of the field as well as with decreasing temperature. The main reason for the difference between simulations and experiment is likely the difference in particle size: Micrometer-sized particles were used in Refs. [27, 40, 138, 140], resulting in large dipole-dipole coupling strengths λ . This reduces the significance of the thermal motion compared to particles of smaller size, which usually have smaller coupling strengths. Indeed, at low temperatures, considerable hexagonal order [cf. Fig. 8.4] can be observed in our simulations.

To have a full phase diagram of the effective system would be very helpful in this context: It would allow for a precise determination of the onset of hexagonal order in the system and the general structural order of the colloidal suspension at any given state point (cf., e.g., Ref. [135] for details on how to determine the phase diagram via free energy calculations).

Our hydrodynamic results indicate that HIs tend to decrease the hexagonal order in systems of permanent dipoles. Since the dipoles in [40, 140] are of induced nature, we do not expect the structures to be influenced by the HIs in these systems. In particular, the TR coupling should not play a significant role. However, in the experiments of Weddemann et al. [27], the particles might follow the dipole moments, which could give rise to TR induced motion and, therefore, a decrease in structural order. The fact that strong hexagonal order was observed in [27] might indicate that the rotational motion of the particles does not closely follow their magnetic moment. On the other hand, as mentioned above, the size of the particles used in Ref. [27] causes strong dipolar coupling strengths, which might emphasize the effects of the dipole interactions.

Further, the driving frequencies used in the publications [27, 40, 138, 140] are considerably

smaller than the ones used here. This can once again be explained by the size of the particles: Larger particles typically have larger friction coefficients, which, as test simulations show, result in cluster formation at lower frequencies of the field. In fact, as already discussed in Sec. 7.10, if we assume the particles to be about $1\ \mu\text{m}$ in diameter with a density of $5\ \text{g}/\text{cm}^3$, we find a driving frequency of $\omega_0^* = 10$ to correspond to a frequency of about 10 kHz at room temperature ($T = 293\ \text{K}$).

In this chapter, we used specific friction coefficients in our LD simulations ($\xi_T^* = 13.5$, $\xi_R^* = 0.45$). As suggested in the previous paragraph, the occurrence of cluster formation is, however, not exclusive to those. Indeed, in test simulations we found clusters at a multitude of different friction coefficients (e.g., at $\xi_T^* = 13.5$, $\xi_R^* = 0.1, 0.45, 1, 5$ and $\xi_R^* = 0.45$, $\xi_T^* = 5, 13.5, 20, 50, 67.5$). These simulations indicate that the larger the translational friction coefficient, the smaller the frequency at which clusters begin to form. Increasing the rotational friction coefficient, on the other hand, seems to shift the breakdown of layer formation to lower frequencies of the field.

The coarsening process investigated in this chapter can universally be observed in phase separating systems. Condensation transitions and spinodal demixing in binary fluids or metallic alloys are popular examples of this. The process reported in this study is exceptional, however, in that the existence of a liquid-vapor phase transition in ordinary dipolar soft and hard sphere systems without additional (van der Waals-like) attraction is still a hotly debated topic and one of the big unresolved questions regarding these particles [61, 62, 73, 153]. But as shown here, such a phase transition can be induced via an external time-dependent field.

The system considered in this study is driven and, consequently, inherently in a nonequilibrium state. The dynamic coarsening observed in spinodal decomposition, on the other hand, is a process typically associated with non-driven systems. It is, however, not unique to those. Two examples are active Brownian swimmers performing a “run-and-tumble” motion such as *E. Coli* bacteria [154] and self-propelled rods [155], both of which exhibit clustering behavior. With the ongoing and rising interest in dynamics and nonequilibrium processes we expect an increasing amount of systems to be uncovered that are driven into cluster or pattern formation with behaviors similar to the one described here.

9. Rotational ratchets with dipolar interactions

So far, we have investigated the effects of rotating fields on colloidal suspensions of dipolar particles. In this chapter, we want to shift the focus to a different class of time-dependent fields. Specifically, we are interested in the effects of oscillating fields that lack a net rotating component on systems of dipolar particles. One of the most intriguing aspects of such fields is that they can give rise to a rotational ratchet effect.

In general, ratchets or, as they are sometimes called, Brownian motors, are devices that are able to extract directional motion from Brownian random noise [156]. Rectifying Brownian noise into directional motion is only possible in out-of-equilibrium situations. In thermal equilibrium a ratchet effect would violate the second law of thermodynamics [157, 158].

Thermal ratchet effects have been known for a long time. Recently, however, they are again gaining attention due to their possible applications in biological transport [159, 160] and nanotechnology [161, 162]. Most of the research on Brownian motors has been focused on directed translational motion. Exceptions are recent studies on the rotational ratchet effect in ferrofluids, which has been investigated theoretically [46, 47, 163] as well as experimentally [164].

The ratchet effect reported in [46, 47] consists of a noise-driven directed rotation of the particles, which are exposed to a field without a net rotating component. The rotations of the particles are associated to an effective torque, which is transferred to the solvent medium. This latter torque is of macroscopic size, making the ferrofluid ratchet effect experimentally detectable [164].

The theoretical investigations so far have been performed on the basis of the single-particle Langevin- and Fokker-Planck equations [47, 163]. Interactions between the ferromagnetic colloids have mostly been neglected [47], the argument being that the concentration of magnetic particles is extremely small in many ferrofluids (volume fraction $\approx 1\%$). In more concentrated samples, however, one would expect the magnetic dipole-dipole interactions between the particles to become important. Indeed, a well known effect is the chain formation of the particles triggered by the anisotropy, particularly the head-to-tail preference, of the dipole interactions. There is, to our knowledge, only one theoretical study in which the impact of the dipolar interactions on the ratchet effect has been investigated [163]. This study approximates the interactions on a mean-field level, i.e., all the particles experience a homogeneous effective field.

In this chapter, we will investigate the impact of the true dipolar interactions on a particle level, i.e., by BD computer simulations. In this way we can not only capture the full anisotropy and range of the interaction (which is known to be crucial for self-organization processes in dipolar systems [20, 38, 141]), but also the fact that the particles are mobile.

This chapter is organized as follows: In Sec. 9.1, we give some background information on the rotational ratchet effect. Then, in Sec. 9.2, we present the model and the simulation methods used throughout this chapter. The next section deals with the rotational thermal ratchet effect in non-interacting systems. Here, we will investigate the angular trajectories of the particles and the influence of the strength of the noise and the external field. In Sec. 9.4 we will then turn to systems, in which the particles interact via a short-range repulsive and a dipole-dipole potential. We will show that dipolar interactions can enhance as well as suppress the ratchet effect and we will analyze the mechanisms behind these effects. Further, we will show that the short-range

isotropic, repulsive potential has a significant influence on the ratchet behavior. The chapter is then closed with a brief summary and conclusions.

Note that most of the results shown in this chapter have been published in Ref. [165].

9.1. Background

The first investigations on the rotational ratchet effect were done by Engel et al. [46, 47]. In these references, isolated particles were considered that interact with the external field

$$\mathbf{B}^{\text{ext}}(t) = B_x \mathbf{e}_x + B_y [\cos(\omega_0 t) + \sin(2\omega_0 t + \delta)] \mathbf{e}_y. \quad (9.1)$$

Specifically, the field has a constant component in x -direction and an oscillating, yet asymmetric component in y -direction. The important point is that this field involves only oscillations, but no full rotations, irrespective of the phase shift δ . Nevertheless, it turns out that the particles can perform directed full rotations. We note that the ansatz (9.1) is, however, by no means the only field with which a ratchet effect can be realized. In fact a multitude of different fields are suitable, if certain conditions are met: B_x must be non-vanishing and there cannot be a Δt such that $B_y(t) = B_y(-t + \Delta t)$ (see Ref. [47] for a detailed discussion of this issue).

In Ref. [47], the systems were studied with BD simulations and numerical evaluations of the Fokker-Planck (FP) equation. The angular FP equation that was solved is given by

$$\partial_t P = \nabla(P \nabla U) + D_0^R \nabla^2 P \quad (9.2)$$

$$= \frac{1}{\sin^2 \theta} \partial_\phi (P \partial_\phi U) + \frac{D_0^R}{\sin \theta} \partial_\theta (\sin \theta \partial_\theta P) + \frac{D_0^R}{\sin^2 \theta} \partial_\phi^2 P, \quad (9.3)$$

where $P(\phi, \theta, t)$ is the probability density of finding a particle at an angular position (ϕ, θ) at time t . The angles ϕ and θ are the polar angle and the azimuthal angle of spherical coordinates with the polar angle corresponding to the angle between the x -axis and the projection of the considered positional vector into the $x - y$ -plane. The function U in (9.2) is the potential

$$U = -\sin \theta (B_x \cos \phi + B_y [\cos(\omega_0 t) + \sin(2\omega_0 t + \delta)] \sin \phi). \quad (9.4)$$

Moreover, Engel et al. evaluated the rotational BD equation

$$\partial_t \phi = -B_x \sin \phi + B_y [\cos(\omega_0 t) + \sin(2\omega_0 t + \delta)] \cos \phi + \sqrt{2D_0^R} \xi_\phi(t). \quad (9.5)$$

Here, ξ_ϕ is a δ -correlated noise source with zero mean. Eq. (9.5) corresponds to the angular BD equations of motion of the system under the restriction that the motion of the particles is confined to the $x - y$ -plane. This means that θ is constant and set to $\pi/2$.

Both the evaluation of the FP equation as well as the BD simulations showed the ratchet character of the driven system.

9.2. Model and simulation methods

In this chapter, we consider a three-dimensional system of dipolar colloidal particles. We model these particles by a DSS potential [Eq. (3.14)], which we use in BD simulations [see Sec. 4.3].

The particles are driven by the external field (9.1) suggested in the previous section, which causes the particles to experience a torque [see Eq. (7.2)].

We consider $N = 500$ particles in our simulation box with periodic boundary conditions. The long-range dipolar interactions are taken into account by using the Ewald summation method [cf. Sec. 5.2].

9.3. The thermal ratchet effect in a non-interacting system

As a background for our investigation of the impact of dipolar interactions, we discuss in this section BD simulation results for the rotational thermal ratchet effect in systems of non-interacting particles. To this end, we analyze the trajectories of the particles under the influence of the external field (9.1) as well as the corresponding torque. Further, we investigate the dependence of the ratchet effect on the strength of the external field versus that of the noise. We note that some of the points discussed in this section have already been investigated in Ref. [47] via numerical integration of the respective FP equation [cf. Sec. 9.1]. Our present BD results supplement these previous theoretical results.

The systems we consider in this section are characterized by a temperature $T^* = 0.2$. The particles are driven by a field of frequency $\omega\sigma^2/D_0^T = 15$, y -field component $B_y^* = 1$, and various values of B_x^* . The dipole moment is set to $\mu^* = 1$, such that the dipole-field coupling is $\mu B_y/k_B T = \mu^* B_y^*/T^* = 5$.

Since neither repulsive nor dipolar interactions are taken into account in this section, the density can be chosen arbitrarily. With these choices of the variables, our results are easily comparable to the ones from Ref. [47] (for the precise relations between the dimensionless variables in this chapter and those in [47], see Appendix F).

To start with, we show in Fig. 9.1 the mean orientation of the particles,

$$\bar{\mathbf{S}}(t) = \frac{1}{N} \sum_{i=1}^N \mathbf{e}_i(t), \quad (9.6)$$

for the external field (9.1) with $B_x^* = 0.1, 0.3$ and $\delta = 0$. As can be seen, \bar{S}_x is essentially constant, while \bar{S}_y follows (with a phase lag) the oscillating component of the external field indicated by the dotted line in Fig. 9.1. Interestingly, while \bar{S}_x is increased for the field with $B_x^* = 0.3$ over the field with $B_x^* = 0.1$, \bar{S}_y remains essentially unchanged. We will later see that this is of crucial importance for understanding the impact of interactions.

The behavior of the mean orientation seen in Fig. 9.1 appears essentially deterministic. The actual ratchet effect is illustrated in Fig. 9.2, where we plot two angles ϕ_i and $\bar{\phi}$. The former is the angle that an (arbitrary) particle i encloses with the x -axis. It first remains close to a multiple of 2π (indicated by the horizontal lines) corresponding to the particle oscillating around the x -direction of the field. This behavior continues, until a noise-induced full rotation (i.e., a crossing of a horizontal line) occurs. One also sees that the forward rotation, i.e., an increase by 2π , occurs more often than the corresponding backward rotation. This illustrates the directional character of the ratchet effect.

The second quantity $\bar{\phi}$ depicted in Fig. 9.2 corresponds to the averaged value of the angles ϕ_i of all the particles

$$\bar{\phi}(t) = \frac{1}{N} \sum_{j=1}^N \phi_j(t). \quad (9.7)$$

In contrast to ϕ_i this average angle $\bar{\phi}$ increases monotonically, since individual fluctuations are smeared out.

Irrespective of these differences between ϕ_i and $\bar{\phi}$, Fig. 9.2 clearly demonstrates that there is a net rotational motion in one direction. This corresponds to the presence of a net torque. We calculated the net torque as an average of the time-dependent torque over one period of the field,

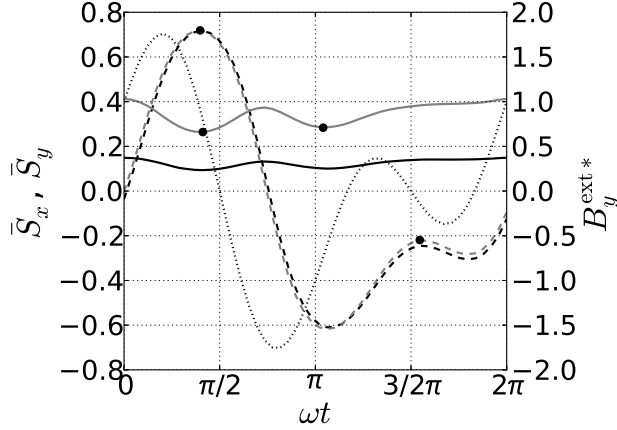


Figure 9.1.: Mean orientation of the particles during one rotational period of the field for non-interacting systems with $B_x^* = 0.1$ (black lines) and $B_x^* = 0.3$ (gray lines) at $\delta = 0$. The x - and y -components of $\bar{\mathbf{S}}(t)$ are indicated by solid and dashed lines, respectively. The dotted line shows the field component in y -direction $B_y^{\text{ext}*}$. The dots are results from Ref. [47] for the $B_x^* = 0.3$ system [see the end of Sec. 9.3].

i.e.,

$$\langle \bar{\mathbf{T}} \rangle = \frac{1}{\tau} \int_{t_0}^{t_0+\tau} \bar{\mathbf{T}}(t) dt \quad (9.8)$$

where

$$\bar{\mathbf{T}}(t) = \frac{1}{N} \sum_{i=1}^N \boldsymbol{\mu}_i(t) \times \mathbf{B}_i(t). \quad (9.9)$$

with

$$\mathbf{B}_i = -\nabla_{\boldsymbol{\mu}_i} \sum_{j \neq i} U^{\text{DSS}}(\mathbf{r}_{ij}, \boldsymbol{\mu}_i, \boldsymbol{\mu}_j) + \mathbf{B}^{\text{ext}}. \quad (9.10)$$

Numerical data for the net torque that the particles experience for $B_x^* = 0, 0.1$, and 0.3 over the phase difference δ are presented in Fig. 9.3 [cf. Eq. (9.1)]. It is seen that $\langle \bar{T}_z^* \rangle$ is indeed non-zero and (at $\delta = 0$) positive, reflecting the net rotation of the particles to the right. Increasing the phase difference δ , the value of $\langle \bar{T}_z^* \rangle$ changes and even assumes negative values. This implies that the particles can perform forward as well as backward rotations depending on δ .

We now consider in more detail the dependence of the net torque on the strength of the constant field contribution B_x^* . At $B_x^* = 0$, the external field simply performs an oscillation into the y -direction. In that case, no net torque can be observed. With only one direction distinguished by the field, directional rotational motion simply cannot occur [157]. For non-vanishing x -components the magnitude of $\langle \bar{T}_z^* \rangle$ depends strongly on the value of B_x^* . As illustrated by Fig. 9.3, increasing B_x^* from 0.1 to 0.3 results in considerably larger torques $\langle \bar{T}_z^* \rangle$. We explain this increase as follows: At higher values of B_x^* , the particles are much more aligned into the x -direction of the field, and thus in the plane of the field. The latter point is illustrated by Fig. 9.1: \bar{S}_x is considerably larger for $B_x^* = 0.3$ than for $B_x^* = 0.1$ while \bar{S}_y remains essentially unchanged. In other words, higher values of B_x^* ensure that the particles remain within the plane of the field without dampening the oscillations of the dipole moments in the y -direction.

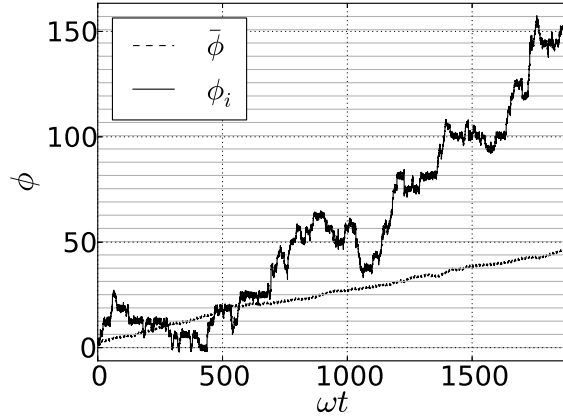


Figure 9.2.: The angular trajectories in terms of the polar angle ϕ_i of an individual particle and the system-averaged angle $\bar{\phi}$ at $B_x^* = 0.3$ and $\delta = 0$.

It is well established that ratchet effects, in general, depend strongly on the strength of the noise relative to the deterministic contributions to the equations of motion [157]. For the present system, this interplay is illustrated in Fig. 9.4, where we plot the torque as a function of the dimensionless temperature T^* . Inspecting Eq. (4.45), we see that the temperature T^* influences the strength of the deterministic torque (due to the field) alone, if the diffusion constant is kept constant. In other words, T^* is a measure for the aforementioned ratio of conservative torques to random noise. Small temperatures correspond to systems that are dominated by deterministic torques, while large temperatures correspond to noise-dominated systems.

In Fig. 9.4, we can see that the ratchet effect is strongest for finite temperatures in the range $T^* \approx 0.05 - 0.2$. This means that the ratchet effect decreases in strength for too small or too large noise contributions. If the temperature is too small, the field dominates the rotational motion of the particles, which are effectively unable to perform rotations against the field. At large temperatures, on the other hand, the noise dominates such that the influence of the field becomes insignificant. However, without the nonequilibrium influence of the external driving field, the ratchet effect cannot exist [157, 158].

As described in Sec. 9.1, the behavior of a single dipole in the oscillating field (9.1) was investigated on the basis of a FP equation in Ref. [47]. Consistent with our results, the authors of Ref. [47] found a maximum in the strength of the net torque at finite values of the noise intensity. Moreover, for the particular choice $B_x^* = 0.3$, our results for the mean orientation and the net torque [see Figs. 9.1 and 9.3] are in quantitative agreement with those in Ref. [47] (see the Appendix F for the relationship between the dimensionless units). As an illustration, some of the results from Ref. [47] are plotted in Figs. 9.1 and 9.3. Moreover, see Ref. [164] for a comparison of these theoretical results (mean torque over phase difference) to experimental findings.

9.4. Influence of the particle interactions

In a ferrofluid, the particles interact with each other via short-range repulsive as well as dipolar interactions. These interactions can be neglected in strongly diluted ferrofluids, however, they do become important when the density of the dipolar particles becomes higher.

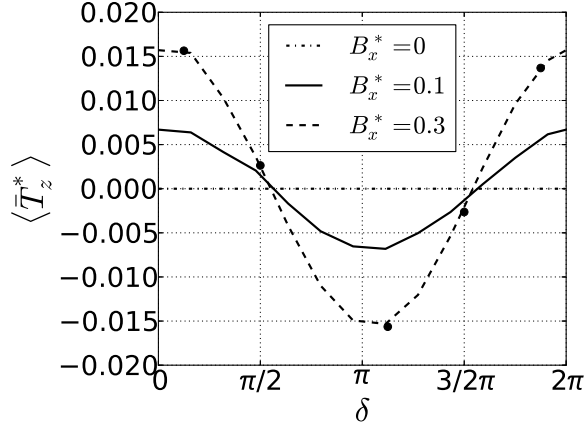


Figure 9.3.: Averaged torque during one rotational period of the field as function of the phase difference δ for $B_x^* = 0, 0.1$, and 0.3 (and $B_y^* = 1$). The dots are results from Ref. [47] for the $B_x^* = 0.3$ system.

As has been shown in previous studies, particle interactions can indeed have a profound influence on ratchet effects [157, 163, 166]: For instance, in a translational ratchet, they can reverse the direction of the effect or even give rise to it in the first place [157, 167]. The latter is also true for the rotational ratchet effect. It was shown in Ref. [163] that dipolar interactions treated on a simple mean-field level can induce effective particle rotations despite a vanishing field component B_x .

In the following, we choose a density of $\rho^* = 0.2$ corresponding to a dipolar fluid of moderate packing fraction $\eta = \pi\rho\sigma^3/6 \approx 0.105$ [168]. This choice ensures that the dipolar interactions play a crucial role at higher coupling strengths. The frequency of the oscillating field is again set to $\omega\sigma^2/D_0^T = 15$ and we use a phase difference of $\delta = 0$. Regarding the interaction parameters, we consider a range of values for the dimensionless dipole moment μ^* and different values of the dimensionless temperature T^* . In this way, we can explore both the impact of the dipolar interactions (3.9) and that of the repulsive interactions (3.7).

Note that while we vary μ^* (and, thus, λ), we keep the products $\mu^*B_x^*$ and $\mu^*B_y^*$, i.e., the dipole-field coupling, fixed. To indicate the used field strength, we therefore use the notation $B_\gamma^+ \equiv \mu^*B_\gamma^*$.

In the lower temperature systems ($T^* = 0.2$) considered here, we use $B_y^+ = 1$. With this choice, the interaction strength between the dipoles and the field remains as in the previous section. In the systems with $T^* = 1$, we use proportionally stronger external fields with $B_y^+ = 5$. The relative strength of the external field compared to the Brownian noise is then equal that in the low temperature case.

In Fig. 9.5, we present results for the z-component $\langle \bar{T}_z^* \rangle$ of the averaged torque $\langle \bar{\mathbf{T}}^* \rangle$ for systems with different dipolar coupling strengths $\lambda = \mu^{*2}/T^*$ at $B_x^+ = 0.5$, $T^* = 1$ and $B_x^+ = 0.1$, $T^* = 0.2$. At $\lambda = 0$, the particles interact with each other via the soft-sphere interaction but not via the dipole-dipole interaction. Note that pure soft-sphere interactions do not affect particle rotations, and thus they should not influence the ratchet effect. Therefore the net torque found at $\lambda = 0$ for the $T^* = 0.2$ system equals the one shown in Fig. 9.3 for $\delta = 0$.

Starting from the non-interacting system, the net torque plotted in Fig. 9.5 increases up to

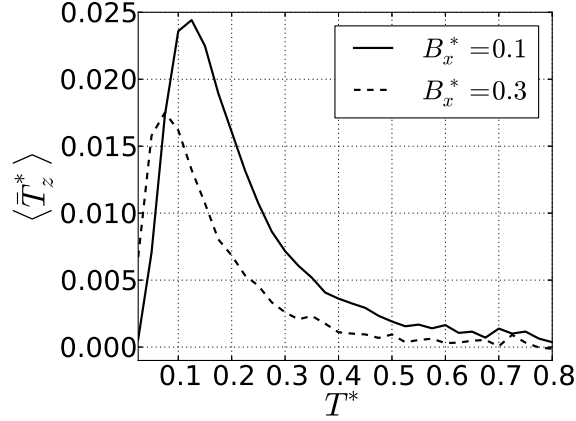


Figure 9.4.: The net torque as function of the temperature for $B_x^* = 0.1, 0.3$ and $\delta = 0$.

$\lambda \approx 1.5$ ($T^* = 1$) or $\lambda \approx 2.5$ ($T^* = 0.2$), respectively. In the high temperature system, the maximum of $\langle \bar{T}_z^* \rangle$ is approximately 30% larger than the torque at $\lambda = 0$. For $T^* = 0.2$ the maximum is even more pronounced: The torque is increased by nearly 40% compared to the non-interacting system. For higher values of λ , $\langle \bar{T}_z^* \rangle$ decreases continuously.

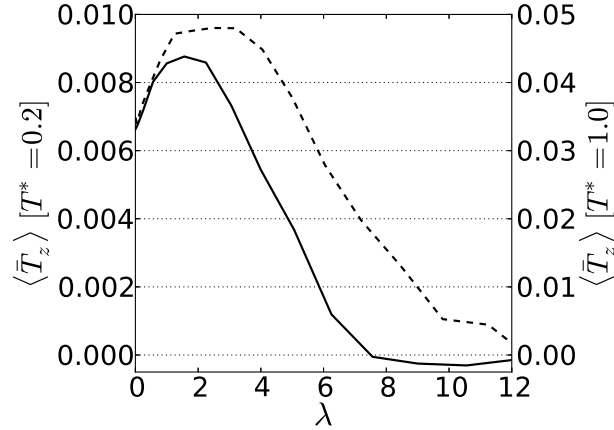


Figure 9.5.: The z-component $\langle \bar{T}_z^* \rangle$ of the averaged torque for different coupling strengths λ at $T^* = 1$, $B_x^+ = 0.5$, $B_y^+ = 5$ (solid line, right axis), and $T^* = 0.2$, $B_x^+ = 0.1$, $B_y^+ = 1$ (dashed line, left axis). As in all the following figures of this chapter, $\rho^* = 0.2$, $\omega\sigma^2/D_0^T = 15$, and $\delta = 0$ were used.

Note that this behavior is consistent with the behavior found in the mean-field investigation in Ref. [163]. In that study, the authors considered particles that experience a (mean-field) torque of the form

$$\mathbf{T}_i^{\text{mf}} = \mathbf{e}_i \times \frac{K}{N} \sum_{i=1, j \neq i}^N \mathbf{e}_j, \quad (9.11)$$

where K is the mean-field coupling strength. For non-vanishing values of K , an increase in the

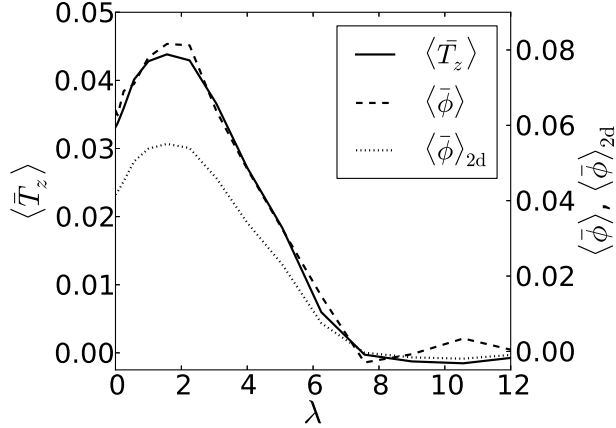


Figure 9.6.: The net torque $\langle \bar{T}_z^* \rangle$, the mean traversed angle $\langle \bar{\phi} \rangle$, and the mean traversed angle $\langle \bar{\phi} \rangle_{2d}$ calculated from the torque [see Eq. (9.13)] are shown for $T^* = 1$ and $B_x^+ = 0.5$.

ratchet effect was discovered [163], which agrees with our observations.

The behavior of $\langle \bar{T}_z \rangle$ in Fig. 9.5 is also reflected by the change in the (system-averaged) polar angle ϕ

$$\langle \bar{\phi} \rangle = \bar{\phi}(t + \tau) - \bar{\phi}(t) \quad (9.12)$$

during one rotational period of the field. As shown in Fig. 9.6, $\langle \bar{\phi} \rangle$ and $\langle \bar{T}_z^* \rangle$ behave almost identically, which can be understood by looking at the BD evolution equation (4.37). Assuming the rotational motion of the particles to be restricted to the plane of the field (denoted by the subscript “2d”) and neglecting the random noise, we find

$$\langle \bar{\phi} \rangle_{2d} = \frac{\tau D_0^R}{k_B T} \langle \bar{T}_z \rangle_{2d} \quad (9.13)$$

from integrating both sides of Eq. (4.37) over one period of the field. This equation relates the traversed angle of the particles to the average torque. The dotted line in Fig. 9.6 demonstrates this relation. We calculated the traversed angle via Eq. (9.13) from the torque component $\langle \bar{T}_z \rangle$. It is seen that this equation slightly underestimates the observed value of $\langle \bar{\phi} \rangle$, which can be explained by the fact that Eq. (9.13) holds strictly only for particle rotations in the plane of the field. Additionally, we neglected the random noise, which is expected to introduce further deviations from the observed relation. Nonetheless, Eq. (9.13) predicts a change in the traversed angle close to the observed one.

We now discuss the origin of the maximum in Figs. 9.5 and 9.6. The initial increase in strength of the ratchet effect for increasing values of λ can be understood by considering the average effective field

$$\mathbf{B}^{\text{eff}} = \mathbf{B}^{\text{ext}} + \frac{1}{M} \sum_{i=1}^M \sum_{j \neq i} \mathbf{B}_{ij}^{\text{dip}} \quad (9.14)$$

felt by the particles, where M is the number of particles considered and

$$\mathbf{B}_{ij}^{\text{dip}} = \frac{3\mathbf{r}_{ij}(\mathbf{r}_{ij} \cdot \boldsymbol{\mu}_j)}{r^5} - \frac{\boldsymbol{\mu}_j}{r^3}. \quad (9.15)$$

This effective field is depicted in Fig. 9.7 for particles with $\lambda = 1.44$, $T^* = 1$ and $\lambda = 2.45$, $T^* = 0.2$. These temperatures and coupling strengths roughly correspond to the maxima in the net torque and the averaged traversed angle [see Fig. 9.5]. The plots in Fig. 9.7 show that, due to the dipolar interactions, the effective field components $B_x^{\text{eff}*}$ and $B_y^{\text{eff}*}$ are increased as compared to the components of the external field. The fact that an enhancement of the (effective) field acting on the particles can support the ratchet effect, is already suggested by our results for a non-interacting system in Sec. 9.3: As shown in Figs. 9.3 and 9.4, an increase in B_x alone or in both, B_x and B_y , can lead to larger values of the net torque.

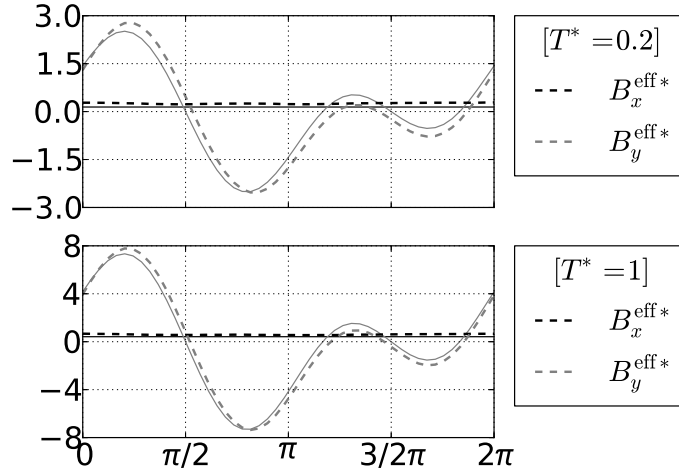


Figure 9.7.: Mean values of the x - and y -components of the averaged effective field $\mathbf{B}^{\text{eff}*}$ over one rotational period of the field at $\lambda = 2.45$, $T^* = 0.2$, and $B_x^+ = 0.1$ (top) and $\lambda = 1.44$, $T^* = 1$, and $B_x^+ = 0.5$ (bottom). The solid lines represent the respective external fields, i.e., $B_x^+ = 0.1$, $B_y^+ = 1$ (top); $B_x^+ = 0.5$, $B_y^+ = 5$ (bottom)

For coupling strengths higher than $\lambda \approx 1.5$ ($T^* = 1$) or $\lambda \approx 2.5$ ($T^* = 0.2$), respectively, the magnitude of the ratchet effect (as measured by $\langle \bar{T}_z^* \rangle$) begins to decrease. We relate this behavior to the increase of the ratio of conservative torques induced by the dipolar interactions and the external field relative to the strength of the noise. However, in contrast to the (corresponding) decrease described in Sec. 9.3 [see Fig. 9.4], a large contribution to the torque now stems from the dipole-dipole interaction and not from the particle-field interaction. This can be seen in Fig. 9.8, where we compare the functions $\bar{S}_x(t)$ and $\bar{S}_y(t)$ [cf. Eq. (9.6)] for a system at $\lambda = 1.44$ ($T^* = 1$) and a more strongly coupled one at $\lambda = 9$ ($T^* = 1$). It is seen that \bar{S}_x is significantly larger for the latter system ($\bar{S}_x \approx 0.58$) than for the former one ($\bar{S}_x \approx 0.16$). Recalling the discussion in Sec. 9.3 (non-interacting system), one would thus expect the ratchet effect at $\lambda = 9$ to be even larger than at $\lambda = 1.44$. However, the amplitude of \bar{S}_y is considerably smaller. Indeed, the maximum of $|\bar{S}_y|$ for the strongly coupled system is about 0.31, while it is about 0.72 for the one with $\lambda = 1.44$.

This means that the particles at $\lambda = 9$ are much more aligned along the x -direction (i.e., the constant part of the field) without closely following the oscillations in y -direction. In conclusion, the behavior seen at $\lambda = 9$ is in stark contrast to what is shown in Fig. 9.1 for a non-interacting system. There, an increase in B_x^* does not automatically damp out the oscillations in the y -

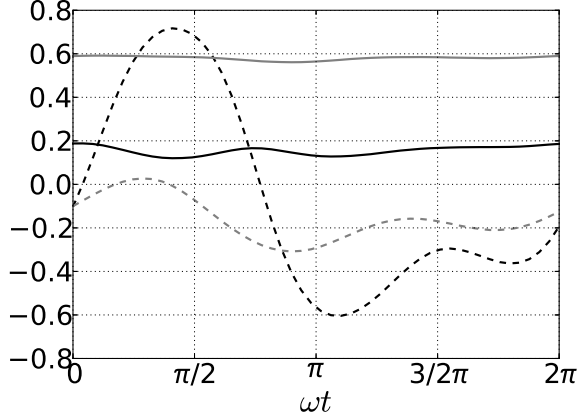


Figure 9.8.: Mean orientation of the particles during one rotational period of the field for $\lambda = 1.44$ (black lines) and $\lambda = 9$ (gray lines) at $T^* = 1$ and $B_x^+ = 0.5$. The x - and y -components of $\bar{\mathbf{S}}$ are indicated by the solid and dashed lines, respectively.

direction. Consequently, the ratchet effect is increased rather than damped.

Finally, we note that, for relevant values of λ , the relative increase in the net torque is larger for the low-temperature system than for the high-temperature one. Indeed, Fig. 9.5 shows that the value of T^* influences the entire behavior of $\langle \bar{T}_z^* \rangle$ as a function of λ . Therefore, not only the dipolar, but also the short-range repulsive interactions between the particles have an impact on the ratchet effect.

The sensitivity against T^* can be explained by the fact that the SS interactions affect the effective distance between the dipolar particles. In Fig 9.9(a), the radial distribution functions of two systems at identical coupling strength $\lambda = 4$ but different temperatures ($T^* = 1$ and 0.2) are shown. Judging from the position of the main peak, two neighbors are typically closer to one another in the $T^* = 1$ system than in the low temperature one. As a result the particles experience a considerably stronger effective field in the high-temperature system. This is illustrated by Fig. 9.9(b), where we plot the function

$$b(r) = \frac{1}{S_r} \int_{S_r} dS \frac{1}{N} \left\langle \sum_{i=1}^N \sum_{j \neq i} \delta(\mathbf{r} - \mathbf{r}_{ij}) B_{x,ij}^{\text{dip}} \right\rangle, \quad (9.16)$$

where S_r is the surface of a sphere of radius r . From a physical point of view, the function $b(r)$ corresponds to the local field in x -direction that is generated by neighboring dipolar particles with distance r^* from the central one. From Fig. 9.9(b), we see that the local field at short distances is significantly increased in the $T^* = 1$ system as compared to the field in the $T^* = 0.2$ system. Hence, as argued above, the rotational motion is much more restricted in the former system resulting in a less pronounced ratchet effect at a fixed coupling strength.

Additional test simulations indicate that we can generally expect a relative increase of the ratchet effect when T^* is decreased.

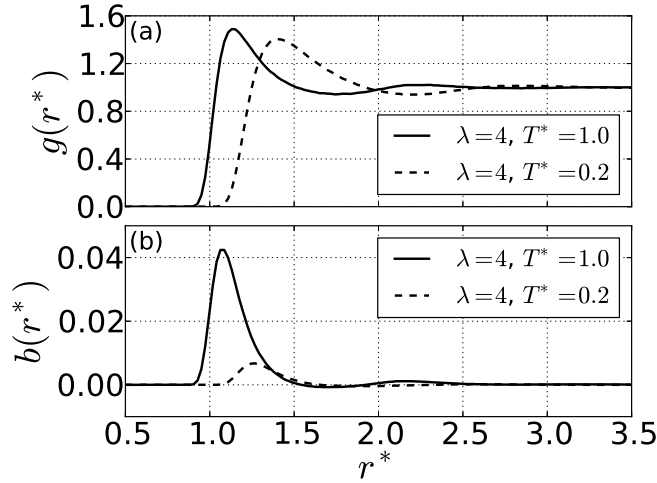


Figure 9.9.: (a) Pair correlation functions of systems ($B_x^+ = 0.5, 0.1$) at different temperatures ($T^* = 1, 0.2$) but identical dipolar coupling strengths λ . (b) The local field $b(r)$ [see Eq. (9.16)] for the two different systems.

9.5. Relation to self-assembly

It is well established that strongly coupled dipolar particles can self-assemble into a variety of structures including chains, networks, and sheets [20, 38]. Moreover, for dense systems of dipolar spheres, theory and computer simulations predict a phase with spontaneous long-range, parallel (i.e., ferromagnetic) order [169]. It is therefore an interesting question whether these phenomena have any relevance in the context of the rotational ratchet effect.

The answer from our present BD simulations is essentially negative. Indeed, at the conditions where we found an increase in the ratchet effect ($T^* = 1, 0 \lesssim \lambda \lesssim 3.5$; $T^* = 0.2, 0 \lesssim \lambda \lesssim 5.5$) there is no global parallel order. Moreover, significant local ordering of the particles only occurs for dipolar coupling strengths $\lambda \gtrsim 9$ ($T^* = 1$), which is outside of the range where we observe enhancement of the ratchet effect. The structures seen in such a highly coupled systems are illustrated by the simulation snapshot in Fig. 9.10. Similar to ferrofluids subject to constant, homogeneous external fields, the oscillating field favors chain formation of the particles. Systems of lower coupling strength lack any such order. In particular, no local order can be observed at $\lambda = 1.44, T^* = 1$, i.e., where the ratchet effect is maximal.

Another interesting aspect is the (possible) impact of the ferromagnetic phase transition occurring at higher densities. In Ref. [163], this question was investigated on a mean-field level [cf. Eq. (9.11)]. For sufficiently large coupling strengths K , one finds a spontaneous ferromagnetic ordering of the particles resulting in an effective non-vanishing field component in x -direction [163]. Due to this net field, the ratchet effect can occur even in the absence of an external x -component of the field.

We have searched for a similar phenomenon in our many-particle system. However, at the parameters considered, we were not able to find a net particle rotation. Not even at high densities, where the DSSs undergo a ferromagnetic phase transition [169], did we detect such a rotation.

This could be due to several reasons: First, the true effective field within the ferromagnetic

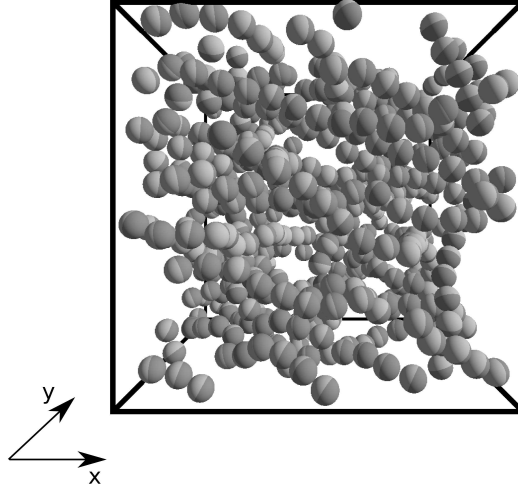


Figure 9.10.: Snapshot of a system at $\lambda = 9$, $T^* = 1$, and $B_x^+ = 0.5$.

phase is inhomogeneous and typically much weaker than any average “mean-field” (this is also the reason that the isotropic-ferromagnetic transition in a true dipolar system occurs at much larger coupling strengths than those predicted by mean-field theory [163, 169]).

Second, in a dense dipolar system, the orientations of the particles are strongly coupled over large distances. In other words, the dipole orientations are severely restricted, which further suppresses the ratchet effect.

Finally, note that test simulations seem to indicate the net torque to increase with increasing density [$0.05 \leq \rho^* \leq 0.5$, see Fig. 9.11]. We speculate that this density-induced increase is due to the increasing number of neighbors around a particle, which, in turn, could enhance the local effective field (similar to the coupling strength-induced mechanism discussed in Sec. 9.4).

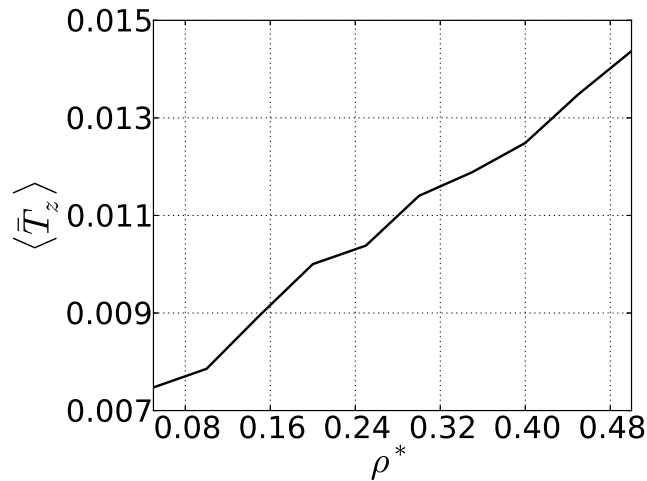


Figure 9.11.: Net torque over density for a system at $T^* = 0.2$, $\mu^* = 0.7$, and $B_x^+ = 0.1$.

9.6. Conclusions

In this chapter, we have investigated the rotational thermal ratchet effect for non-interacting particles as well as particles interacting via long-range dipolar interactions.

With our particle based simulations, we looked at the angular trajectories of the dipolar particles, which conclusively illustrate the net rotating behavior of the driven particles. For non-interacting particles, we found that a finite ratio of deterministic torques to random noise yields a maximally pronounced ratchet effect.

The main focus of this chapter, however, was the investigation of the influence of dipolar interactions on the rotational behavior of the particles. In particular, we showed that dipolar interactions can have an enhancing as well as a dampening effect depending on the dipolar coupling strength λ . The enhancement found at small values of λ is due to the fact that the effective field acting on a particle is larger (than without interactions), but not too large to suppress rotations. This finding is consistent with the mechanism found in Ref. [163].

However, it would be difficult to directly compare these two results, since the prediction from [163] is based on particles interacting via a mean-field interaction. This causes two problems. First, density is irrelevant in the mean-field theory. In our simulations, however, it is expected to play a role. Closely related to this is the second point: The mean-field interaction is not distance dependent, which means that the coupling parameter used in [163] cannot be easily compared to the dipolar coupling strength used in this thesis.

Interestingly, we were not able to attribute the increase in the ratchet effect in systems of dipoles to a synchronization phenomenon, i.e., a coupled rotation of two neighboring dipolar particles. It is, however, possible that such synchronization phenomena occur at thermodynamic and field parameters that differ from the ones investigated here.

At higher values of λ , i.e., stronger dipolar couplings, we find a decrease in the ratchet effect. In this region, the particles start to aggregate into clusters along the direction determined by the constant contribution to the external field. As a consequence, the effective field becomes too strong and the dipole moments can follow the oscillatory motion of the field less and less, leading to a pronounced dampening of any rotations. We note that the values of λ considered in this chapter are in the range typical for real ferrofluids (as are the considered densities).

As a somewhat counterintuitive effect, we have found that not only the anisotropic dipolar interactions but also the isotropic repulsive interactions between the particles have a significant influence on the ratchet effect. At constant dipolar coupling strength, the steepness of these interactions determines the average distance between the particles and thus, the magnitude of the effective local field. In this way, short-range interactions can “tune” the effective torque.

One interesting remaining question concerns the influence of the driving frequency on the ratchet effect. This influence has already been investigated experimentally [164] as well as theoretically [47]. However, the theoretical predictions seem to conflict with the experimental data. In the experiment, the net torque saturates at high frequencies, the reason for which yet remains to be understood.

In summary our results show that the conservative interactions typical of real ferrofluids strongly influence noise-induced phenomena such as the ratchet effect. So far, we have not taken into account the fact that the solvent, which is omnipresent in a ferrofluid, induces additional hydrodynamic interactions between the magnetic particles. These long-range interactions have been shown to be able to play a significant role in translational ratchets (see, e.g., Refs. [52, 53]) and related synchronization phenomena [54].

10. Summary

In this thesis, we have discussed the nonequilibrium dynamic and pattern formation behavior of dipolar particles that are driven by external time-dependent fields. Here, in this chapter, we will summarize the key results of our investigations.

First, we focused on dipolar particles that are exposed to external rotating fields in three-dimensional bulk geometries. This setup causes the particles to aggregate into layers for suitable thermodynamic and field parameters. The reason for this behavior is a synchronized rotation of the particles with the field: It results in an emerging effective interparticle interaction that is attractive within the plane of the field and repulsive otherwise. Upon loss of synchronization, the layered structures disappear.

To understand the layer formation in detail, we constructed a nonequilibrium diagram illustrating the regions of layer formation in the field strength-frequency domain. Within this diagram, we investigated the rotational dynamic behavior of the particles in the layered and unlayered regions. By understanding the dynamics in these two different regions, we were able to explain the breakdown of layer formation with an effective single particle theory. Specifically, we found the breakdown of synchronization, and, consequently, layer formation, to essentially be a friction induced effect.

Further, given synchronization, we asked whether synchronized motion automatically leads to layering. By performing density functional calculations of a system interacting via a time-averaged, effective interparticle potential, we were able to show that there exists a phase transition from a homogeneous state into a layered one in this system (in the density functional theory). The transition is caused by the effective potential overcoming the entropy cost associated with the formation of layers.

An important question in colloidal systems regards the influence of the solvent on the behavior of the immersed particles. We showed layer formation to be stable under the inclusion of hydrodynamic interactions, even though they seem to cause the layers to disappear at lower frequencies. The rotational behavior of the particles, however, does not seem to be significantly affected by the solvent-mediated interactions.

The second major investigation presented in this thesis revolves around the behavior of dipolar colloids in quasi-two-dimensional geometries that are exposed to in-plane rotating fields. As in the three-dimensional case, the driven particles perform a synchronized rotation for suitable thermodynamic and field parameters. This synchronization results in an effective interaction as described above. Since the particles are confined to a single layer which agrees with the plane of the field the effective potential is attractive and isotropic. These properties of the potential can cause the formation of clusters that extend into two dimensions.

We systematically investigated regions of synchronization, cluster formation, and non-synchronized motion depending on the field parameters. Compared to layer formation in three dimensions, higher driving frequencies are required for the two-dimensional cluster formation to occur.

For these two-dimensional systems, the question of the influence of hydrodynamic interactions on the behavior of the particles is also an important one to ask. We found that cluster formation occurs despite the presence of solvent-mediated interactions. However, as in three dimensions,

structures stop forming at smaller frequencies than in the not hydrodynamically interacting system. Moreover, the hydrodynamic interactions accelerate the clustering process and cause a collective cluster rotation.

We also uncovered a first-order phase transition between a vapor and a condensed phase in a system interacting via the time-averaged dipolar interactions. Investigating the domain growth behavior of this system as well as the one of the driven system showed the growth to progress identically in both cases and with a power law behavior. The power law behavior agrees with the one seen in many systems undergoing spinodal demixing. From this and the fact that clustering was observed in the coexistence region only, we concluded the clustering process to correspond to spinodal decomposition within the coexistence region of the phase transition.

Having understood the clustering behavior, we briefly [see Appendix A] turned to a system consisting of a setup with characteristics of both the previously investigated geometries and field alignments. More precisely, we looked into the structure formation behavior of quasi-two-dimensional systems exposed to out-of-plane fields. For sufficiently high field strengths, in a process similar to the one observed in the driven three-dimensional system, these systems can form one-dimensional “layers” in the plane of the field.

By making use of density functional calculations we showed the existence of a phase transition into a “layered” state. In contrast to the three-dimensional layer formation, a considerably higher dipolar coupling strength is required for patterns to emerge.

The last major investigation presented in this thesis is centered on the rotational ratchet effect. In general, ratchet effects are characterized by the rectification of random Brownian noise into directional motion in far out of equilibrium systems. The rotational ratchet effect, specifically, can be observed in systems that are driven by an oscillating field lacking a net rotating component. Despite this lack, a net transfer of torque from the field to the particles, and, hence, a directed rotation of the particles, can take place.

Our investigation of the rotational ratchet effect in systems of dipolar particles yielded two main results: First, we showed dipolar interactions to be able to enhance as well as suppress the rotational ratchet effect. Enhancement occurs due to an increase in the effective field felt by the particles while the suppression happens due to a decrease in freedom in their rotational motion. Second, we uncovered the influence of the short-range repulsive interactions. By affecting the effective distance between the particles, they change the effective local field (caused by the dipoles) felt by the particles. The larger the distances that are prescribed by the short-range interaction, the larger the possible enhancement of the ratchet effect.

These results conclude the main part of this thesis. The author of this thesis was involved in further projects, the results of which are not presented in the principal part of the thesis. However, the contributions to these projects are summarized in the Appendices B and C.

11. Outlook

Suspensions of dipolar colloidal particles are very complex systems, which give rise to a myriad of interesting pattern formation and many-particle effects. Responsible for these phenomena is in many cases the interplay between a particle-field interaction and the anisotropic particle-particle interaction.

In this thesis we have focused on two kinds of external fields in dipolar systems: We investigated the effects of rotating fields and the effects of oscillating fields lacking a net rotating component. While these fields allow intriguing phenomena to emerge, they are clearly not the only interesting ones to consider. For instance, the effects of triaxial fields or general oscillating fields are still poorly understood. In particular triaxial fields seem to give rise to complex phenomena such as the formation of honeycomb-like structures.

Dipolar interactions are strongly anisotropic, which is the root of many of the pattern formation phenomena described in this thesis. Similar to different choices of the external field, different anisotropic particle interactions, such as, e.g., quadrupolar ones, still remain to be studied. As is the case for dipoles, an investigation of these interactions might pave the way to the discovery of new materials with unexpected properties.

In this thesis, we have seen that not only the anisotropic interactions play a significant role in the dynamic behavior of the particles. The short-range, isotropic interaction can also have a crucial influence on the behavior of colloidal systems. A deeper investigation of the impact of this interaction on the dynamics and the pattern formation in the layering and clustering phenomena might yield surprising results. For example, we expect the structures at low driving frequencies of the field to be considerably affected due to the changes in the effective anisotropy of the particle interactions.

An important point in this thesis concerns the influence of hydrodynamic interactions on the layering and the clustering effect. But despite our investigations, some open questions remain. We have seen that the in-cluster structure is influenced by hydrodynamic interactions. However, no such data exists for layer formation, which is very likely to undergo a similar change. But even in the case of cluster formation, in particular at low driving frequencies of the field, more information is required to form a full picture of the effects of hydrodynamic interactions on the arrangement of the particles.

A specific consequence of hydrodynamic interactions is a premature breakdown of layer and cluster formation at high frequencies. This breakdown seems, at least partially, to be caused by additional translational motion in the systems stemming from the hydrodynamic flow fields. However, the extent of the influence of this motion is not yet quantitatively understood.

While the influence of hydrodynamic interactions on the layering and clustering phenomena has been studied in this thesis, similar results for the rotational ratchet effect have not been presented. However, it has been shown in recent studies that hydrodynamic interactions between colloids can lead to rotational synchronization. Such a phenomenon could give rise to a completely new mechanism that causes rotations of the particles in dipolar ratchet systems and could strongly enhance the magnitude of the effect. For this reason, an investigation of the effects of a solvent on the ratchet behavior might be very enlightening and helpful for applications.

The focal points of this thesis were the pattern formation and dynamics of dipolar colloidal systems. Both of these can be very useful to experimentalists and material scientists. However, while we have investigated the patterns and the associated dynamic behavior, we have not studied quantities such as the thermal conductivity or the viscosity. Finding out more about these properties could help shed more light on how the self-organized materials investigated here can be utilized in material science.

The results of the current work, are, however, not only useful in the context of material science. Indeed, they contribute to the more general field of nonequilibrium physics. In a variety of contexts, most notably in biological systems, nonequilibrium phenomena play a key role. Active Brownian swimmers, characterized by their self-propelled motion through a solvent, are prime examples of such systems. Despite the differences between these swimmers and the dipolar particles considered in this thesis, similar phenomena can be observed: For instance, clustering and spinodal decomposition are processes that can occur in both systems. At a second glance, this is not really surprising: The major ingredients of these active media are also present in our colloidal suspensions. The particles are driven by an external field causing motion and they interact via a (effective) potential which can result in directional preferences.

At last, we would like to refer the reader to the conclusion sections of Chs. 7, 8, and 9. Open questions specific to the systems considered in these chapters are discussed there.

Acknowledgments

First and foremost, I want to thank Prof. Dr. Sabine Klapp for introducing me to the fascinating field of complex fluids and computer simulations and for giving me the opportunity to work on this exiting and challenging topic. Thanks to her constant support, great mentoring, and invaluable input I learned a lot about physics and science in general.

Also, I would like to thank Prof. Dr. Roland Netz for taking the time to grade this work.

For providing the reference data that was used in the investigation of the ratchet effect, I would like to thank Prof. Dr. Andreas Engel.

For the fruitful and interesting collaborations, I want to thank Heiko Schmidle and Jelena Jordanovic.

My thanks also goes to the entire research training group RTG 1558 *Nonequilibrium Collective Dynamics in Condensed Matter and Biological Systems*. The organizers and the other PhD students created a great atmosphere to work in.

Further, I would like to thank the members of Prof. Dr. Klapp's work group. In particular Heiko, Anton, and Ken helped me with many enlightening discussions. Moreover, Ken was the best office companion I could have ever hoped for.

At last I want to thank my parents. Their unwavering support in every conceivable way helped me to get to this point in my life. Without them, this thesis would have never even been started.

Appendices

A. Pattern formation of dipolar colloids driven by out-of-plane fields in two dimensions

In this chapter, we want to consider a physical setup that resembles the one described in Ch. 8. However, here we look at the behavior of dipolar particles dispersed on a monolayer that are exposed to out-of-plane rotating external fields. As compared to Ch. 8, this tilt of the external field fundamentally changes the effective particle interactions. Instead of being purely attractive, the potential is repulsive in the direction perpendicular to the field and attractive in the plane of the field if the particles perform a synchronized rotation. Consequently, we do not expect to observe the formation of two-dimensional clusters as described in Ch. 8, but rather the formation of structures that are in line with the layer formation investigated in Ch. 7.

The main focus of this chapter is the pattern formation behavior of the dipolar particles. The dynamical properties of the particles are very similar to the ones described in Chs. 7 and 8.

A.1. Model and simulation methods

We again model the particles by DSSs [see Sec. 3.7] in our LD simulations [Sec. 4.2]. In these simulations, we use the friction coefficients ($\xi_T^* = 13.5$, $\xi_R^* = 0.45$), moment of inertia ($I^* = 0.0025$), and time step ($\Delta t^* = 0.0025$) that have been used in Chs. 7 and 8. Further, the simulation boxes contain 900 particles.

The particles are confined to a quasi-two-dimensional geometry. Hence, the translational motion of the particles is restricted to the $x - y$ -plane modeling a monolayer. Rotational motion, however, is possible into all the spatial directions. While the monolayer lies within the $x - y$ -plane, the external field rotates in the $y - z$ -plane, i.e.,

$$\mathbf{B}^{\text{ext}}(t) = B_0(\mathbf{e}_y \cos \omega_0 t + \mathbf{e}_z \sin \omega_0 t). \quad (\text{A.1})$$

Thus, the field performs a rotation perpendicular to the plane the particles are confined to.

The LD simulations that we use here are carried out as in the Ch. 8: We integrate the equations of motion with a leapfrog algorithm [see Sec. 4.1.1] and use the quasi-two-dimensional dipolar Ewald sum to calculate the dipolar interactions between the particles [cf. Sec. 5.3].

A.2. One-dimensional layer formation

In Fig. A.1(a), a system ($\rho\sigma^2 = 0.35$, $T^* = 1.35$) in zero field at a very high dipolar coupling strength ($\mu^* = 6.1$, $\lambda = \mu^{2^*}/T^* \approx 27.6$) is shown. Very pronounced ring and chain formation can be observed. Exposing this system to an external rotating field of suitable frequency and strength results in the formation of one-dimensional “layers” in the plane of the field as depicted in Fig. A.1(b). This situation is very similar to the one discussed in Ch. 7. The synchronized

particles interact via [cf. Eq. (7.5)]

$$U^{\text{ID}}(\mathbf{r}_{ij}) = -\mu^2 \frac{(1 - 3 \cos^2 \Theta_{ij})}{2r_{ij}^3}, \quad (\text{A.2})$$

where Θ_{ij} is the angle between the normal to the plane of the field and the vector \mathbf{r}_{ij} . Hence, the particles attract each other in the plane of the field (i.e., if $|\cos^2 \Theta_{ij}| < 1/3$) and repulse each other otherwise.

Note that the dipole strength of the systems shown in Fig. A.1 is considerably larger than the ones used in the investigation of the layer formation phenomenon in three dimensions. We will discuss this point later.

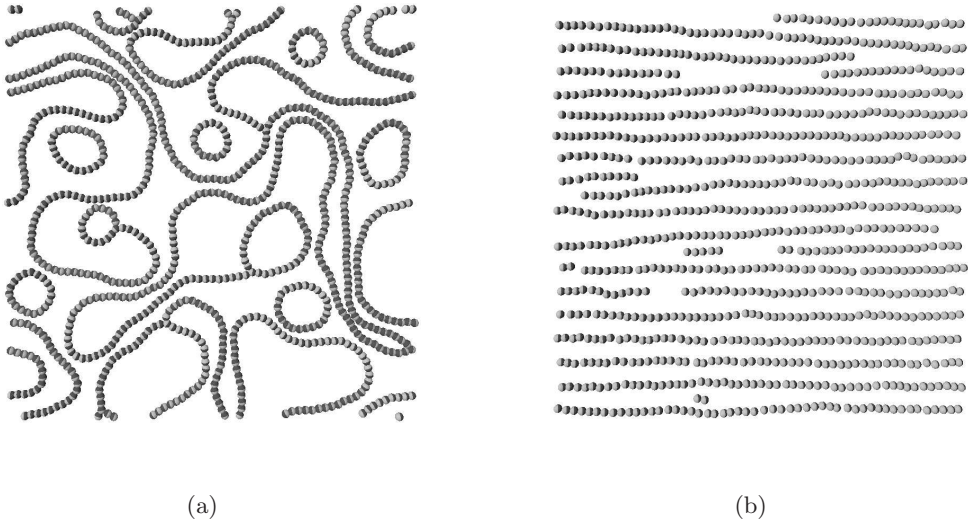


Figure A.1.: (a) Snapshot of a system in zero field at $\rho^* = 0.35$, $T^* = 1.35$, and $\mu^* = 6.1$. (b) Snapshot of a system in a layered state at the same thermodynamic parameters as (a). The strength and frequency of the field are $B_0^* = 150$ and $\omega_0^* = 50$, respectively.

A.3. Density functional approach to one-dimensional layering in a synchronized system

Given synchronous rotation, we ask here for which dipole strengths and densities the particles arrange themselves into one-dimensional layered structures. In order to answer this question, we again turn to density functional methods [cf. Secs. 6.2 and 7.7]. Due to the assumption of synchronized rotation, we consider the particles as interacting via the effective potential (A.2), in which case we can calculate the perturbation expansion of the free energy up to second order in the density [cf. Sec. 6.2.2] in two spatial dimensions:

$$\begin{aligned} \frac{\Delta \mathcal{F}}{A} = & \frac{1}{\beta A} \int_A d^2 r [\log(\Lambda^2 \rho(\mathbf{r})) - 1] - \frac{1}{\beta A} \int_A d^2 r \rho_0 [\log(\Lambda^2 \rho_0) - 1] \\ & - \frac{1}{2\beta A} \int_A d^2 r_1 \int_{\mathbb{R}^2} d^2 r_2 c(\mathbf{r}_1 - \mathbf{r}_2) \Delta \rho(\mathbf{r}_1) \Delta \rho(\mathbf{r}_2) \quad (\text{A.3}) \end{aligned}$$

In Eq. (A.3), $\Delta\rho(\mathbf{r}) = \rho(\mathbf{r}) - \rho_0$ with $\int_A d^2r \Delta\rho(\mathbf{r}) = 0$, Λ is the thermal wavelength, and c is the direct correlation function of the homogeneous system.

To approximate the direct correlation function, we employ the RPA [cf. Sec. 6.2.3], which amounts to setting

$$c(\mathbf{r}) = \begin{cases} c_{2d}^{\text{PY}}(r), & r \leq \sigma \\ -\beta U^{\text{ID}}(\mathbf{r}), & r > \sigma. \end{cases} \quad (\text{A.4})$$

In contrast to the three-dimensional case [see Sec. 7.7], we consider the reference system to consist of HDs instead of HSS [cf. Sec. 6.2.3]. Hence, c_{2d}^{PY} is given by Eq. (6.26) instead of Eq. (6.23).

Similar to the ansatz for the density profile used in Sec. 7.7, we use

$$\rho(\mathbf{r}) = \rho(x) = \rho_0 + \tilde{\rho} \cos(kx). \quad (\text{A.5})$$

Using this ansatz in Eq. (6.5), we find

$$\frac{\Delta\mathcal{F}}{H} = \frac{1}{\beta} \int_0^{\lambda_L} dx \rho(x) \log\left(\frac{\rho(x)}{\rho_0}\right) - \lambda_L \frac{\tilde{\rho}^2}{4\beta} \tilde{c}(k). \quad (\text{A.6})$$

Here, $\Delta\mathcal{F}$ is the free energy of the area $A = H \cdot \lambda_L$ as compared to the homogeneous system, H is a length in the y -direction and $\lambda_L = 2\pi/k$, and \tilde{c} is again the Fourier transform of c with $\tilde{c}(k) \equiv \tilde{c}(k\mathbf{e}_x)$.

From Eq. (A.6), we can calculate the free energies at different thermodynamic parameters. In contrast to the three-dimensional case discussed in Sec. 7.7, the free energy possesses a well defined minimum at finite values of k . Consequently, no distance between the ‘‘layers’’ has to be prescribed. As in Sec. 7.7, we find the DFT to predict the system to undergo a phase transition into a layered state.

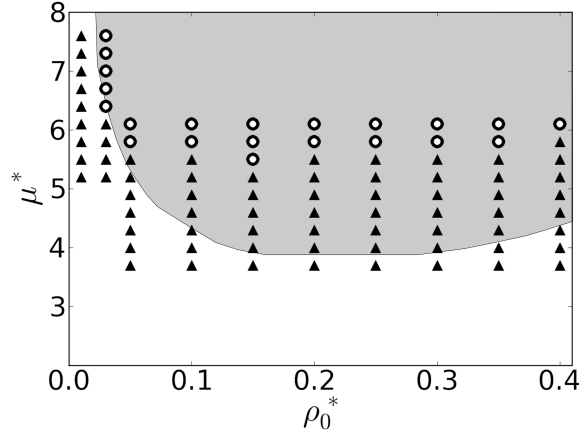


Figure A.2.: Equilibrium phase diagram of a perfectly synchronized system. The gray area indicates the stability range of the layered state according to our DFT calculations. Also shown are LD results (at $\omega_0^* = 50, B_0^* = 50$) with the open circles (solid triangles) representing layered (non-layered) states.

Fig. A.2 shows the results of the numerical evaluation of Eq. (A.6). The gray area indicates where layer formation depending on the dipole moment and density was found. Also shown

in Fig. A.2 are LD simulation results. Both the simulation and the DFT results predict a rise in the necessary dipole strength for “layer” formation at decreasing density. However, in the simulations, comparatively higher dipole moments are required for the structures to appear. Responsible for this difference are the approximations that were made to calculate the free energies. We only consider a perturbation expansion of the free energy, approximate the direct correlation function, and impose a density profile.

A.4. Conclusion

In this chapter, we have considered a system of dipolar particles in a quasi-two-dimensional geometry driven by an out-of-plane rotating field. For suitable thermodynamic and field parameters, the particles arrange themselves into layer-like structures in the plane of the field. Due to the geometric restrictions, the “layers” extend only into one spatial dimension.

As in the three-dimensional case, the system undergoes a phase transition into a “layered” state in our DFT. Compared to layer formation in three dimensions, higher dipole-moments, i.e., dipolar coupling strengths are required for structures to emerge in the present two-dimensional system. Intuitively, this can be understood by realizing that the lack of particles in the second in-field dimension implies that the attraction and repulsion of one “layer” is smaller than the one of a layer in three dimensions at a given dipolar coupling strength.

B. Crossover from Normal to Anomalous Diffusion in Systems of Field-Aligned Dipolar Particles

In the publication “Crossover from Normal to Anomalous Diffusion in Systems of Field-Aligned Dipolar Particles” [20], we investigated the translational dynamics of dipolar particles in homogeneous and not time-dependent external fields.

The particles of the system exhibit different diffusive regimes depending on the thermodynamic and field parameters. In particular, a subdiffusive regime followed by a superdiffusive one was observed in strongly coupled dipolar systems that are exposed to strong external fields. This behavior can be observed in as well as perpendicular to the field direction. The slowdown of the dynamics, i.e., the subdiffusivity, occurs, since the particles are confined to chains. At longer time scales, however, entire chains of particles move collectively causing the superdiffusive behavior.

In this chapter, we will not discuss the entirety of Ref. [20]. Only the contributions of the author of this thesis to the publication will be summarized. For details we refer the reader to Ref. [20].

B.1. Model and simulation methods

We use LD simulations [cf. Sec. 4.2] with the DSS interaction potential (3.14) to calculate the mean squared displacement

$$\text{MSD}_\gamma(t) = \frac{1}{N} \left\langle \sum_{i=1}^N [\mathbf{r}_{i,\gamma}(t) - \mathbf{r}_{i,\gamma}(0)]^2 \right\rangle \quad (\text{B.1})$$

of the particles parallel ($\gamma = \parallel$) and perpendicular ($\gamma = \perp$) to the external field

$$\mathbf{B}^{\text{ext}}(t) = B_0 \mathbf{e}_x. \quad (\text{B.2})$$

We specialize to the temperature $T^* = 1.35$, the dipole coupling strength $\lambda = \mu^{*2}/T^* = 7$, the field strength $\mu^* B_0^*/T^* = 100$, and the density $\rho^* = 0.05$. As before, we use the Ewald summation method to determine the dipolar interactions [cf. Sec. 5.2]. 864 particles were used in the simulations.

B.2. Dynamic behavior of the particles

We used the LD simulations to understand, to first order, the influence of the presence of a solvent on the dynamic behavior of the system. Specifically, we were interested in the effects of a solvent on the different diffusive regimes.

Clearly, LD simulations do neither explicitly nor implicitly model HIs. However, the friction and random terms in the equations of motion (4.26) and (4.27) of LD can be understood as

modeling a solvent on a single-particle level: The friction terms describe the friction with the solvent and the random contributions correspond to the Brownian kicks stemming from it.

Fig. B.1 shows the MSDs parallel and perpendicular to the field for MD [cf. Sec. 4.1] and LD simulations with different translational diffusion constants D_0^{T*} and fixed rotational diffusion constant $D_0^{R*} = 1$. The rotational diffusion constant was kept fixed, since rotations are not expected to be relevant at the high field strength considered here.

As expected, the simulations reveal an initial ballistic behavior ($\propto t^2$) of the particles both along as well as perpendicular to the field. In the field direction, the dynamics of the particles in the system slows down at intermediate times $t^* = 0.1 - 1$. This slow down is followed by a superdiffusive regime (i.e., $\text{MSD} \propto t^\alpha, \alpha > 1$) at times $t^* = 1 - 10$ for systems with $D_0^{T*} > 1$. At long times the normal diffusion behavior (i.e., $\text{MSD} \propto t$) is recovered.

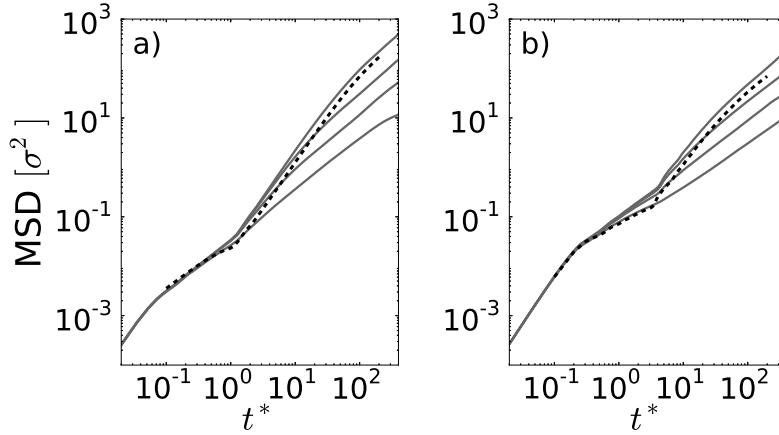


Figure B.1.: MSDs (a) parallel and (b) perpendicular to the field at $T^* = 1.35$, $\lambda = 7$, $\mu^* B_0^*/T^* = 100$ and, $\rho^* = 0.05$. The MSDs from the MD simulations are indicated by the dashed lines. The results from the LD simulations are indicated by the gray lines (from top to bottom: $D_0^{T*} = 50, 10, 3, 1$).

Perpendicular to the field, subdiffusive behavior is observed at all the considered diffusion constants D_0^{T*} in our LD simulations. For $D_0^{T*} \geq 10$, i.e., not too large friction coefficients [cf. Eq. (4.50)], this subdiffusive regime is followed by a superdiffusive one.

These results support the MD observations of Ref. [20]: Despite the inclusion of a first order approximation of a solvent, subdiffusive as well as superdiffusive regimes still exist.

Note that both along as well as perpendicular to the field, the transition from the subdiffusive to the superdiffusive region is less pronounced in the LD simulations than in MD simulations [20]. This smearing of the transitional “kink” might, however, be expected due to the presence of the random and friction terms in the LD equations of motion.

C. Two-dimensional colloidal networks induced by a uni-axial external field

In the publication “Two-dimensional colloidal networks induced by a uni-axial external field” [42], we investigated the experimental system [29] on the basis of Monte Carlo (MC) [58], MD, and LD computer simulations.

The experimental system in [29] consists of colloidal polystyrene particles, which are confined to a plane. Some of the particles have single gold patches covering parts of their surface. These gold patches have an interesting consequence when the colloids are exposed to an oscillating in-plane field of suitable frequency: In addition to the dipole moment induced in the polystyrene particles by the field, an antiparallel dipole moment is induced in the gold patch. These double-dipoles (DID) yield quadrupolar-like interactions, which are markedly different from the usual dipole interactions.

In our publication [42], we investigated a system of spherical particles containing a single or a double-dipole with different computer simulations techniques. We showed that this system exhibits one-dimensional as well as two-dimensional network formation. Moreover, we established the existence of percolation transitions in as well as perpendicular to the field direction and established the existence of gel-like dynamic behavior of the particles.

In this chapter, we will highlight the contributions of the author of this thesis to the paper “Two-dimensional colloidal networks induced by a uni-axial external field”. Specifically, we will discuss the dynamic behavior of the particles, with the central quantity being their mean squared displacement. For details we refer the reader to Ref. [42].

C.1. Model and simulation methods

We used MD as well as LD simulations [cf. Secs. 4.1 and 4.2] to understand the dynamic behavior of the system consisting of single- as well as double-dipoles. The interactions between the different dipole moments in the system were calculated by making use of the Ewald summation method [cf. Sec. 5.3].

Due to their induced nature, the single-dipoles were taken to always point into the field direction. The DIDs were modeled by placing two oppositely oriented dipoles into a particle at a distance of half a particle diameter ($\sigma/2$). In the experiment, the gold patch is either on the right or left hand side of the particle with respect to the external field. To replicate this situation in our simulations, one of the two possible antiparallel configurations was chosen at random for each DID particle.

Instead of using the usual (shifted) SS interaction (3.2) that is proportional to $(\sigma/r)^{12}$ to describe the short-range repulsion, we use a steeper repulsive potential that is proportional to $(\sigma/r)^{28}$. This choice ensures that we remain as close as possible to the MC results in [42], which utilize a hard core interaction.

We used 1024 particles in our simulations, and integrated the equations of motion with a leapfrog algorithm [cf. Sec. 4.1.1].

C.2. Translational dynamics of the particles

Fig. C.1 shows two snapshots of a mixture of dipolar and quadrupolar particles in a quasi-two-dimensional geometry. The ratio of quadrupolar to dipolar particles is $c_{\text{DID}} = 0.25$, the dipole moments are $\mu^* = 1.0$, the temperature of the systems is $T^* = 0.15$ and the densities are $\rho\sigma^2 = 0.25$ and 0.5 , respectively.

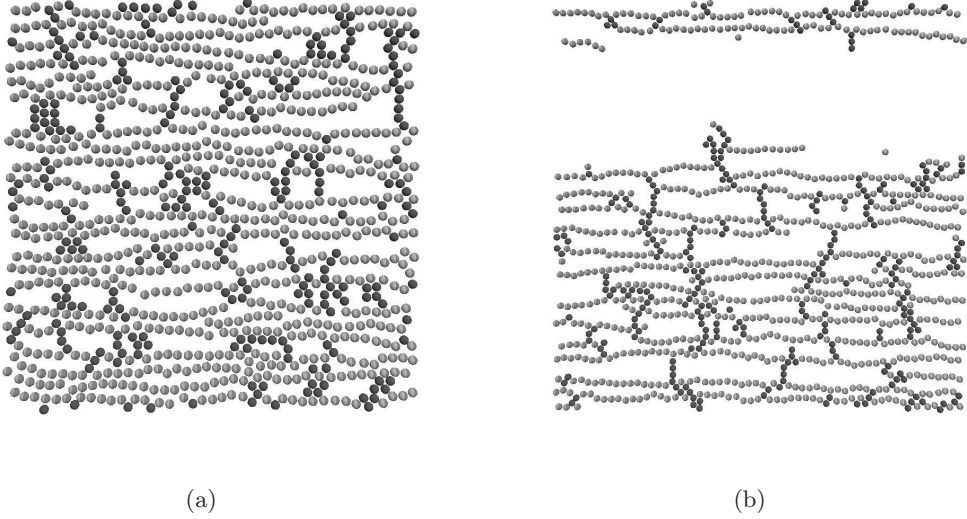


Figure C.1.: MD snapshots of two systems at $c_{\text{DID}} = 0.25$, $\mu^* = 1.0$, and $T^* = 0.15$. The system in (a) has a density of $\rho\sigma^2 = 0.25$, while the system in (b) is of density $\rho\sigma^2 = 0.5$. In both the snapshots, the external field is horizontally aligned.

MD [see Sec. 4.1] results of the mean square displacements (MSDs) parallel and perpendicular to the field [see Eq. (B.1)] are plotted in Fig. C.2. Specifically, we considered systems of density $\rho\sigma^2 = 0.5$ at three different temperatures $T^* = 0.15, 0.3, 0.5$.

It was shown in Ref. [42] that these three different temperatures correspond to different percolation regimes: At $T^* = 0.15$, the system percolates in the field direction as well as perpendicular to the field direction. The former is also true for the $T^* = 0.3$ system, in which percolation parallel to the field can be observed. The high temperature system ($T^* = 0.5$) does not percolate at all.

In our MD simulations, we found MSDs with the typical ballistic behavior ($\propto t^2$) in all the considered systems. At intermediate times, however, the dynamics strongly depend on the temperature. In the $T^* = 0.5$ and $T^* = 0.3$ systems, the MSDs reveal an immediate transition from ballistic to normal diffusive behavior ($\propto t$). The long-time diffusion constants, i.e.,

$$D_\gamma^{\text{T}} = \lim_{t \rightarrow \infty} \frac{1}{2t} \text{MSD}_\gamma(t), \quad (\text{C.1})$$

are somewhat larger along than perpendicular to the field in both cases ($D_\parallel > D_\perp$). However, the dynamics change significantly at $T^* = 0.15$. The MSDs exhibit a pronounced plateau, which is particularly distinctive in the perpendicular direction. The slowing down of the dynamics illustrates that the cross-linking of vertical chains due to the DID particles leads to strongly

hindered translational diffusion. Interestingly, the length scale related to the plateau is in the range $\approx 0.1\sigma$ known from colloidal gels in three dimensions [170,171].

In addition to MD simulations, we performed LD simulations. These were used to estimate the extent to which a solvent might influence the MSD results. We considered different friction coefficients, which were in the range suggested by the MD data. Even for the largest friction coefficients ($\xi_T^* = 50$), the MSDs are still characterized by plateaus [cf. Fig. C.2], suggesting that the hindered dynamics persists in the presence of a medium.

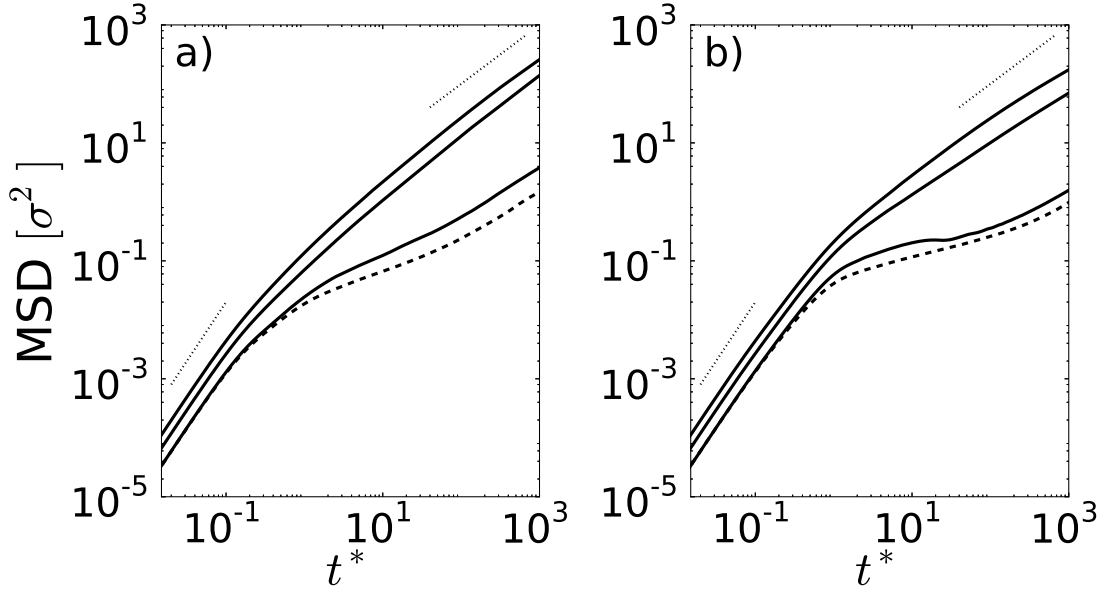


Figure C.2.: MSD (a) parallel and (b) perpendicular to the field as function of time t^* at $\rho\sigma^2 = 0.5$ and $T^* = 0.5, 0.3, 0.15$ (from top to bottom). The dotted straight lines indicate pure ballistic (small t^*) and diffusive behavior (large t^*). The dashed line corresponds to LD simulation results ($T^* = 0.15$, $\xi_T^* = 1.5$).

D. Ewald expressions for the forces and torques in dipolar systems

In the MD, LD, and BD algorithms [cf. Secs. 4.1, 4.2, and 4.3], the forces and torques acting on the particles in the system are necessary ingredients. In this appendix, we present the dipolar Ewald sums for these quantities in different geometries.

D.1. In 3d systems

The forces can be derived from the expression for the energy of the system by using [104]

$$\mathbf{F}_i^{3d} = -\nabla_{\mathbf{r}_i} U_D^{3d}, \quad (\text{D.1})$$

where U_D^{3d} is given by Eq. (5.34). For dipolar particles in three-dimensional bulk systems, we thus find [68, 104]

$$\begin{aligned} \mathbf{F}_i^{3d} = & \sum_{j=1}^N \sum_{\mathbf{n}}' \{ [(\boldsymbol{\mu}_i \cdot \boldsymbol{\mu}_j) \mathbf{r} + \boldsymbol{\mu}_i (\boldsymbol{\mu}_j \cdot \mathbf{r}) + \boldsymbol{\mu}_j (\boldsymbol{\mu}_i \cdot \mathbf{r})] C(|\mathbf{r}_{ij} + \mathbf{n}|) - (\boldsymbol{\mu}_i \cdot \mathbf{r}) (\boldsymbol{\mu}_j \cdot \mathbf{r}) \mathbf{r} D(|\mathbf{r}_{ij} + \mathbf{n}|) \} \\ & + \frac{4\pi}{V} \sum_{\mathbf{k} \neq 0} \frac{1}{k^2} \exp\left(-\frac{k^2}{4\alpha^2}\right) \mathbf{k} (\mathbf{k} \cdot \boldsymbol{\mu}_i) \left[\sin(\mathbf{k} \cdot \mathbf{r}_i) \text{Re} \tilde{M}(\mathbf{k}) - \cos(\mathbf{k} \cdot \mathbf{r}_i) \text{Im} \tilde{M}(\mathbf{k}) \right], \end{aligned} \quad (\text{D.2})$$

where

$$D(r) = \frac{1}{r^7} \left[\frac{2\alpha r}{\sqrt{\pi}} (15 + 10\alpha^2 r^2 + 4\alpha^4 r^4) \exp(-\alpha^2 r^2) + 15 \text{erfc}(\alpha r) \right]. \quad (\text{D.3})$$

Similarly, the torques can be obtained by the relation [58]

$$\mathbf{T}_i = -\boldsymbol{\mu}_i \times \nabla_{\boldsymbol{\mu}_i} U_D^{3d}, \quad (\text{D.4})$$

which yields [68, 104]:

$$\begin{aligned} \mathbf{T}_i^{3d} = & -\boldsymbol{\mu}_i \times \left[-\sum_{j=1}^N \sum_{\mathbf{n}}' [\boldsymbol{\mu}_j B(|\mathbf{r}_{ij} + \mathbf{n}|) + \mathbf{r} (\boldsymbol{\mu}_j \cdot \mathbf{r}) C(|\mathbf{r}_{ij} + \mathbf{n}|)] \right. \\ & \left. + \frac{4\pi}{V} \sum_{\mathbf{k} \neq 0} \frac{1}{k^2} \exp\left(-\frac{k^2}{4\alpha^2}\right) \mathbf{k} \left[\cos(\mathbf{k} \cdot \mathbf{r}_i) \text{Re} \tilde{M}(\mathbf{k}) + \sin(\mathbf{k} \cdot \mathbf{r}_i) \text{Im} \tilde{M}(\mathbf{k}) \right] \right] \end{aligned} \quad (\text{D.5})$$

D.2. In 2d systems

The derivation of the Ewald expressions for the forces and torques in quasi-two-dimensional systems proceeds as in three dimensions [cf. Appendix D.1]. From the Ewald sum for the potential

energy (5.44), we obtain

$$\begin{aligned}
 \mathbf{F}_i^{2d} = & \sum_{j=1}^N \sum_{\mathbf{n}}' \{ [(\boldsymbol{\mu}_i \cdot \boldsymbol{\mu}_j) \mathbf{r} + \boldsymbol{\mu}_i (\boldsymbol{\mu}_j \cdot \mathbf{r}) + \boldsymbol{\mu}_j (\boldsymbol{\mu}_i \cdot \mathbf{r})] C(|\mathbf{r}_{ij} + \mathbf{n}|) - (\boldsymbol{\mu}_i \cdot \mathbf{r})(\boldsymbol{\mu}_j \cdot \mathbf{r}) \mathbf{r} D(|\mathbf{r}_{ij} + \mathbf{n}|) \} \\
 & + \frac{2\pi}{V} \sum_{\mathbf{G} \neq 0} \frac{\text{erfc}(G/2\alpha)}{G} (\mathbf{G} \cdot \boldsymbol{\mu}_i^{\parallel}) \mathbf{G} \left[\sin(\mathbf{G} \cdot \mathbf{r}_i) \text{Re} \tilde{N}(\mathbf{G}) - \cos(\mathbf{G} \cdot \mathbf{r}_i) \text{Im} \tilde{N}(\mathbf{G}) \right] \\
 & + \frac{2\pi}{V} \sum_{\mathbf{G} \neq 0} \left[\frac{2\alpha}{\sqrt{\pi}} \exp\left(-\frac{G^2}{4\alpha^2}\right) - \text{Gerfc}\left(\frac{G}{2\alpha}\right) \right] \\
 & \mathbf{G} \left[\sin(\mathbf{G} \cdot \mathbf{r}_i) \text{Re} \tilde{O}(\mathbf{G}) - \cos(\mathbf{G} \cdot \mathbf{r}_i) \text{Im} \tilde{O}(\mathbf{G}) \right], \quad (\text{D.6})
 \end{aligned}$$

where

$$\tilde{N}(\mathbf{G}) = \sum_{j=1}^N (\mathbf{G} \cdot \boldsymbol{\mu}_j^{\parallel}) \exp(i\mathbf{G} \cdot \mathbf{r}_j) \quad (\text{D.7})$$

$$\tilde{O}(\mathbf{G}) = \sum_{j=1}^N \mu_j^z \exp(i\mathbf{G} \cdot \mathbf{r}_j). \quad (\text{D.8})$$

Similarly, we find

$$\begin{aligned}
 \mathbf{T}_i^{2d} = & -\boldsymbol{\mu}_i \times \left[\sum_{j=1}^N \sum_{\mathbf{n}}' (\boldsymbol{\mu}_j B(|\mathbf{r}_{ij} + \mathbf{n}|) + \mathbf{r}(\mathbf{r} \cdot \boldsymbol{\mu}_j) C(|\mathbf{r}_{ij} + \mathbf{n}|)) \right. \\
 & \left. + \frac{2\pi}{A} \sum_{\mathbf{G} \neq 0} \frac{\text{erfc}(G/2\alpha)}{G} \mathbf{G} \left[\sin(\mathbf{G} \cdot \mathbf{r}_i) \text{Re} \tilde{N}(\mathbf{G}) - \cos(\mathbf{G} \cdot \mathbf{r}_i) \text{Im} \tilde{N}(\mathbf{G}) \right] \right. \\
 & \left. + \frac{2\pi}{A} \sum_{\mathbf{G} \neq 0} \left[\frac{2\alpha}{\sqrt{\pi}} \exp\left(-\frac{G^2}{4\alpha^2}\right) - \text{Gerfc}\left(\frac{G}{2\alpha}\right) \right] \mathbf{e}_z \left[\sin(\mathbf{G} \cdot \mathbf{r}_i) \text{Re} \tilde{O}(\mathbf{G}) - \cos(\mathbf{G} \cdot \mathbf{r}_i) \text{Im} \tilde{O}(\mathbf{G}) \right] \right. \\
 & \left. + \frac{4\sqrt{\pi}\alpha}{A} \mathbf{e}_z M_z \right] \quad (\text{D.9})
 \end{aligned}$$

for the torque.

E. Ewald summation of the diffusion tensor

Hydrodynamic interactions are interactions of long-range and, consequently, cannot simply be truncated in a computer simulation. Notwithstanding the errors that would be introduced by such a procedure, a cutoff would result in the diffusion tensor losing its positive definiteness. As a result no meaningful value of L [cf. Eq. (4.87)] would exist.

In this appendix, we present a method based on an Ewald-like summation technique for the diffusion tensor (up to third order in the density) to enable the evaluation of HIs in computer simulations. See Refs. [172,173] for details on the derivation of the respective expressions.

Consider the following equations of motion for a hydrodynamically interacting system [172, 173]:

$$U_i^\alpha = \frac{1}{3\pi\eta a} \left[F_i^\alpha + M_{ij}^{(2)UF}(\mathbf{r}=0)F_j^\alpha + \sum'_{\mathbf{n}} \sum_{\beta=1}^N (M_{ij}^{(1)UF}(\mathbf{r}_{\alpha\beta} + \mathbf{n})F_j^\beta + M_{ij}^{(1)UL}(\mathbf{r}_{\alpha\beta} + \mathbf{n})L_j^\beta) + \frac{1}{V} \sum_{\mathbf{k}} \sum_{\beta=1}^N (M_{ij}^{(2)UF}(\mathbf{k}) \cos(\mathbf{k} \cdot \mathbf{r}_{\alpha\beta})F_j^\beta + M_{ij}^{(2)UL}(\mathbf{k}) \sin(\mathbf{k} \cdot \mathbf{r}_{\alpha\beta})L_j^\beta) \right] \quad (\text{E.1})$$

and

$$\omega_i^\alpha = \frac{4}{3\pi\eta a^3} \left[\frac{3}{4}L_i^\alpha + M_{il}^{(2)\omega F}(\mathbf{r}=0)L_l^\alpha + \sum'_{\mathbf{n}} \sum_{\beta=1}^N (M_{il}^{(1)\omega F}(\mathbf{r}_{\alpha\beta} + \mathbf{n})F_l^\beta + M_{il}^{(1)\omega L}(\mathbf{r}_{\alpha\beta} + \mathbf{n})L_l^\beta) + \frac{1}{V} \sum_{\mathbf{k}} \sum_{\beta=1}^N (-M_{il}^{(2)\omega F}(\mathbf{k}) \sin(\mathbf{k} \cdot \mathbf{r}_{\alpha\beta})F_l^\beta + M_{il}^{(2)\omega L}(\mathbf{k}) \cos(\mathbf{k} \cdot \mathbf{r}_{\alpha\beta})L_l^\beta) \right] \quad (\text{E.2})$$

Here, U_i^α and ω_i^α are the translational and rotational velocities of particle i and the prime at the summation symbol indicates that the $\beta = \alpha$ summation is omitted for $\mathbf{n} = 0$. Further, the parameter a denotes the diameter of the particles and η the viscosity of the solvent. Details on the derivation of Eqs. (E.1) and (E.2) can be found in Refs. [172,173].

In the following, we present the Ewald expressions for the tensors $M_{ij}^{(1)UF}$, $M_{ij}^{(2)UF}$, $M_{ij}^{(1)UL}$, $M_{ij}^{(2)UL}$, $M_{ij}^{(1)\omega F}$, $M_{ij}^{(2)\omega F}$, $M_{ij}^{(1)\omega L}$, and $M_{ij}^{(2)\omega L}$ up to third order in the inverse density.

First, we show the tensors that relate the forces on the particles to their velocities. The real

space contribution is given by

$$\begin{aligned}
 M_{ij}^{(1)UF}(\mathbf{r}) = & \frac{1}{4r^3} \left[\frac{1}{2} a \left[\left(3 \left(\operatorname{erfc}(r\xi) - \frac{1}{\sqrt{\pi}} (2 \exp(-r^2\xi^2) r\xi (2r^2\xi^2 - 1)) \right) r^2 \right. \right. \right. \\
 & + \left. \left. \left(-\frac{1}{\sqrt{\pi}} (2 \exp(-r^2\xi^2) r\xi (4r^6\xi^6 - 16r^4\xi^4 + 2r^2\xi^2 + 3)) - 3\operatorname{erfc}(r\xi) \right) \frac{1}{2} a^2 \right) e_i e_j \right. \\
 & \left. \left. + \left(3 \left(\frac{1}{\sqrt{\pi}} (2 \exp(-r^2\xi^2) r\xi (2r^2\xi^2 - 3)) + \operatorname{erfc}(r\xi) \right) r^2 \right. \right. \\
 & \left. \left. + \left(\frac{1}{\sqrt{\pi}} (2 \exp(-r^2\xi^2) r\xi (4r^6\xi^6 - 20r^4\xi^4 + 14r^2\xi^2 + 1)) + \operatorname{erfc}(r\xi) \right) \frac{1}{2} a^2 \right) \delta_{ij} \right] \right] \quad (\text{E.3})
 \end{aligned}$$

and

$$M_{ij}^{(2)UF}(\mathbf{r} = 0) = \delta_{ij} \left(\frac{\xi}{3\sqrt{\pi}} a (9 - \frac{5}{2}\xi^2 a^2 - \frac{5}{2}\xi^2 a^2) \right). \quad (\text{E.4})$$

Here, ξ is a parameter that controls how fast the expression (E.3) converges. The Fourier contribution equals

$$M_{ij}^{(2)UF}(\mathbf{k}) = (\delta_{ij} - \hat{k}_i \hat{k}_j) \left(\frac{1}{2} a - \frac{1}{48} a^3 k^2 \right) \left(1 + \frac{k^2}{4\xi^2} + \frac{k^4}{8\xi^4} \right) \frac{6\pi}{k^2} \exp\left(-\frac{k^2}{4\xi^2}\right). \quad (\text{E.5})$$

The expressions relating the velocities and torques with each other are given by

$$\begin{aligned}
 M_{ij}^{(1)UL}(\mathbf{r}) = & \frac{1}{8\sqrt{\pi}r^2} \left\{ \frac{1}{2} \exp(-r^2\xi^2) a \left[r^3 a^2 \xi^5 (2r^4\xi^4 - 15r^2\xi^2 + 21) \right. \right. \\
 & \left. \left. + 3(4r^5\xi^5 + 2r\xi - 12r^3\xi^3 + \exp(r^2\xi^2)\sqrt{\pi}\operatorname{erfc}(r\xi)) \right] (e_l \delta_{ij} - e_k \delta_{il}) \epsilon_{lkj} \right\}, \quad (\text{E.6})
 \end{aligned}$$

$$M_{ij}^{(2)UL}(\mathbf{k}) = i\pi \epsilon_{ikj} \hat{k}_k \left(\frac{3}{2} a - \frac{1}{16} a^3 k^2 \right) \left(\frac{1}{k} + \frac{k}{4\xi^2} + \frac{k^3}{8\xi^4} \right) \exp\left(-\frac{k^2}{4\xi^2}\right), \quad (\text{E.7})$$

and

$$M_{ij}^{(2)UL}(\mathbf{r} = 0) = 0. \quad (\text{E.8})$$

At last, the torques on the particles and the angular velocities are related via

$$\begin{aligned}
 M_{il}^{(2)\omega L}(\mathbf{r}) = & \frac{1}{8\sqrt{\pi}r^3} \left\{ \frac{3}{8} \exp(-r^2\xi^2) a^3 \right. \\
 & \left. [(8r^7\xi^7 - 32r^5\xi^5 + 4r^3\xi^3 + 6r\xi + 3 \exp(r^2\xi^2)\sqrt{\pi}\operatorname{erfc}(r\xi)) e_i e_j \right. \\
 & \left. - (8r^7\xi^7 - 40r^5\xi^5 + 28r^3\xi^3 + 2r\xi + \exp(r^2\xi^2)\sqrt{\pi}\operatorname{erfc}(r\xi)) \right] \right\}, \quad (\text{E.9})
 \end{aligned}$$

$$M_{il}^{(2)\omega L}(\mathbf{k}) = \frac{3}{16} \pi a^3 k (\delta_{il} - \hat{k}_i \hat{k}_l) \left(\frac{1}{k} + \frac{k}{4\xi^2} + \frac{k^3}{8\xi^4} \right) \exp\left(-\frac{k^2}{4\xi^2}\right), \quad (\text{E.10})$$

and

$$M_{il}^{(2)\omega L}(\mathbf{k}) = \frac{5}{8\sqrt{\pi}} a^3 \xi^3 \delta_{il}. \quad (\text{E.11})$$

The relation between the forces and the angular velocities [$M_{ij}^{\omega F}$, cf. Eq. (E.2)] can be obtained by symmetry considerations: Recall that the grand diffusion tensor \mathbf{D} [Eq. (4.68)] is symmetric.

F. Reduced units in the ratchet effect

Here, we show how the reduced units used in Ch. 9 are related to the ones used by Engel et al. [47]. The latter are denoted by a superscript “ \dagger ”. For the reduced temperature we find

$$T^* = \mu_0^* D^\dagger \frac{B^*}{B^\dagger}. \quad (\text{F.1})$$

The frequency is given by

$$\omega \frac{\sigma^2}{D_0^{\text{T}^*}} = \frac{3}{D^\dagger}, \quad (\text{F.2})$$

the time by

$$t \frac{D_0^{\text{T}^*}}{\sigma^2} = \frac{1}{3} D^\dagger t^\dagger, \quad (\text{F.3})$$

and the torque by

$$T_z^* = T_z^\dagger \frac{T^*}{D^\dagger}. \quad (\text{F.4})$$

Using $D^\dagger = 0.2$, $\mu_0^* = 1$ [cf. Eq. (7.2)], and choosing $B^\dagger = B^*$ and $\Delta t^\dagger = 0.0015$, yields $T^* = 0.2$, $\Delta t D_0^{\text{T}^*} / \sigma^2 = 0.0001$, and $\omega \sigma^2 / D_0^{\text{T}^*} = 15$. This implies that $T_z^* = T_z^\dagger$.

G. Abbreviations

Here, we list the abbreviations used in this thesis.

BD	Brownian dynamics
DID	Double induced dipole
DSS	Dipolar soft sphere
DFT	Density functional theory
HD	Hard disc
HI	Hydrodynamic interaction
HS	Hard sphere
FP	Fokker-Planck
LB	Lattice Boltzmann
LD	Langevin dynamics
LJ	Lennard-Jones
MC	Monte Carlo
MD	Molecular dynamics
MPCD	Multi-particle collision dynamics
MSA	Mean spherical approximation
MSD	Mean squared displacement
NS	Navier-Stokes
OZ	Ornstein-Zernike
PY	Percus-Yevick
RPA	Random phase approximation
RR	Rotation-rotation
RT	Rotation-translation
SD	Stokesian dynamics
SS	Soft sphere
SSS	Shifted soft sphere
SW	Soft wall
TR	Translation-rotation
TT	Translation-translation

Bibliography

- [1] R. E. Rosensweig, *Ferrohydrodynamics*. Dover Publications, 1997.
- [2] E. Blums, A. O. Cebers, and M. M. Maiorov, *Magnetic Fluids*. de Gruyter, 1997.
- [3] K. Murata, K. Mitsuoka, T. Hirai, T. Walz, P. Agre, J. B. Heymann, A. Engel, and Y. Fujiyoshi, "Structural determinants of water permeation through aquaporin-1," *Nature*, vol. 407, p. 599, 2002.
- [4] B. Berkovski and V. Bashtovoy, *Magnetic fluids and applications handbook*. Begel House Inc., 1996.
- [5] S. Odenbach, "Ferrofluids - magnetically controlled suspensions," *Colloids Surf. A*, vol. 217, p. 171, 2003.
- [6] A. S. Lübbe, C. Alexiou, and C. Bergemann, "Clinical Applications of Magnetic Drug Targeting," *J. Surgical Research*, vol. 95, p. 200, 2000.
- [7] N. A. Brusentsov, L. V. Nikitin, T. N. Brusentsova, A. A. Kuznetsov, F. S. Bayburt-skiy, L. I. Shumakov, and N. Y. Jurchenko, "Magnetic fluid hyperthermia of the mouse experimental tumor," *J. Magn. Magn. Mater.*, vol. 252, p. 378, 2002.
- [8] Q. A. Pankhurst, J. Connolly, S. K. Jones, and J. Dobson, "Applications of magnetic nanoparticles in biomedicine," *J. Phys. D: Appl. Phys.*, vol. 36, p. R167, 2003.
- [9] J. Dzubiella, G. P. Hoffmann, and H. Löwen, "Lane formation in colloidal mixtures driven by an external field," *Phys. Rev. E*, vol. 65, p. 021402, 2002.
- [10] H. Löwen, "Particle-resolved instabilities in colloidal dispersions," *Soft Matter*, vol. 6, p. 3133, 2010.
- [11] K. Kang, M. P. Lettinga, Z. Dogic, and J. K. G. Dhont, "Vorticity banding in rodlike virus suspensions," *Phys. Rev. E*, vol. 74, p. 026307, 2006.
- [12] U. Ognysta, A. Nych, V. Nazarenkom, M. Škarabot, and I. Mušević, "Design of 2D Binary Colloidal Crystals in a Nematic Liquid Crystal," *Langmuir*, vol. 25, p. 12092, 2009.
- [13] P. G. de Gennes and P. A. Pincus, "Pair correlations in a ferromagnetic colloid," *Phys. Kondens. Materie*, vol. 11, p. 189, 1970.
- [14] R. W. Chantrell, A. Bradbury, J. Popplewell, and S. W. Charles, "Agglomerate formation in a magnetic fluid," *J. Appl. Phys.*, vol. 53, p. 2742, 1982.
- [15] K. Butter, P. H. H. Bomans, P. M. Frederik, J. Vroege, and A. P. Philipse, "Direct observation of dipolar chains in iron ferrofluids by cryogenic electron microscopy," *Nature Mater.*, vol. 2, p. 88, 2003.

-
- [16] M. Klokkenburg, B. H. Erné, A. Wiedenmann, A. V. Petukhov, and A. P. Philipse, “Dipolar structures in magnetite ferrofluids studied with small-angle neutron scattering with and without applied magnetic field,” *Phys. Rev. E*, vol. 75, p. 051408, 2007.
- [17] M. Bonini, E. Fratini, and P. Baglioni, “SAXS study of chain-like structures formed by magnetic nanoparticles,” *Mater. Sci. Eng., C*, vol. 27, p. 1377, 2006.
- [18] S. A. Safran, “Magnetic strings and networks,” *Nature Mater.*, vol. 2, p. 72, 2003.
- [19] N. Casic, S. Schreiber, P. Tierno, W. Zimmermann, and T. M. Fischer, “Friction-controlled bending solitons as folding pathway toward colloidal clusters,” *Europhys. Lett.*, vol. 90, p. 58001, 2010.
- [20] J. Jordanovic, S. Jäger, and S. H. L. Klapp, “Crossover from normal to anomalous diffusion in systems of field-aligned dipolar particles,” *Phys. Rev. Lett.*, vol. 106, no. 3, p. 038301, 2011.
- [21] J. E. Martin, E. Venturini, J. Odinek, and R. A. Anderson, “Anisotropic magnetism in field-structured composites,” *Phys. Rev. E*, vol. 61, p. 2818, 2000.
- [22] M. E. Leunissen, H. R. Vutukuri, and A. v. Blaaderen, “Directing Colloidal Self-Assembly with Biaxial Electric Fields,” *Adv. Mater.*, vol. 21, p. 3116, 2009.
- [23] J. F. Douglas, “Membrane magic,” *Nature*, vol. 463, p. 302, 2010.
- [24] J. E. Martin, E. Venturini, G. Gulley, and J. Williamson, “Using triaxial magnetic fields to create high susceptibility particle composites,” *Phys. Rev. E*, vol. 68, p. 021508, 2004.
- [25] J. E. Martin, R. A. Anderson, and J. Williamson, “Generating strange magnetic and dielectric interactions: Classical molecules and particle foams,” *J. Chem. Phys.*, vol. 118, p. 1557, 2003.
- [26] N. Ostermann, I. Poberaj, J. Dobnikar, D. Frenkel, P. Ziherl, and D. Babić, “Field-Induced Self-Assembly of Suspended Colloidal Membranes,” *Phys. Rev. Lett.*, vol. 103, p. 228301, 2009.
- [27] A. Weddemann, F. Wittbracht, B. Eickenberg, and A. Hütten, “Magnetic Field Induced Assembly of Highly Ordered Two-Dimensional Particle Arrays,” *Langmuir*, vol. 26, p. 19225, 2010.
- [28] P. Ilg, “Importance of depletion interactions for structure and dynamics of ferrofluids,” *Eur. Phys. J. E*, vol. 26, p. 169, 2008.
- [29] S. Gangwal, A. Pawar, I. Kretzschmar, and O. D. Velev, “Programmed assembly of metalodielectric patchy particles in external AC electric fields,” *Soft Matter*, vol. 6, p. 1413, 2010.
- [30] J. Philip, P. D. Shima, and B. Raj, “Enhancement of thermal conductivity in magnetite based nanofluid due to chainlike structures,” *Appl. Phys. Lett.*, vol. 91, p. 203108, 2007.
- [31] K. Butter, P. H. H. Bomans, P. M. Frederik, G. J. Vroege, and A. P. Philipse, “Direct observation of dipolar chains in iron ferrofluids by cryogenic electron microscopy,” *Nature Mater.*, vol. 2, p. 88, 2003.

- [32] J. E. Martin, R. A. Anderson, and C. P. Tigges, "Simulation of the athermal coarsening of composites structured by a uniaxial field," *J. Chem. Phys.*, vol. 108, p. 3765, 1998.
- [33] J. E. Martin, R. A. Anderson, and C. P. Tigges, "Thermal coarsening of uniaxial and biaxial field-structured composites," *J. Chem. Phys.*, vol. 110, p. 4854, 1999.
- [34] U. Dassanayake, S. Fraden, and A. van Blaaderen, "Structure of electrorheological fluids," *J. Chem. Phys.*, vol. 112, p. 3851, 2000.
- [35] A.-P. Hynninen and M. Dijkstra, "Phase Diagram of Dipolar Hard and Soft Spheres: Manipulation of Colloidal Crystal Structures by an External Field," *Phys. Rev. Lett.*, vol. 94, p. 138303, 2005.
- [36] J. E. Martin, R. A. Anderson, and C. P. Tigges, "Simulation of the athermal coarsening of composites structured by a biaxial field," *J. Chem. Phys.*, vol. 108, p. 7887, 1998.
- [37] V. V. Murashov and G. N. Patey, "Structure formation in dipolar fluids driven by rotating fields," *J. Chem. Phys.*, vol. 112, p. 9828, 2000.
- [38] S. Jäger and S. H. L. Klapp, "Pattern formation of dipolar colloids in rotating fields: layering and synchronization," *Soft Matter*, vol. 7, p. 6606, 2011.
- [39] S. Jäger and S. H. L. Klapp, "Non-equilibrium structure of rotationally driven dipoles: the role of the simulation method," *Magnetohydrodynamics*, vol. 47, p. 135, 2011.
- [40] N. Elsner, C. P. Royall, B. Vincent, and D. R. E. Snoswell, "Simple models for two-dimensional tunable colloidal crystals in rotating ac electric fields," *J. Chem. Phys.*, vol. 130, p. 154901, 2009.
- [41] N. Osterman, I. Poberaj, J. Dobnikar, D. Frenkel, P. Ziherl, and D. Babić, "Field-Induced Self-Assembly of Suspended Colloidal Membranes," *Phys. Rev. Lett.*, vol. 103, p. 228301, 2009.
- [42] H. Schmidle, S. Jäger, C. K. Hall, O. D. Velez, and S. H. L. Klapp, "Two-dimensional colloidal networks induced by a uni-axial external field," *Soft Matter*, *submitted*, 2012.
- [43] N. Coq, S. Ngo, O. du Roure, M. Fermigier, and D. Bartolo, "Three-dimensional beating of magnetic microrods," *Phys. Rev. E*, vol. 82, p. 041503, Oct 2010.
- [44] P. Tierno, J. Claret, F. Sagués, and A. Cēbers, "Overdamped dynamics of paramagnetic ellipsoids in a precessing magnetic field," *Phys. Rev. E*, vol. 79, p. 021501, Feb 2009.
- [45] W. A. Shelton, K. D. Bonin, and T. G. Walker, "Nonlinear motion of optically torqued nanorods," *Phys. Rev. E*, vol. 71, p. 036204, 2005.
- [46] A. Engel, H. W. Müller, P. Reimann, and A. Jung, "Ferrofluids as thermal ratchets," *Phys. Rev. Lett.*, vol. 91, p. 060602, 2003.
- [47] A. Engel and P. Reimann, "Thermal ratchet effects in ferrofluids," *Phys. Rev. E*, vol. 70, p. 051107, 2004.
- [48] R. E. Goldstein, M. Polin, and I. Tuval, "Noise and Synchronization in Pairs of Beating Eukaryotic Flagella," *Phys. Rev. Lett.*, vol. 103, p. 168103, 2009.

-
- [49] S. Jäger, H. Stark, and S. H. L. Klapp, “Dynamics of cluster formation in driven dipolar colloids dispersed on a monolayer,” *J. Phys.: Condens. Matter*, submitted, 2012.
- [50] M. Rex and H. Löwen, “Influence of hydrodynamic interactions on lane formation in oppositely charged driven colloids,” *Eur. Phys. J. E*, vol. 26, p. 143, 2008.
- [51] A. Satoh, R. W. Chantrell, G. N. Coverdale, and S. Kamiyama, “Stokesian Dynamics Simulations of Ferromagnetic Colloidal Dispersions in a Simple Shear Flow,” *J. Coll. Int. Sci.*, vol. 203, p. 233, 1998.
- [52] A. Grimm and H. Stark, “Hydrodynamic interactions enhance the performance of Brownian ratchets,” *Soft Matter*, vol. 7, p. 3219, 2011.
- [53] P. Maggaretti, I. Pagonabarraga, and D. Frenkel, “Running faster together: huge speed up of thermal ratchets due to hydrodynamic coupling,” *ArXiv e-prints*, abs/1209.4189, 2012.
- [54] J. Kotar, M. Leoni, B. Bassetti, M. C. Lagomarsino, and P. Cicuta, “Hydrodynamic synchronization of colloidal oscillators,” *PNAS*, vol. 107, p. 7669, 2010.
- [55] J. A. Barker and R. O. Watts, “Monte carlo studies of the dielectric properties of water-like models,” *Mol. Phys.*, vol. 26, p. 789, 1973.
- [56] D. J. Adams and E. M. Adams, “Static dielectric properties of the stockmayer fluid from computer simulation,” *Mol. Phys.*, vol. 42, p. 907, 1981.
- [57] K. E. Schmidt and A. L. Michael, “Implementing the fast multipole method in three dimensions,” *J. Stat. Phys.*, vol. 63, p. 1223, 1991.
- [58] M. P. Allen and D. J. Tildesley, *Computer Simulations of Liquids*. Oxford University Press, 1986.
- [59] G. Ganzenmüller and P. J. Camp, “Applications of Wang-Landau sampling to determine phase equilibria in complex fluids,” *J. Chem. Phys.*, vol. 107, p. 237801, 2011.
- [60] J.-M. Caillol, “Search of the gas-liquid transition of dipolar hard spheres,” *J. Chem. Phys.*, vol. 98, p. 9835, 1993.
- [61] G. Ganzenmüller, G. N. Patey, and P. C. Campa, “Vapour-liquid phase transition of dipolar particles,” *Mol. Phys.*, vol. 107, p. 403, 2009.
- [62] L. Rovigatti, J. Russo, and F. Sciortino, “No Evidence of Gas-Liquid Coexistence in Dipolar Hard Spheres,” *Phys. Rev. Lett.*, vol. 107, p. 237801, 2011.
- [63] A. M. Puertas, M. Fuchs, and M. E. Cates, “Simulation study of nonergodicity transitions: Gelation in colloidal systems with short-range attractions,” *Phys. Rev. E*, vol. 67, p. 031406, 2003.
- [64] G. Mériguet, M. Jardat, and P. Turq, “Brownian dynamics investigation of magnetization and birefringence relaxations in ferrofluids,” *J. Chem. Phys.*, vol. 123, p. 144915, 2005.
- [65] Y. Tang, “Role of the Barker-Henderson diameter in thermodynamics,” *J. Chem. Phys.*, vol. 116, p. 6694, 2002.

- [66] S. Grandner and S. H. L. Klapp, "Freezing of charged colloids in slit pores," *J. Chem. Phys.*, vol. 129, p. 244703, 2008.
- [67] S. Grandner, *Structure formation of charged colloidal particles in confined geometry*. PhD thesis, Technische Universität Berlin, 2012.
- [68] S. H. Klapp and M. Schoen, *Reviews in Computational Chemistry*, vol. 24. Wiley, 2007.
- [69] R. G. Larson, *The Structure and Rheology of Complex Fluids*. Oxford University Press, 1999.
- [70] M. J. Stevens and G. S. Grest, "Phase coexistence of a stockmayer fluid in an applied field," *Phys. Rev. E*, vol. 51, pp. 5976–5984, 1995.
- [71] M. E. van Leeuwen and B. Smit, "What makes a polar liquid a liquid?," *Phys. Rev. Lett.*, vol. 71, pp. 3991–3994, 1993.
- [72] B. Groh and S. Dietrich, "Ferroelectric phase in stockmayer fluids," *Phys. Rev. E*, vol. 50, pp. 3814–3833, 1994.
- [73] M. J. Stevens and G. S. Grest, "Structure of soft-sphere dipolar fluids," *Phys. Rev. E*, vol. 51, p. 5962, 1995.
- [74] D. Fincham, N. Quirke, and D. J. Tildesley, "Computer simulation of molecular liquid mixtures. I. A diatomic Lennard-Jones model mixture for CO₂/C₂H₆," *J. Chem. Phys.*, vol. 84, p. 4535, 1986.
- [75] E. J. Bottani and J. M. D. Tascón, eds., *Adsorption by Carbons*. Elsevier, 2008.
- [76] Z. Wang, C. Holm, and H. W. Müller, "Molecular dynamics study on the equilibrium magnetization properties and structure of ferrofluids," *Phys. Rev. E*, vol. 66, p. 021405, 2002.
- [77] H. B. Callen and T. A. Welton, "Irreversibility and Generalized Noise," *Phys. Rev.*, vol. 83, p. 34, 1951.
- [78] W. F. van Gunsteren, H. J. C. Berendsen, and J. A. C. Rullmann, "Stochastic dynamics for molecules with constraints," *Mol. Phys.*, vol. 44, p. 69, 1981.
- [79] T. Geyer and U. Winter, "An $O(N^2)$ approximation for hydrodynamic interactions in Brownian dynamics simulations," *J. Chem. Phys.*, vol. 130, p. 114905, 2009.
- [80] A. Satoh, "Comparison of Approximations between Additivity of Velocities and Additivity of Forces for Stokesian Dynamics Methods," *J. Coll. Int. Sci.*, vol. 243, p. 342, 2001.
- [81] A. J. C. Ladd, "Hydrodynamic interactions in a suspension of spherical particles," *J. Chem. Phys.*, vol. 88, p. 5051, 1988.
- [82] E. Dickinson, S. A. Allison, and J. A. McCammon, "Brownian Dynamics with Rotation-Translation Coupling," *J. Chem. Soc., Faraday Trans. 2*, vol. 81, p. 591, 1985.
- [83] D. L. Ermak and J. A. McCammon, "Brownian dynamics with hydrodynamic interactions," *J. Chem. Phys.*, vol. 69, p. 1352, 1978.

-
- [84] A. J. Banchio and J. F. Brady, "Accelerated Stokesian dynamics: Brownian motion," *J. Chem. Phys.*, vol. 118, p. 10323, 2003.
- [85] P. E. Kloeden and E. Platen, *Numerical Solution of Stochastic Differential Equations*. Springer, 1999.
- [86] C. W. Gardiner, *Handbook of stochastic methods for physics, chemistry, and the natural sciences*. Springer, 2002.
- [87] A. J. C. Ladd and R. Verberg, "Lattice-Boltzmann Simulations of Particle-Fluid Suspensions," *J. Stat. Phys.*, vol. 104, p. 1191, 2001.
- [88] M. E. Cates, K. Stratford, R. Adhikari, P. Stansell, J.-C. Desplat, I. Pagonabarraga, and A. J. Wagner, "Simulating colloid hydrodynamics with lattice Boltzmann methods," *J. Phys.: Condens. Matter*, vol. 16, p. 3903, 2004.
- [89] G. Gompper, T. Ihle, D. M. Kroll, and W. R. G., "Multi-Particle Collision Dynamics: A Particle-Based Mesoscale Simulation Approach to the Hydrodynamics of Complex Fluids," *Adv. Polym. Sci.*, vol. 221, p. 1, 2009.
- [90] J. F. Brady and G. Bossis, "Stokesian dynamics," *Ann. Rev. Fluid Mech.*, vol. 20, p. 111, 1988.
- [91] J. K. G. Dhont, *An Introduction to Dynamics of Colloids*. Elsevier, 1996.
- [92] L. Durlofsky, J. F. Brady, and G. Bossis, "Dynamic simulation of hydrodynamically interacting particles," *J. Fluid Mech.*, vol. 180, p. 21, 1987.
- [93] P. Mazur and W. van Saarloos, "Many-sphere hydrodynamic interactions and mobilities in a suspension," *Physica*, vol. 115A, p. 21, 1982.
- [94] M. Reichert and H. Stark, "Hydrodynamic coupling of two rotating spheres trapped in harmonic potentials," *Phys. Rev. E*, vol. 69, p. 031407, 2006.
- [95] J. Rotne and S. Prager, "Variational Treatment of Hydrodynamic Interaction in Polymers," *J. Chem. Phys.*, vol. 50, p. 4831, 1969.
- [96] J. M. Deutch and I. Oppenheim, "Molecular Theory of Brownian Motion for Several Particles," *J. Chem. Phys.*, vol. 54, p. 3547, 1971.
- [97] P. G. Wolynes and J. M. Deutch, "Dynamical orientation correlations in solution," *J. Chem. Phys.*, vol. 67, p. 733, 1977.
- [98] A. Iniesta and G. de la Torre, "A second-order algorithm for the simulation of the brownian dynamics of macromolecular models," *J. Chem. Phys.*, vol. 92, p. 2015, 1989.
- [99] W. H. Press, S. A. Teukolsky, W. T. Vetterling, and B. P. Flannery, *Numerical Recipes. The Art of Scientific Computing*. Cambridge University Press, 2007.
- [100] J. Lekner, "Summation of coulomb fields in computer-simulated disordered systems," *Physica A*, vol. 176, p. 485, 1991.
- [101] D. Frenkel and B. Smit, *Understanding Molecular Simulation*. Academic Press, 2001.

- [102] P. P. Ewald, "Die berechnung optischer und elektrostatischer gitterpotentiale," *Ann. Phys.*, vol. 64, p. 253, 1921.
- [103] D. M. Heyes, "Pressure tensor of partial-charge and point-dipole lattices with bulk and surface geometries," *Phys. Rev. B*, vol. 49, p. 755, 1994.
- [104] Z. Wang and C. Holm, "Estimate of the cutoff errors in the Ewald summation for dipolar systems," *J. Chem. Phys.*, vol. 115, p. 6351, 2001.
- [105] D. C. Rapaport, *The Art of Molecular Dynamics Simulation*. Cambridge University Press, 2004.
- [106] M. Abramowitz and I. Stegun, *Handbook of Mathematical Functions*. Dover, 1965.
- [107] G. T. Gao, X. C. Zeng, and W. Wang, "Vapor-liquid coexistence of quasi-two-dimensional Stockmayer fluids," *J. Chem. Phys.*, vol. 106, p. 3311, 1997.
- [108] M. Mazars, "Long ranged interactions in computer simulations and for quasi-2D," *Phys. Rep.*, vol. 500, p. 43, 2011.
- [109] J. J. Weis, "Simulation of quasi-two-dimensional dipolar systems," *J. Phys.: Condens. Matter*, vol. 15, p. 1471, 2003.
- [110] L. Dagum and R. Menon, "Openmp: an industry standard api for shared-memory programming," *IEEE Comput. Sci. Engi.*, vol. 5, p. 46, 1998.
- [111] M. Snir, S. Otto, S. Huss-Ledermann, D. Walker, and J. Dongarra, *MPI - The complete reference*. MIT Press, 1998.
- [112] J. Nickolls, I. Buck, M. Garland, and K. Skadron, "Scalable parallel programming with cuda," *Queue*, vol. 6, p. 40, 2008.
- [113] S. W. Koch, R. C. Desai, and F. F. Abraham, "Dynamics of phase separation in two-dimensional fluids: Spinodal decomposition," *Phys. Rev. A*, vol. 27, p. 2152, 1983.
- [114] H. Kabrede and R. Hentschke, "Spinodal decomposition in a 3D Lennard-Jones system," *Physica A*, vol. 361, p. 485, 2006.
- [115] S. Majumder and S. K. Das, "Universality in fluid domain coarsening: The case of vapor-liquid transition," *Europhys. Lett.*, vol. 95, p. 46002, 2011.
- [116] R. C. Desai and R. Kapral, *Dynamics of Self-Organized and Self-Assembled Structures*. Cambridge University Press, 2009.
- [117] K. Lichtner, A. J. Archer, and S. H. L. Klapp, "Phase separation dynamics in a two-dimensional magnetic mixture," *J. Chem. Phys.*, vol. 136, p. 024502, 2012.
- [118] J.-P. Hansen and J. R. McDonald, *Theory of simple Liquids*. Academic Press, 2006.
- [119] J. A. White, A. Gonzalez, F. L. Román, and S. Velasco, "Density-Functional Theory of Inhomogeneous Fluids in the Canonical Ensemble," *Phys. Rev. Lett.*, vol. 84, p. 1220, 2000.

-
- [120] F. Schwabl, *Statistische Mechanik*. Springer, 2006.
- [121] T. V. Ramakrishnan and M. Yussouf, “First-principles order-parameter theory of freezing,” *Phys. Rev. B*, vol. 19, p. 2775, 1979.
- [122] A. D. J. Haymet and D. W. Oxtoby, “A molecular theory for the solid-liquid interface,” *J. Chem. Phys.*, vol. 74, p. 2559, 1981.
- [123] C. G. Gray and K. E. Gubbins, *Theory of Molecular Fluids Fundamentals*. Oxford University Press, 1984.
- [124] M. S. Wertheim, “Exact Solution of the Percus-Yevick Integral Equation for Hard Spheres,” *Phys. Rev. Lett.*, vol. 10, p. 321, 1963.
- [125] M. Baus and J. L. Colot, “Thermodynamics and structure of a fluid of hard rods, disks, spheres, or hyperspheres from rescaled virial expansions,” *Phys. Rev. A*, vol. 36, p. 3912, 1987.
- [126] M. S. Ripoll and C. F. Tejero, “Approximate analytical expression for the direct correlation function of hard discs within the percus-yevick equation,” *Mol. Phys.*, vol. 85, p. 423, 1995.
- [127] X. Guo and U. Riebel, “Theoretical direct correlation function for two-dimensional fluids of monodisperse hard spheres,” *J. Chem. Phys.*, vol. 125, p. 144504, 2006.
- [128] T. C. Halsey, R. A. Anderson, and J. E. Martin, “The rotary electrorheological effect,” *Int. J. Mod. Phys. B*, vol. 10, p. 3019, 1996.
- [129] A. Härtel, R. Blaak, and H. Löwen, “Towing, breathing, splitting, and overtaking in driven colloidal liquid crystals,” *Phys. Rev. E*, vol. 81, p. 051703, 2010.
- [130] J. J. Weis and D. Levesque, “Chain formation in low density dipolar hard spheres: A monte carlo study,” *Phys. Rev. Lett.*, vol. 71, p. 2729, 1993.
- [131] J. Delhommelle, J. Petracic, and D. J. Evans, “Non-newtonian behavior in simple fluids,” *J. Chem. Phys.*, vol. 120, p. 6117, 2004.
- [132] S. H. Strogatz, *Nonlinear Dynamics and Chaos*. Westview Press, 2000.
- [133] M. Argentina, P. Coulet, and L. Mahadevan, “Colliding Waves in a Model Excitable Medium: Preservation, Annihilation, and Bifurcation,” *Phys. Rev. Lett.*, vol. 79, p. 2803, 1997.
- [134] D. Wei, G. N. Patey, and A. Perera, “Orientational order in simple dipolar fluids: Density-functional theory and absolute-stability conditions,” *Phys. Rev. E*, vol. 47, p. 506, 1993.
- [135] F. Smalenburg and M. Dijkstra, “Phase diagram of colloidal spheres in a biaxial electric or magnetic field,” *J. Chem. Phys.*, vol. 132, p. 204508, 2010.
- [136] G. P. Morris and C. P. Dettmann, “Thermostats: Analysis and application,” *Chaos*, vol. 8, p. 321, 1998.
- [137] Y.-K. Tao, W. K. den Otter, and W. J. Briels, “Kayaking and wagging of liquid crystals under shear: Comparing director and mesogen motions,” *Europhys. Lett.*, vol. 86, no. 5, p. 56005, 2009.

- [138] F. Wittbracht, B. Eickenberg, A. Weddemann, and A. Hütten, “Rotating magnetic field assisted formation of highly ordered two-dimensional magnetic bead arrays,” in *ICQNM 2011, The Fifth International Conference on Quantum, Nano and Micro Technologies*, p. 99, 2012.
- [139] P. Tierno, R. Muruganathan, and T. M. Fischer, “Viscoelasticity of Dynamically Self-Assembled Paramagnetic Colloidal Clusters,” *Phys. Rev. Lett.*, vol. 98, p. 028301, 2007.
- [140] D. R. E. Snoswell, C. L. Bower, P. Ivanov, M. J. Cryan, J. G. Rarity, and B. Vincent, “Dynamic control of lattice spacing within colloidal crystals,” *New Journal of Physics*, vol. 8, no. 11, p. 267, 2006.
- [141] S. Jäger, H. Schmidle, and S. H. L. Klapp, “Non-equilibrium condensation and coarsening of field-driven dipolar colloids,” *Phys. Rev. E*, vol. 86, p. 011402, 2012.
- [142] F. Wang and D. P. Landau, “Efficient, multiple-range random walk algorithm to calculate the density of states,” *Phys. Rev. Lett.*, vol. 86, pp. 2050–2053, Mar 2001.
- [143] H. Schmidle and S. H. L. Klapp, “Phase transitions of two-dimensional dipolar fluids in external fields,” *J. Chem. Phys.*, vol. 134, no. 11, p. 114903, 2011.
- [144] P. D. Duncan and P. J. Camp, “Structure and dynamics in a monolayer of dipolar spheres,” *J. Chem. Phys.*, vol. 121, p. 11322, 2004.
- [145] J. F. M. Lodge and D. M. Heyes, “Brownian dynamics simulations of Lennard-Jones gas/liquid phase separation and its relevance to gel formation,” *J. Chem. Soc., Faraday Trans.*, vol. 93, p. 437, 1997.
- [146] J. A. Barker, D. Henderson, and F. F. Abraham, “Phase diagram of the two-dimensional lennard-jones system; evidence for first-order transitions,” *Physica A*, vol. 106, no. 1-2, pp. 226–238, 1981.
- [147] F. F. Abraham, S. W. Koch, and R. C. Desai, “Computer-Simulation Dynamics of an Unstable Two-Dimensional Fluid: Time-Dependent Morphology and Scaling,” *Phys. Rev. Lett.*, vol. 49, p. 923, 1982.
- [148] E. Velasco and S. Toxvaerd, “Computer Simulation of Phase Separation in a Two-Dimensional Binary Fluid Mixture,” *Phys. Rev. Lett.*, vol. 71, p. 388, 1993.
- [149] H. Stark, *private communication*.
- [150] I. O. Götze and G. Gompper, “Dynamic self-assembly and directed flow of rotating colloids in microchannels,” *Phys. Rev. E*, vol. 84, p. 031404, 2011.
- [151] R. Yamamoto, K. Kim, Y. Nakayama, K. Miyazaki, and D. R. Reichmann, “On the Role of Hydrodynamic Interactions in colloidal Gelation,” *J. Phys. Soc. Jpn.*, vol. 77, p. 084804, 2008.
- [152] M. Reichert and H. Stark, “Synchronization of rotating helices by hydrodynamic interactions,” *Eur. Phys. J. E*, vol. 17, p. 493, 2005.
- [153] J. Russo, J. M. Tavares, P. I. C. Teixeira, M. M. Telo da Gama, and F. Sciortino, “Reentrant phase diagram of network fluids,” *Phys. Rev. Lett.*, vol. 106, p. 085703, Feb 2011.

-
- [154] J. Tailleur and M. E. Cates, “Statistical mechanics of interacting run-and-tumble bacteria,” *Phys. Rev. Lett.*, vol. 100, p. 218103, May 2008.
- [155] F. Ginelli, F. Peruani, M. Bär, and H. Chaté, “Large-scale collective properties of self-propelled rods,” *Phys. Rev. Lett.*, vol. 104, p. 184502, May 2010.
- [156] P. Hänggi and F. Marchesoni, “Artificial Brownian Motors: Controlling transport on the nanoscale,” *Rev. Mod. Phys.*, vol. 81, p. 387, 2009.
- [157] P. Reimann, “Brownian motors: noisy transport far from equilibrium,” *Phys. Rep.*, vol. 361, p. 57, 2002.
- [158] R. D. Astumian and P. Hänggi, “Brownian motors,” *Phys. Today*, vol. 55, p. 33, 2002.
- [159] M. O. Magnasco, “Forced thermal ratchets,” *Phys. Rev. Lett.*, vol. 71, p. 1477, 1993.
- [160] F. Jülicher, A. Ajdari, and J. Prost, “Modeling molecular motors,” *Rev. Mod. Phys.*, vol. 69, p. 1269, 1997.
- [161] J. Rousselet, L. Salome, A. Ajdari, and J. Prost, “Directional motion of brownian particles induced by a periodic asymmetric potential,” *Nature*, vol. 370, p. 446, 1994.
- [162] H. Linke, T. E. Humphrey, A. Löfgren, A. O. Sushkov, R. Newbury, R. P. Taylor, and P. Omling, “Experimental tunneling ratchets,” *Science*, vol. 286, p. 2314, 1999.
- [163] V. Becker and A. Engel, “Role of interactions in ferrofluid thermal ratchets,” *Phys. Rev. E*, vol. 75, p. 031118, 2007.
- [164] T. John and R. Stannarius, “Experimental investigation of a brownian ratchet effect in ferrofluids,” *Phys. Rev. E*, vol. 80, p. 050104(R), 2009.
- [165] S. Jäger and S. H. L. Klapp, “Rotational ratchets with dipolar interactions,” *Phys. Rev. E*, vol. 86, p. 061402, 2012.
- [166] A. Pototsky, A. J. Archer, S. E. Savel’ev, U. Thiele, and F. Marchesoni, “Ratcheting of driven attracting colloidal particles: Temporal density oscillations and current multiplicity,” *Phys. Rev. E*, vol. 83, p. 061401, 2011.
- [167] P. Reimann, R. Kawai, C. Van den Broeck, and P. Hänggi, “Coupled brownian motors: Anomalous hysteresis and zero-bias negative conductance,” *Europhys. Lett.*, vol. 45, p. 545, 1999.
- [168] A. O. Ivanov and O. B. Kuznetsova, “Magnetic properties of dense ferrofluids: An influence of interparticle correlations,” *Phys. Rev. E*, vol. 64, p. 041405, 2001.
- [169] S. H. L. Klapp and M. Schoen, “Spontaneous orientational order in confined dipolar fluid films,” *J. Chem. Phys.*, vol. 117, p. 8050, 2002.
- [170] M. A. Miller, R. Blaak, C. N. Lumb, and J.-P. Hansen, “Dynamical arrest in low density dipolar colloidal gels,” *J. Chem. Phys.*, vol. 130, p. 114507, 2009.
- [171] P. Ilg and E. Del Gado, “Non-linear response of dipolar colloidal gels to external fields,” *Soft Matter*, vol. 7, p. 163, 2011.

- [172] C. W. J. Beenakker, “Ewald sum of the Rotne-Prager tensor,” *J. Chem. Phys.*, vol. 85, p. 1591, 1986.
- [173] K. R. Hase and R. L. Powell, “Calculation of the Ewald summed far-field mobility functions for arbitrarily sized spherical particles in Stokes flow,” *Phys. Fluids*, vol. 13, p. 32, 2001.